ANALYSIS OF OFF-AXIS, LOW-VELOCITY ZONES ON THE FLANKS OF THE ENDEAVOUR SEGMENT OF THE JUAN DE FUCA RIDGE

by

ANNE ELIZABETH WELLS

A THESIS

Presented to the Department of Geological Sciences
and the Graduate School of the University of Oregon
in partial fulfillment of the requirements
for the degree of
Master of Science

March 2012

THESIS APPROVAL PAGE

Student: Anne Elizabeth Wells

Title: Analysis of Off-axis, Low-velocity Zones on the Flanks of the Endeavour Segment of the Juan de Fuca Ridge

This thesis has been accepted and approved in partial fulfillment of the requirements for the Master of Science degree in the Department of Geological Sciences by:

Emilie Hooft	Chairperson
Douglas Toomey	Member
William Wilcock	Member
Eugene Humphreys	Member

and

Kimberly Andrews Espy	Vice President for Research & Innovation/Dean of the Graduate School

Original approval signatures are on file with the University of Oregon Graduate School.

Degree awarded March 2012

THESIS ABSTRACT

Anne Elizabeth Wells

Master of Science

Department of Geological Sciences

March 2012

Title: Analysis of Off-axis, Low-velocity Zones on the Flanks of the Endeavour Segment of the Juan de Fuca Ridge

Seismic data from the intermediate-spreading Endeavour segment of the Juan de Fuca Ridge reveal several crustal-level, low-velocity, high-attenuation regions on the eastern and western ridge flanks 7 to 16 km from the neovolcanic zone. I examine *Pg* amplitude anomalies for a wide variety of source-receiver azimuths in the Endeavour active source seismic tomography data. I use finite difference waveform forward modeling to estimate the dimensions, depth, and seismic properties of the best-observed inferred anomalous regions. The attenuating regions extend 10-15 km beneath axis-parallel bathymetric highs and from 2 to 4 km below the seafloor. The velocity reduction is small (~8%) and the attenuation large ($Q_P \approx$ 8-40) suggesting the presence of partial melt. I infer that melt focusing toward the neovolcanic zone is incomplete and that tectonic interactions with the Heckle seamount chain and/or the large segment-bounding overlapping spreading centers may promote off-axis melt delivery at the Endeavour segment.

CURRICULUM VITAE

NAME OF AUTHOR: Anne Elizabeth Wells

GRADUATE AND UNDERGRADUATE SCHOOLS ATTENDED:

University of Oregon, Eugene, OR

University of Tennessee, Knoxville, TN

University of Malta, Msida, Malta

DEGREES AWARDED:

Master of Science, Geological Sciences, 2012, University of Oregon

Bachelor of Science, Chemical Engineering, 2007, University of Tennessee

AREAS OF SPECIAL INTEREST:

Marine Geophysics
The crustal structure of mid-ocean spreading centers.
Seismology
The application of seismic methods to constrain variations in crustal structure.

PROFESSIONAL EXPERIENCE:

Graduate Teaching Fellow University of Oregon, Eugene, OR, 2009 - 2011

Subsurface Engineer, ExxonMobil, Houston, TX, 2007 – 2009

Chemical Engineer Intern, Honeywell, Hopewell, VA, 2004 – 2005

ACKNOWLEDGMENTS

I wish to express my infinite appreciation of Professor Emilie Hooft for all of her guidance, support, and patience during the completion of this project. She gave me a great opportunity to learn and participate in exciting research. I would like to thank Douglas Toomey and William Wilcock for all of their help, guidance, and extremely time saving computer codes. I would like to thank Gene Humphreys, Ray Weldon, and Marli Miller for their advice and guidance. I would like to thank Robert Weekly, Troy Durant, Matt Beachly, Dax Soule, Amberlee Darold, Ashley Streig, and Kohtaro Araragi for their help completing my research. I would also like to thank the crews of the R/V Marcus G. Langseth, Scripps, and WHOI, and many thanks to the National Science Foundation for funding the Endeavour Seismic Tomography Study, grant OCE-0454747.

I offer my greatest measure of gratitude to my family and friends. Their blessings make anything possible.

I dedicate this manuscript to my family,

who have supported and loved me always.

TABLE OF CONTENTS

Chapter Page

LIST OF FIGURES

Figure Page

Figure Page

LIST OF TABLES

Table Page

CHAPTER I

INTRODUCTION

Oceanic crust forms primarily within a 1–2 km wide neovolcanic zone at mid-ocean ridges of all spreading rates (Macdonald, 1984); however, there is an increasing recognition that crustal structure is modified by off-axis volcanism. Our knowledge of off-axis volcanism has been limited in the past due to the scale of geophysical surveys and their focus on the ridge axis. Only through more recent, larger geophysical surveys have off-axis areas been investigated. The identification of off-axis, crustal-level melt sills and low-velocity bodies at the East Pacific Rise (Durant and Toomey, 2009; Canales et al., 2012) leads to the questions of whether off-axis volcanism is a common occurrence at mid-ocean ridges and what processes contribute to its development. Possible explanations of volcanism outside of the neovolcanic zone could be weak focusing of mantle melt delivery and the result of complex tectonic settings interacting with melt delivery. Answering these questions affects our overall understanding of the creation of oceanic crust.

A recent study identified a crustal-level melt sill and low-velocity, high-attenuation body 20 km away from the rise axis at the East Pacific Rise, between the Siqueiros and Clipperton transforms (Durant and Toomey, 2009). They use seismic data from the UNDERSHOOT experiment (Toomey et al., 2007) to reveal an intrusive complex approximately 2 km beneath the seafloor. The intrusive complex is limited in lateral extent to less than 5 km and contains a narrow melt lens with a wider, low-velocity, high-attenuation crust beneath. They identify the complex by observing *P* waveforms

diffracting around the low-velocity body, abrupt attenuation of energy propagating through the region, and also large amplitude *P*-to-*S* wave conversions that require a solid-liquid interface.

Because of the limited spatial extent of the low-velocity body, it was not detected in delay time tomographic velocity inversions (Canales et al., 2003) due to post-anomaly wavefront healing. That is to say, the resulting small travel time delays for first arrivals (<50 ms) caused difficulty in resolving the anomaly with delay time tomographic methods. Instead, the low-velocity body was discovered by examining waveform data.

Anomalous *P* waveforms were observed in the seismic records for two of the instruments (Durant and Toomey, 2009 – **Figure 1.1 b**). The observed anomalous waveforms are similar to diffracted arrivals predicted from waveform modeling of the axial magma chamber (**Figure 1.2**) (Wilcock et al., 1993). Wilcock et al. (1993) modeled diffractions of a *P* wave turning through the crust as it encountered a low-velocity anomaly whose vertical dimension is less than the seismic wavelength and is also underlain by a broad low-velocity body. This causes energy to propagate above and below the anomalous body. The energy propagating above is shown in **Figure 1.2 a** as *dPa* waves and the energy propagating below is shown as *dPb* waves. As *P* waves encounter the broad low-velocity region, a decrease in wave amplitude also occurs. The diffractions of the *P* waves are seen in a seismic record by a significant drop in wave amplitude, accompanied by a second separate arrival (**Figure 1.2 b**). Durant and Toomey (2009) observe diffractions of *P* waves and also strongly attenuated first-arriving energy (*dPb*) at longer ranges (**Figure 1.1 b**). **Figure 1.1 c** shows a third observation of large amplitude *P*-to-*S* wave conversions in the radial direction.

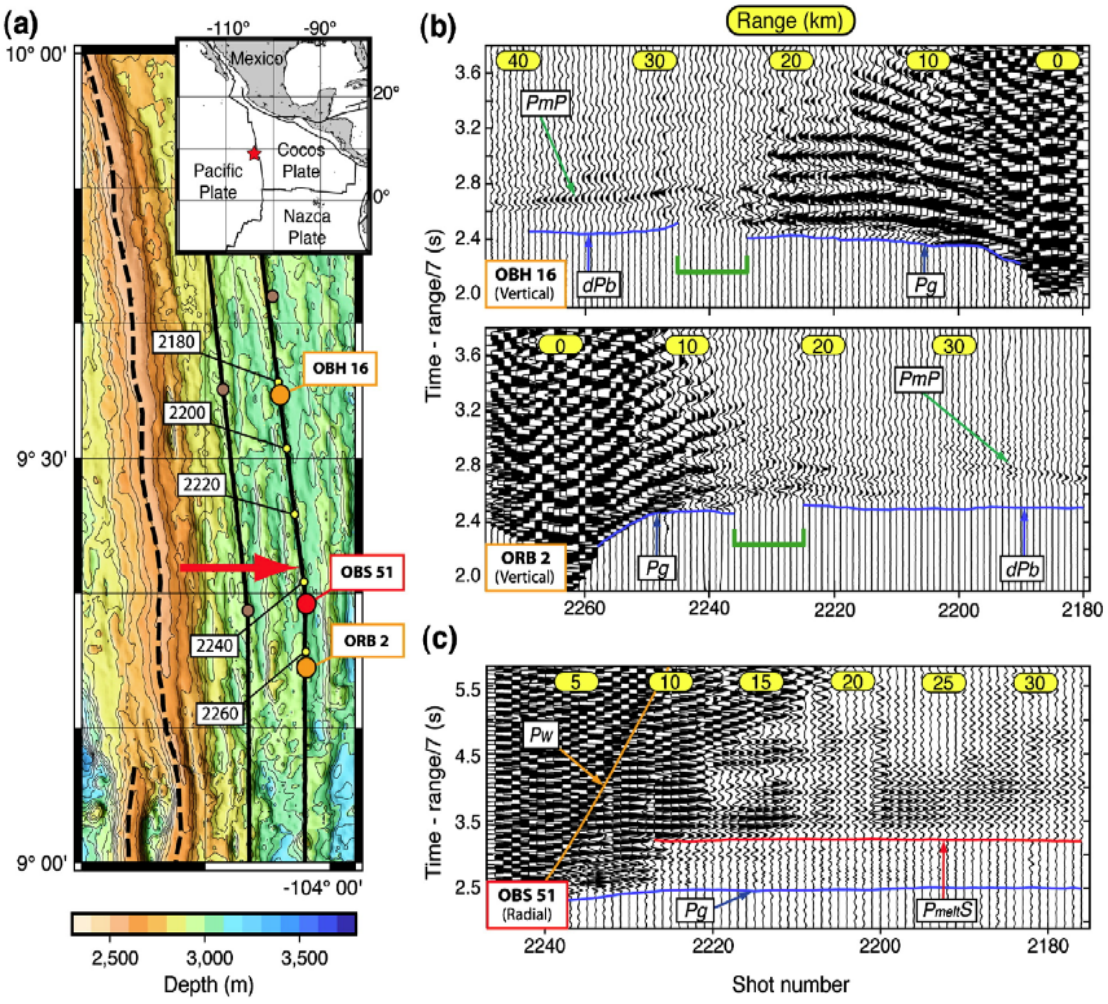

Figure 1.1. Map of the experimental geometry and seismic record sections of the 9°20′N region of the East Pacific Rise taken from Durant and Toomey (2009). (a) Map locations of instruments that recorded the *P* wave diffractions (orange circles) and $P_{melt}S$ arrivals (red circle), shown in record sections (b) and (c), respectively. Small, brown circles represent other instruments in the region. Specific shot locations (yellow circles) for each record section are labeled. The location of the magmatic complex is indicated by the red arrow. (b) Record sections for OBH 16 (top) and ORB 2 (bottom) hydrophones, which show diffracted *P* wave arrivals and a sudden decrease in waveform amplitudes. Record sections are aligned by shot number (bottom axis), ranges are shown in yellow ovals (top axis); amplitudes are fixed scaled. The green bar shows the diffracted *P* wave arrivals. (c) Radial record section for OBS 51, which shows $P_{melt}S$ (red line). *Pg* (blue line) and *Pw* (water wave; orange line) phases are also shown; amplitudes are fixed scaled. Large amplitudes of $P_{melt}S$ arrivals out to ranges of 30 km are shown. All record sections are plotted with a velocity reduction of 7 km/s and are band-pass filtered between 5 and 30 Hz.

There are no bathymetric or morphologic features that would indicate extrusive volcanism above the off-axis magma body at the East Pacific Rise. However, evidence of off-axis magmatic and hydrothermal activity has been found elsewhere. Abnormally young lavas were found at off-axis locations (Zou et al., 2002), and hydrothermal fluids have been imaged at different off-axis locales on the western side of the rise axis (10°20'N, 103°33.2'W and 9°27'N, 104°32.3'W) using seafloor mapping (Haymon et al., 2005).

The East Pacific Rise and Juan de Fuca Ridge are two of the most intensely studied mid-ocean ridges in the world. Multiple studies have focused on mantle melting and crustal formation at both sites. The off-axis volcanism discovered at the East Pacific Rise inspired this study of the Endeavour segment of the Juan de Fuca Ridge. I investigate the presence of off-axis, crustal-level, low-velocity zones on both the eastern and western sides of the Endeavour segment, using data from the multi-scale Endeavour Seismic Tomography Experiment (ETOMO) that took place in September 2009. The ETOMO experiment was performed to constrain the nature of sub-ridge mantle flow and melt transport pattern from the top part of the mantle to the crust beneath the entire Endeavour segment. I examine the travel times and amplitude anomalies of the *Pg* phase (*P* waves that turn within the crust) for a wide variety of source-receiver azimuths and observe significant and localized decreases in the amplitude of *P* waves on the eastern and western flanks of the Endeavour segment, suggesting a loss of energy due to low-velocity, high-attenuation bodies in the mid-crust. Using ray tracing and finite difference modeling, I am able to estimate the dimensions, depths, and physical properties of several of the best-observed anomalous regions.

Figure 1.2 (next page). Finite difference modeling of a magma sill taken from Wilcock et al. (1993). The fully molten magma sill is 200 m thick and 2 km wide with a broad low-velocity region beneath. (a) Finite difference experiment's crustal ray-theoretical paths. Paths show the *P*-diving phase (solid) and diffractions above (*dPa*) (solid line) and below (*dPb*) (dashed) the magma chamber. The *dPa* and *dPb* waves are diffracted around a magma body located 1.6 km beneath the seafloor. (b) Velocity model used for finite difference modeling. *P* wave velocity (*Vp*) is shown as a contour plot. The depths are relative to the sea surface, 2.8 above the seafloor. (c) Pressure record section. A decrease in amplitude can been seen where the *P* waves are diffracted (*dPa* and *dPb*) and also intercept the broad low-velocity region. The range where the *P* waves are first diffracted is ~2 km further in distance from the seismometer than the magma sill. This happens because at closer ranges rays turn at shallower depths; therefore, not intercepting the magma body until further away from the seismometer.

(a)

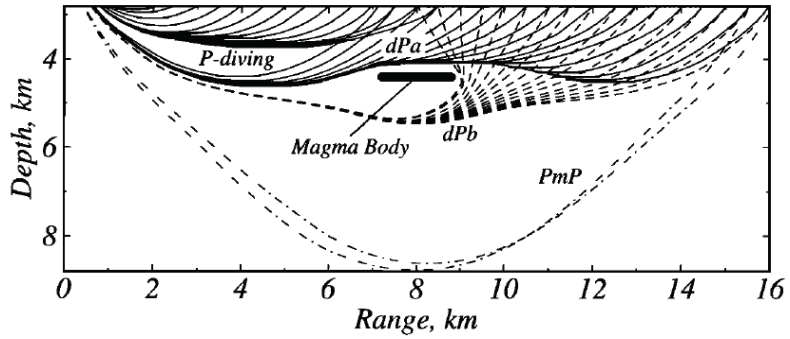
P-diving
dPa
dPb
Magma Body
PmP
Depth, km
Range, km
0
2
4
6
8
10
12
14
16

(b)

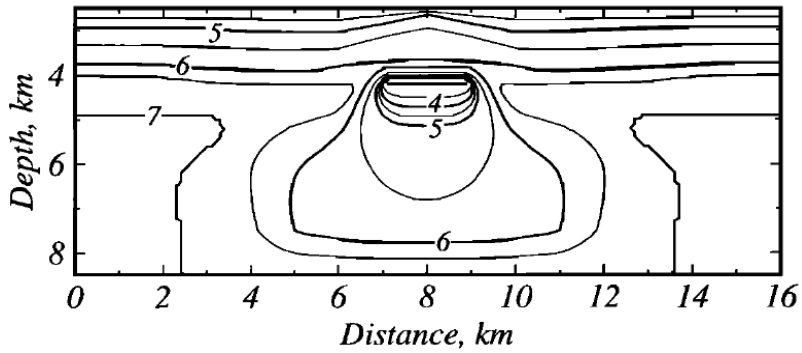
5
6
7
4
5
6
Depth, km
Distance, km
0
2
4
6
8
10
12
14
16

(c)

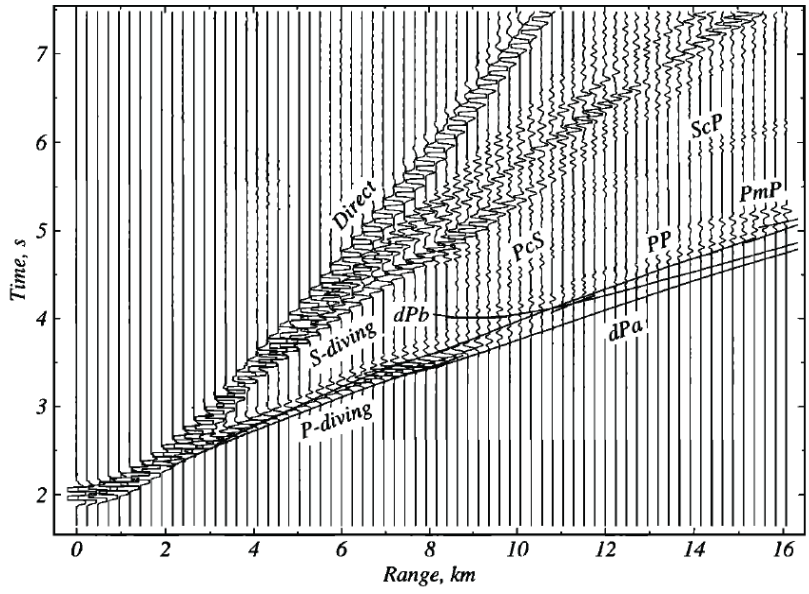
Direct
S-diving
P-diving
dPb
dPa
PcS
PP
ScP
PmP
Time, s
Range, km
2
3
4
5
6
7
0
2
4
6
8
10
12
14
16

CHAPTER II

REGIONAL SETTING AND TECTONIC HISTORY

The Juan de Fuca Ridge is a near constant rate intermediate spreading boundary between the Juan de Fuca Plate and the Pacific plate at latitude 44^0 to 52^0N. In a hot-spot reference frame, the spreading center is moving northwest (110° oblique to the spreading direction) at ~31 mm/yr (Carbotte et al., 2008) with a 30 mm/yr half-spreading rate (Riddihough, 1984). The Juan de Fuca Ridge consists of seven segments and has a transitional morphology characterized by fault-bounded ridges that parallel the spreading center with a history of near ridge and on-axis hot spot volcanism (Carbotte et al., 2008).

The Endeavour segment is ~90 km long and lies between the Cobb and Endeavour OSCs on the northern Juan de Fuca Ridge (**Figure 2.1**). A 1 – 2 km wide, 10 – 100 m deep inner rift is observed, overlaid on larger structures ranging from 5 – 10 km wide, as much as 3,000 m deep median valleys towards the southern end of the segment to 5 km wide, 2,100 deep volcanic ridges around the center of the segment (Karsten et al., 1986). Van Ark et al. (2007) finds a 16 – 24 km long, 0.4 – 1.2 km wide, crustal-level magma body along the ridge axis and Johnson et al. (1983) interprets there to have been recent volcanism at the Endeavour segment from seismic reflection and magnetometer surveys, photographic coverage, and dredging of volcanic rock; however Carbotte et al., (2006) and Nedimovic et al. (2008) interpret the 2 – 3 km wide axial trough to indicate there have been no recent eruptions, and many of Endeavour's characteristics were incorrectly interpreted to indicate there is minimal magma supply (Wilcock and Delaney, 1996).

The Cobb offset, which separates the Endeavour and Northern Symmetric segments, is interpreted to have been propagating north for ~4.5 Ma (Carbotte et al., 2008). At ~0.8 Ma, the Endeavour segment began propagating southward, but within the past 100,000 years, the propagation has reversed (Carbotte et al., 2008). The Endeavour and Northern Symmetric ridge segments overlap for ~30 km and are separated by ~30 km in the overlap region (Shoberg et al., 1991). The Endeavour offset, ~13 km wide, separates the West Valley and Endeavour segments and is interpreted to have formed when the spreading ridge jumped from Middle Valley to West Valley <200,000 yr ago (Karsten et al., 1986). The West Valley segment is inferred to be propagating south cutting into the Endeavour segment (Van Wagoner and Leybour, 1991).

A series of asymmetric, ridge-parallel abyssal hills, which are spaced around 6 km (~200,000 years) apart and are <300 m high (Barclay and Wilcock, 2003), are prominent in the central area of the Endeavour segment, which is interpreted to be on a ~40 km wide plateau (Van Ark et al., 2007). The location of the broad plateau (**Figure 2.2**) on axis aligns with projection of the trend of the Heckle seamount chain and is construed from seismic reflection work to have greater crustal thickness (~0.5-1.0 km) that began forming about 0.7 Ma (Carbotte et al., 2008). The plateau is interpreted to have developed when the northwestward migrating Juan de Fuca Ridge overrode the mantle melt anomaly associated with the Heckle seamount chain. Since the Northern Symmetric has been propagating northward for the past 100,000 years, the magma supply from the presumed Heckle hotspot may be waning at the Endeavour segment if the magma supply controls segmentation (Carbotte et al., 2008).

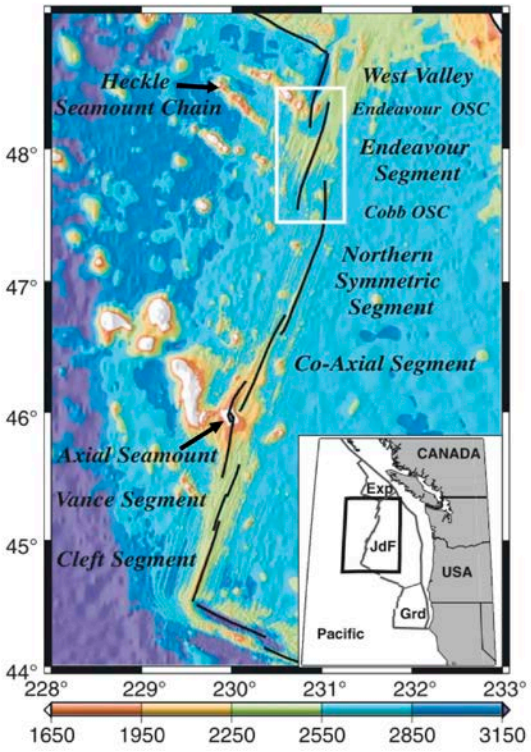

Figure 2.1. Map with locations of Juan de Fuca Ridge segments taken from Van Ark et al. (2007). Each segment is represented by black lines. The Endeavour segment is located within the white box. The broad plateau of interpreted thicker crust is located along the projection of the Heckle seamount chain.

A multichannel reflection study (Van Ark et al., 2007) observes mid-crustal reflectors at depths of ~2.1 – 3.3 km below the seafloor beneath the hydrothermal vent fields at the Endeavour segment, indicating there is a magma body under the rise-axis. The magma body is found to be narrow (0.4 – 1.2 km wide) and segmented into multiple crustal magma lenses; the total extent of the magma body along-axis is 16 – 24 km. The magma chamber is shown to be dipping from ~2.1 km to 2.4 km depth from west to east from cross axis seismic lines, except beneath the southern hydrothermal vent field, Mothra, where the magma chamber dips from 2.5 km to 3.1 km (Van Ark et al., 2007). Data from the reflection survey, EW02-07, has also shown evidence of crustal-level

reflectors off-axis on both the eastern and western sides of the ridge axis (S. M. Carbotte pers. comm.). One of the reflectors on the western side has reversed polarity, indicating the possibility of a crustal-level, pure melt or partially molten magma body.

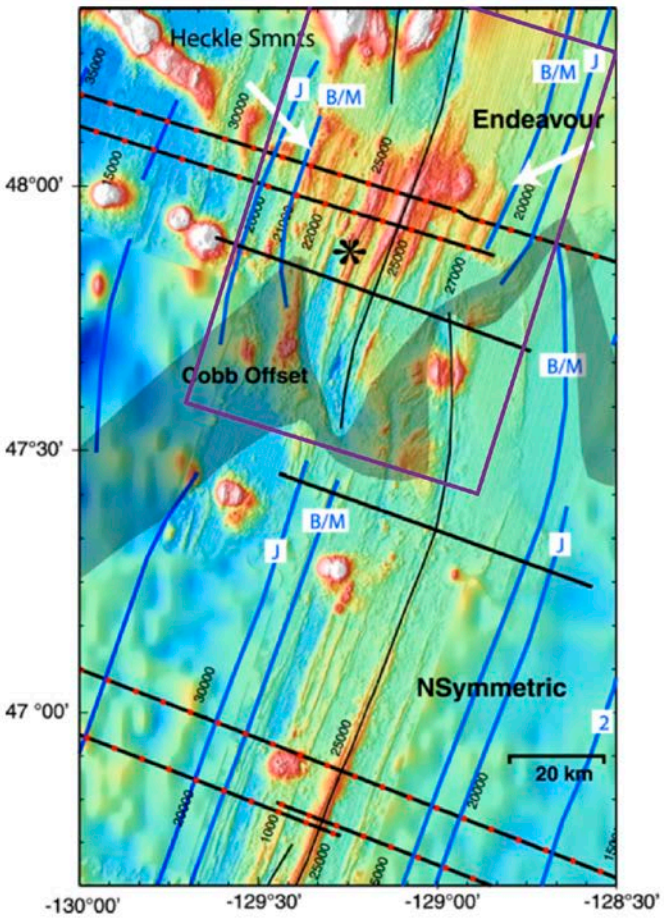

Figure 2.2. Bathymetric map of Endeavour and Northern Symmetric segments taken from Carbotte et al. (2008). The purple box shows the region covered by the ETOMO study. The medium-weight black lines mark the locations of the current ridge axes. The blue lines show the magnetic isochrones (B/M, Brunhes/Matuyama; J, Jaramilo; 2, anomaly 2; and 2a, anomaly 2a). The white arrows show the interpreted boundaries of the ~40 km wide plateau. The black star highlights the prominent west flank hill, which may be where the ridge axis was prior to the small ridge jump to the current location. The gray shading shows the approximate region of disturbed seafloor associated with recent history of dueling propagation between the Northern Symmetric and Endeavour segments. The thick black lines (a, b, c, and d) show the locations multichannel seismic profiles were shot (Carbotte et al., 2008).

Studies have found that lateral differences in the velocity structure for the upper crust at a mid-ocean ridge provide constraints on the volcanic processes that create young crust (Barclay and Wilcock, 2003). At the Endeavour segment, axis-parallel alternating bands of high and low velocity are seen in the shallow crustal velocity structure. An inverse correlation between the velocity variation and bathymetry is seen with the low-velocity bands being associated with the axis-parallel seafloor ridges. These velocity variations have previously been explained by a 100 – 200 m increase in layer 2A thickness beneath split volcanic ridges, implying the processes that create the bathymetric highs result in a thicker extrusive layer (Barclay and Wilcock, 2003). Van Ark et al. (2007) also observed a thicker 2A layer beneath axis-parallel bathymetric highs, which is interpreted to be caused by either intermittent periods of magma supply (Kappel and Ryan, 1986) or dike induced normal faulting (Carbotte et al., 2006). The latter model implies a more steady state magma supply and predicts intermittent topography through the interplay of tectonic extensional stresses and dike-induced stress perturbations (Van Ark et al., 2007).

CHAPTER III

METHODS

Section 3.1. ETOMO Seismic Experiment

Seismic data were collected along the Endeavour segment of the Juan de Fuca Ridge, using an array of 68 four-component ocean bottom seismometers (OBS) at 64 sites and the 6600 in^3 airgun array of the *R/V Marcus G. Langseth*. The 30-day study includes 5,567 near-surface air gun shots within a region extending 90 km along-axis and 50 km across. Shot and OBS locations are shown in **Figure 3.1**. Three nested shooting plans, Undershoot, Crustal Grid, and Inner Crustal Grid, were implemented with shots spaced at 450 m along each shot line. The Undershoot shot lines (outer three lines on the east and west sides of the ridge axis and the outer lines in the far north and south in **Figure 3.1**) are designed to constrain ridge crest segmentation, mantle upwelling and melt transport. The Crustal Grid shot lines compromising nineteen lines oriented parallel to the ridge axis spaced 1 km apart, will constrain the shape, size and distribution of crustal magma bodies fueling the Endeavour hydrothermal system. The Inner Crustal Grid included an additional ten shorter shot lines interspaced with the crustal grid to examine the hydrothermal vent fields and their interaction with the spreading center. Details of the experiment can be found in Toomey et al. (2009).

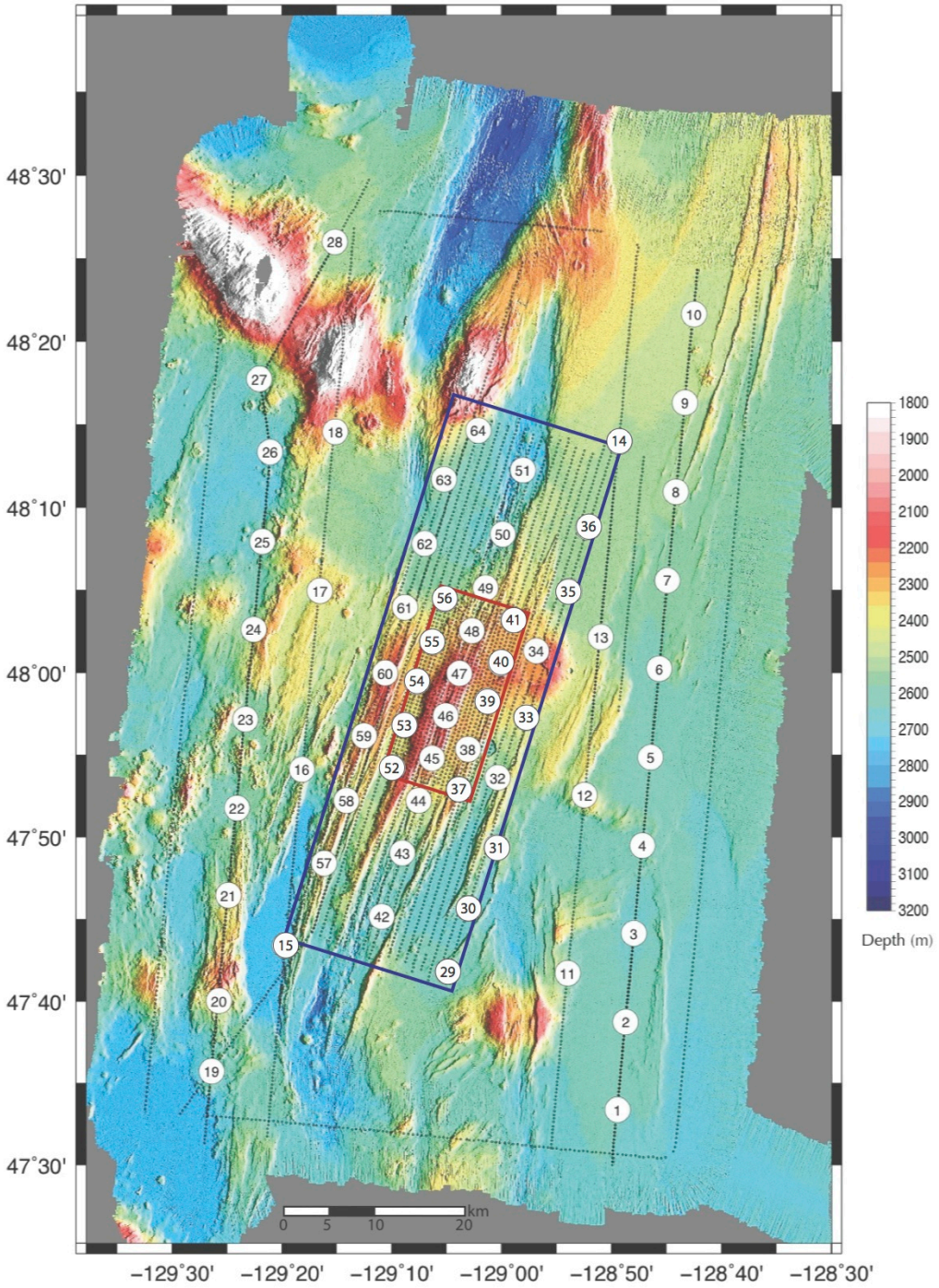

Figure 3.1. Bathymetric map of Endeavour segment from the ETOMO study. ETOMO shot locations are shown by small black circles; OBS locations are shown by the larger white circles with each OBS's number in the middle. The color scale shows the seafloor depth. The three shooting plans are shown. The red box encloses the Inner Crustal Grid, the blue box encloses the Crustal Grid, and outside of the blue box are the Undershoot shot lines.

Section 3.2. Record Section Interpretation

I examine the seismic travel times and amplitude anomalies of the *Pg* phase for a wide variety of source-receiver azimuths on the outer east and west regions of the Endeavour Segment, located more than 7 km from the ridge axis (**Figure 3.1**, OBSs 1-36 and 57-63). I look for regions with disrupted and/or low-amplitude *P* waves that could be due to a high-attenuation, low-velocity body in the mid-crust. The primary step for locating and analyzing the off-axis, low-velocity zones is to compare seismic records for OBSs 1-36 and 57-63, looking for waveform amplitude anomalies that are recorded by more than one OBS. The seismic records for the shot lines that passed directly over specific OBSs are examined first since this yields the most conventional geometry.

Using this approach, I am able to identify waveform amplitude anomalies beneath shot lines. Changes in seafloor topography can also cause decreases in *P* wave energy by geometric scattering. To ensure that a change in topography did not create the disrupted and/or low-amplitude *P* waves, the topography is examined beneath each shot with anomalous waveforms. If a potentially anomalous region is inferred to have been caused by seafloor topography, the region is not further examined. The technique of examining the seismic records for the shot lines that passed directly over specific OBSs gives an idea of the possible number of anomalous regions and their proximity to the ridge axis.

After the potentially anomalous areas are located, *P* waves crossing through these regions from different azimuths and ranges are examined. If amplitude attenuation is also seen in these seismic records, it provides further support of the presence of potentially anomalous regions.

Section 3.3. Three-Dimensional Velocity Model and Ray Tracing

I determine if the potentially anomalous regions are detected as low-velocity bodies in the three-dimensional (3-D) velocity model of the Endeavour segment (Weekly et al., 2011). To create a 3-D velocity model, Robert Weekly picked a total of 96,515 *Pg* arrivals (*P* waves through the crust) for 62 of the OBSs. Robert Weekly inverted the *Pg* arrival times tomographically to create the 3-D velocity model, using the Stingray and TomoLab MATLAB codes developed by Doug Toomey at the University of Oregon. Picks are manually made using the picker MATLAB program created by William Wilcock at the University of Washington. An error value based on the uncertainty of each *Pg* arrival is assigned to each pick. The tomographic inversion accounts for the seafloor topography. I compare the 3-D velocity model to an averaged velocity model to see if amplitude anomalies are associated with low-velocity regions in the 3-D velocity model.

If the arrival times for the disrupted and/or low-amplitude *P* waves are included in the inversion to create the 3-D velocity model, the potentially anomalous regions may be present as low-velocity bodies in the velocity model. The modeled ray paths should bend around the amplitude anomalies if they are present as low-velocity bodies in the velocity model. The ray paths are found using the shortest path method with the 3-D velocity model. If the amplitude anomalies are too small, they may not be detected in the velocity model due to post-anomaly wavefront healing (Durant and Toomey, 2009). If the rays are found to bend around the potentially anomalous regions, this will provide further support for the interpretation that these zones of amplitude attenuation are associated with low-velocities and possible magma bodies. To create the 3-D velocity model, the majority of the disrupted and/or low-amplitude *Pg* arrivals were not included in the inversion,

making it very unlikely for the amplitude anomalies to be present as low-velocity bodies in the model.

By examining the ray paths through the potentially anomalous regions, I estimate the depths to the top of each region. The ray paths give a general idea of where *P* waves might interact with possibly anomalous regions. By examining the ray paths for seismograms that show disrupted and/or low-amplitude *P* waves, I can estimate the depth to the tops of each region. The following example shows how the maximum depth for the top of an amplitude anomaly is estimated from the shortest ray path. **Figure 3.2** shows the shortest time ray paths in the initial 1-D velocity model (Cudrak and Clowes, 1993) that was used to create the 3-D velocity model of the Endeavour segment. For a given line of shots, the shortest-range shot to the OBS that has a disrupted and/or low-amplitude *P* wave arrival is located 20 km from the OBS. The amplitude anomaly is presumed to be present somewhere along the ray path of that shot's *P* wave (i.e., white ray path starting 20 km from the OBS in **Figure 3.2**). The top of the amplitude anomaly would need to be at or above a depth of 3.2 km below seafloor (BSF) to interact with the ray path.

Section 3.4. Finite Difference Modeling

I use an elastic finite difference waveform propagation code, E3D (Larsen and Harris, 1993), with a two-dimensional (2-D) seismic velocity model that includes the seafloor topography to constrain the dimensions, depths, and physical properties of three of the best-observed potentially anomalous zones. The 2-D model is extracted from the velocity model of the Endeavour segment (Weekly et al., 2011) and consists of a 60 km

long, rise-parallel cross-section, which includes a ~2.5 km water column, ~5.9 km thick crust, 1 km thick Mohorovicic discontinuity (Moho) and ~2.7 km thick mantle region with a velocity of 7.8 km/s. The models are padded with a boundary that absorbs energy to avoid reflections off the model sides. A high attenuation boundary of quality factor (Q) equal to 5 is placed along the bottom and sides of the model. The crustal Vp/Vs ratios and Q values are from Durant and Toomey (2009) (**Appendix A**), and the crustal densities (ρ) are computed using the density-velocity relationship $\rho=0.165Vp+1.852$ (Christensen and Shaw, 1970). An anomalous volume is embedded in the crust. Several models are created with varying lengths, depths, and properties for the anomalous volume.

The central frequency for the OBSs modeled is found by plotting the power spectrum for the wave amplitude within a 0.8 s window around the initial arrival. The average largest wave amplitude is observed at 6 Hz for the OBSs examined (OBSs 29, 30, 31, 35, and 36). The stacked signal for shots within 10 km of OBS 35 as well as the amplitude power spectrum are shown in **Figure 3.3**. A Ricker wavelet with the identified central frequency of 6 Hz is used for the source in the E3D model. I generate synthetic seismograms from the models and compare these synthetics to the observed disrupted and/or low-amplitude *P* wave regions to constrain the properties and geometry of the anomalous volume. The synthetic data are band-pass filtered from 5 to 30 Hz.

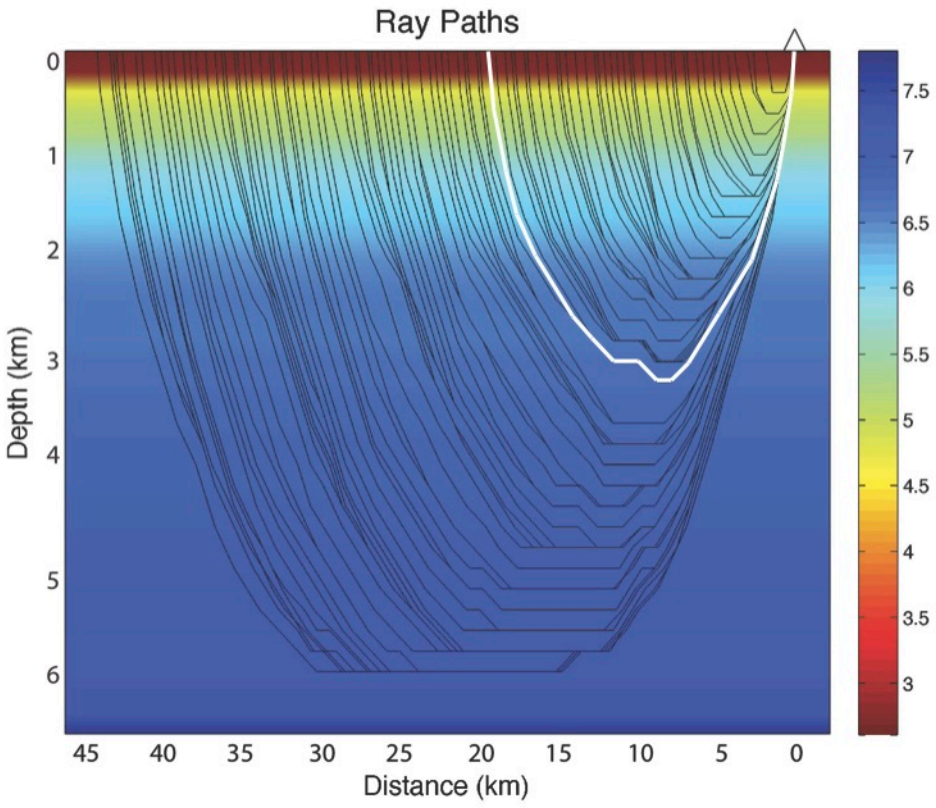

Figure 3.2. Shortest ray paths through a 1-D velocity model (Cudrak and Clowes, 1993) of oceanic crust without a water column. The triangle shows the location for the seismometer. The velocity is shown in km/s. Each source starts at 0 km depth and varying distances of 1.8 to 43.8 km from the instrument. The shortest path for a ray to travel from the source to the instrument is shown as the black lines. The white line shows the shortest ray path for a source 20 km from the instrument. The maximum depth the ray path travels from the source to the instrument is 3.2 km below seafloor (BSF). If this is the shortest-range shot to an OBS that has a disrupted and/or low-amplitude *P* wave arrival, then the maximum depth of the potentially anomalous region is 3.2 km BSF.

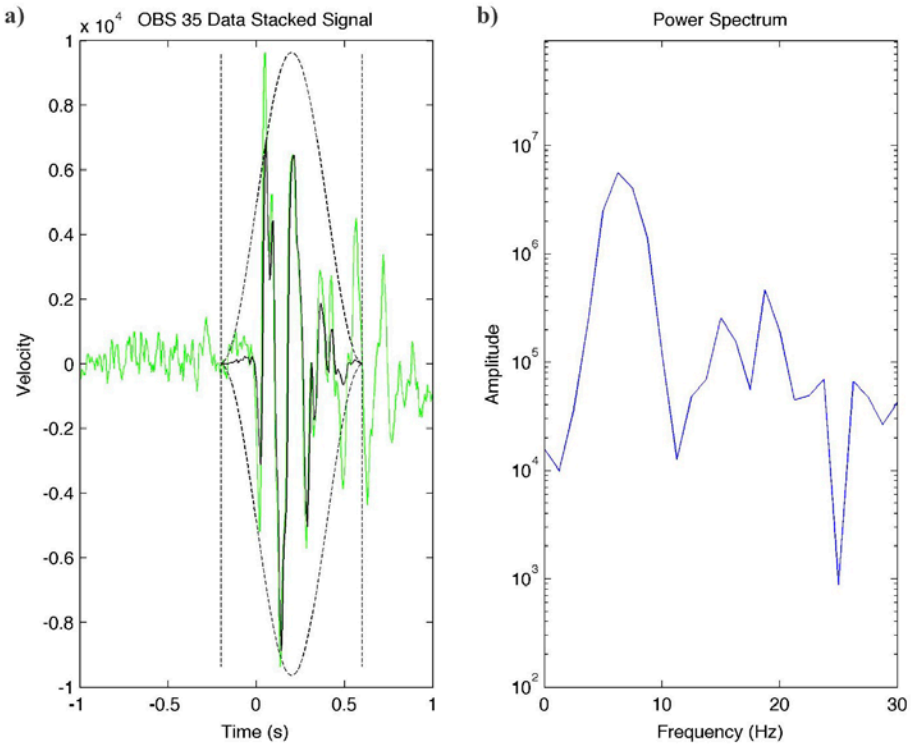

Figure 3.3. Stacked signal and power spectrum for OBS 35 shots 9099 through 9109. (a) The green line shows the signal of the stacked shots in a window of -1 to 1 s around the initial arrival time of the *P* waves. A Hanning window of -0.2 to 0.6 s is placed around the initial *P* wave arrival. The average signal after applying the Hanning window is shown by the black line. (b) The amplitude versus frequency is plotted for the stacked signal within the Hanning window. The largest amplitude is observed at ~6 Hz frequency.

CHAPTER IV

RESULTS

To investigate the presence of off-axis, crustal-level, low-velocity zones, I first examine the *P* wave profiles that cross directly over OBSs. I then verify any potentially anomalous region detected by examining the profiles for *P* waves crossing through the potentially anomalous regions from multiple azimuths and ranges. Lastly, I use ray tracing and finite difference modeling to estimate the dimensions, depths, and physical properties of several of the best-observed amplitude anomalies.

Section 4.1. Seismic Observations of Anomalous Waveforms

P Waves for Profiles Crossing Directly Over the OBSs

I examine shot sequences 2, 6, 8, 9, 20, and 42, which are directly over OBSs 1-36 and 57-63 and located more than 7 km from the ridge axis (**Figure 4.1**). The initial arrival of the *Pg* wave is picked for each seismometer. Disrupted and/or low-amplitude *Pg* waves are identified and picked as well. **Figure 4.2** shows seismic records with picked *Pg*, picked *dPg* (disrupted and/or low-amplitude *Pg*), and predicted *Pg* arrival times. The predicted *Pg* arrival times are created by ray tracing through the 3-D velocity model of Weekly.

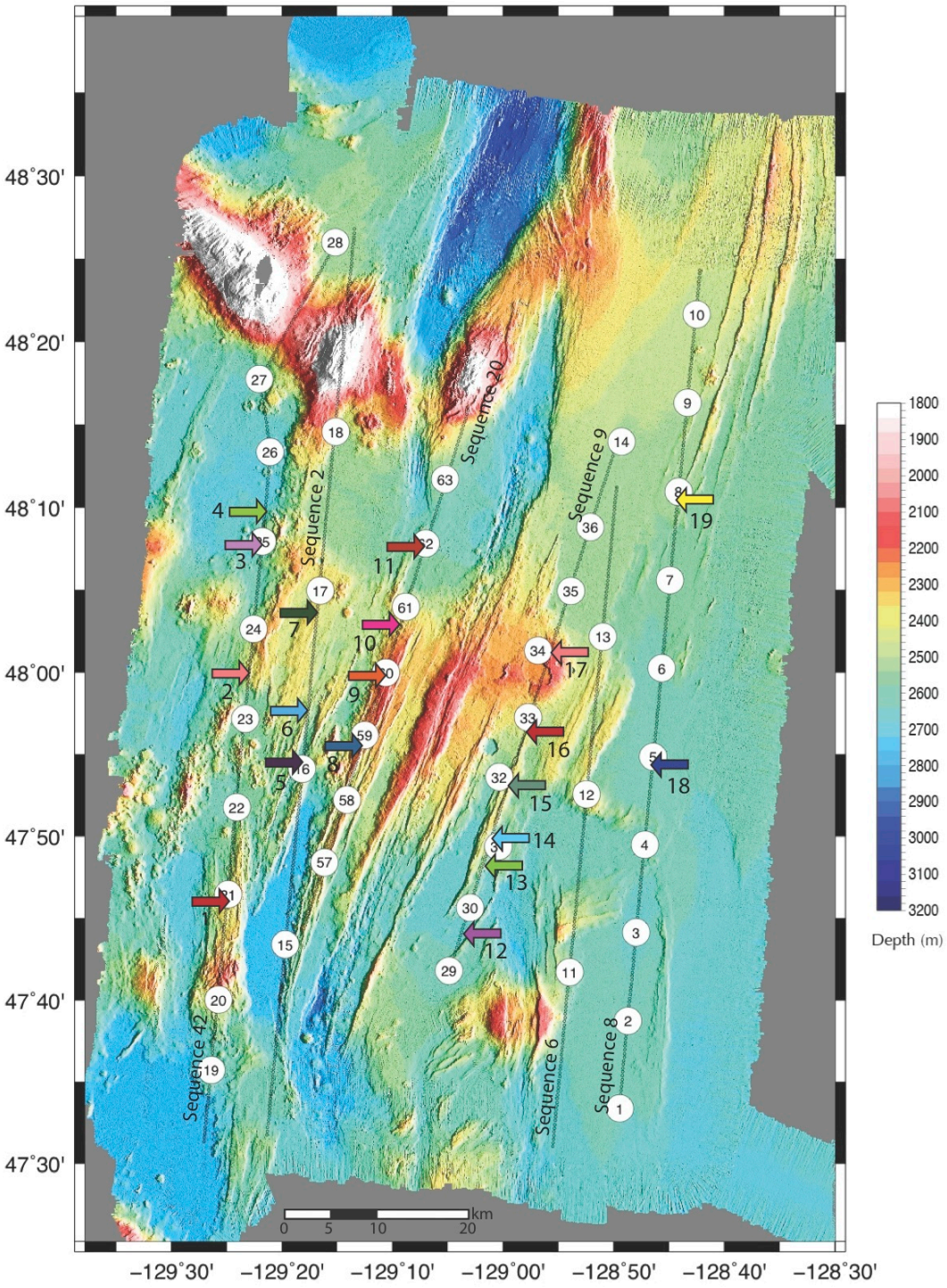

Figure 4.1. Bathymetric map of Endeavour segment with numbered arrows marking the location of the nineteen preliminary amplitude anomalies from the analysis of the overhead *P* waves. ETOMO shot locations that are examined are shown by small black circles, and the OBS locations that are examined are shown by the larger, white circles with each OBS's number in the middle. The scale shows the surface depth.

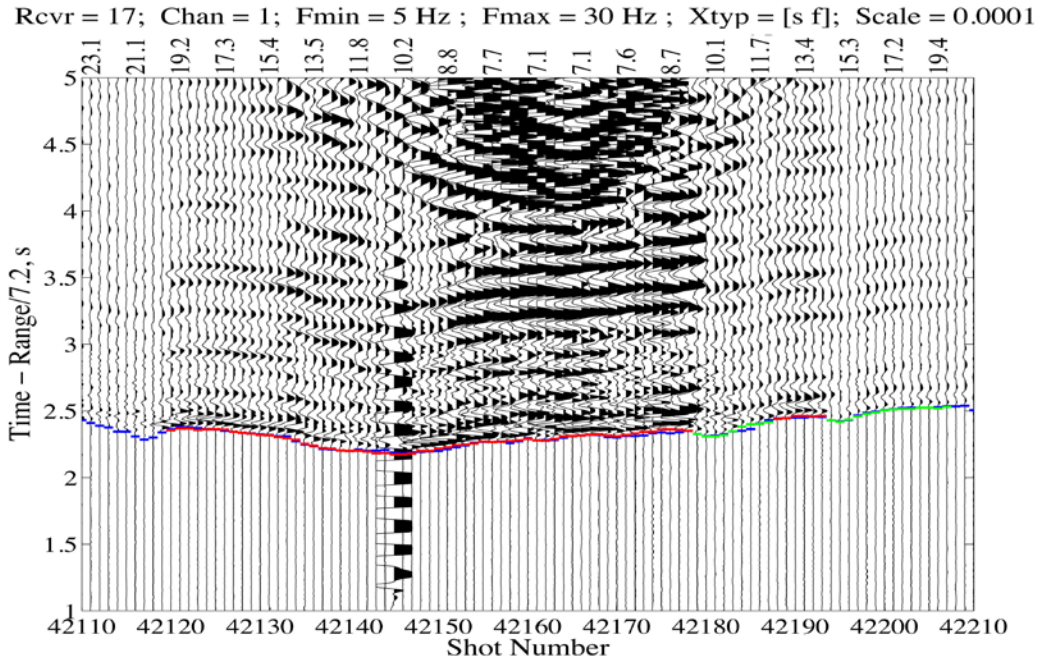

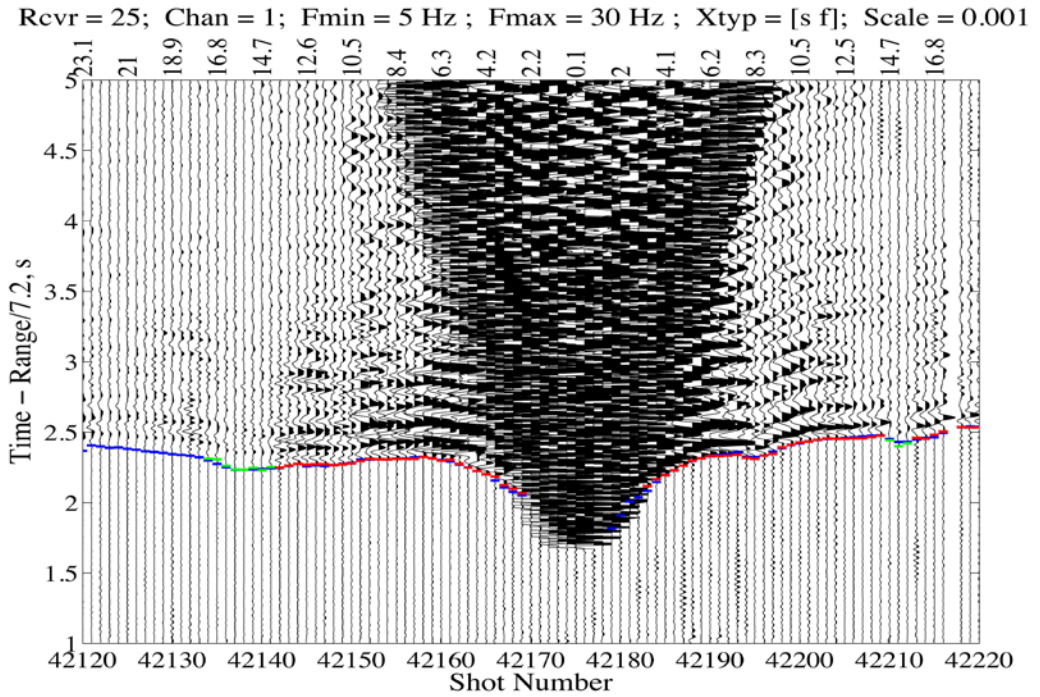

Figure 4.2. Seismic records for OBS 17 and 25 with shot sequence 42. The picked *Pg* (red), picked *dPg* (green), and predicted *Pg* (blue) arrival times are shown by colored lines. Shot numbers are listed below each figure; the range of the shot to the OBS is shown above the figures. The record sections are fixed scale, plotted with a velocity reduction of 7.2 km/s, and are band-pass filtered between 5 and 30 Hz.

To find potential low-velocity, high-attenuation regions, I compare the seismic records for OBSs 1-36 and 57-63 along specific shot lines, positioning the seismic records from north to south. I look for anomalous waveforms that occur in localized geographic regions. A low-velocity, high attenuation region may not always yield localized anomalous waveforms, but localized anomalous waveforms can provide evidence of an anomalous region (Durant and Toomey, 2009; Canales et al., 2012). From this approach, I identify several regions with considerable and concentrated decreases in wave amplitude, suggesting an attenuation of energy due to an anomalous region in the mid-crust (Durant and Toomey, 2009; Canales et al., 2012).

To verify each potentially anomalous region, I use the following criteria. I look for a region with anomalous waveforms that is at least 1km wide. The amplitude anomalies must be observed at multiple ranges from the OBSs. The amplitude anomalies must be visible in the seismic records of seismometers that are located both north and south of the amplitude anomaly. I rank the amplitude anomalies in accordance to the amount of wave amplitude decrease that is visible in the seismic records (3 – the highest rank to 1 – the lowest rank). These values are listed in **Appendix B**. Using these criteria, I am able to make a preliminary identification and ranking of the amplitude anomalies.

I also examine the topography at the locations of each amplitude anomaly to determine if topography could have caused the decrease in wave amplitude. **Figure 4.3** shows an example of a decrease in *Pg* amplitude that is inferred to be caused by topography. The shot amplitudes decrease within the same region (between the mauve lines) for both the northern and southern OBSs, indicating there was geometric scattering

at the seafloor surface. The location that waveform amplitude decreases is where the shots go over the crest of a ridge.

From this analysis, I identify a total of nineteen preliminary, potentially anomalous regions; their locations are shown in **Figure 4.1**. These amplitude anomalies are found by comparing OBSs 19 – 27 with shot sequence 42, OBSs 15B – 18 with shot sequence 2, OBSs 57 – 63 with shot sequence 20, OBSs 29 – 36 with shot sequence 9, OBSs 11 – 14 with shot sequence 6, and OBSs 1 – 10 with shot sequence 8. The amplitude anomalies are shown in **Appendix C** by the series of OBSs that best demonstrate each area of anomalous waveforms. The average length for all of the identified amplitude anomalies is approximately 3 km. The largest region, 13, is ~7 km in length, whereas the smallest region, 3, is 1.5 km in length. The amplitude anomalies are observed at multiple ranges from the OBSs. The closest range is 4 km for region 12 (OBS 8 with shot sequence 8), and the furthest range is 54 km for region 18 (OBS 30 with shot sequence 20). The amplitude anomalies are consistent on seismic records for multiple OBSs that are located both north and south of the amplitude anomalies. The relative wave amplitude decrease varies for each amplitude anomaly. An example would be that region 16 shows very clear decreases in wave amplitude on five OBSs (average rank of 3 for five OBSs), whereas region 1 shows little amplitude decrease (average rank of 1.3 for four OBSs). Details of the observations for each potentially anomalous region can be found in **Appendix B** (**Tables B.1** and **B.2**).

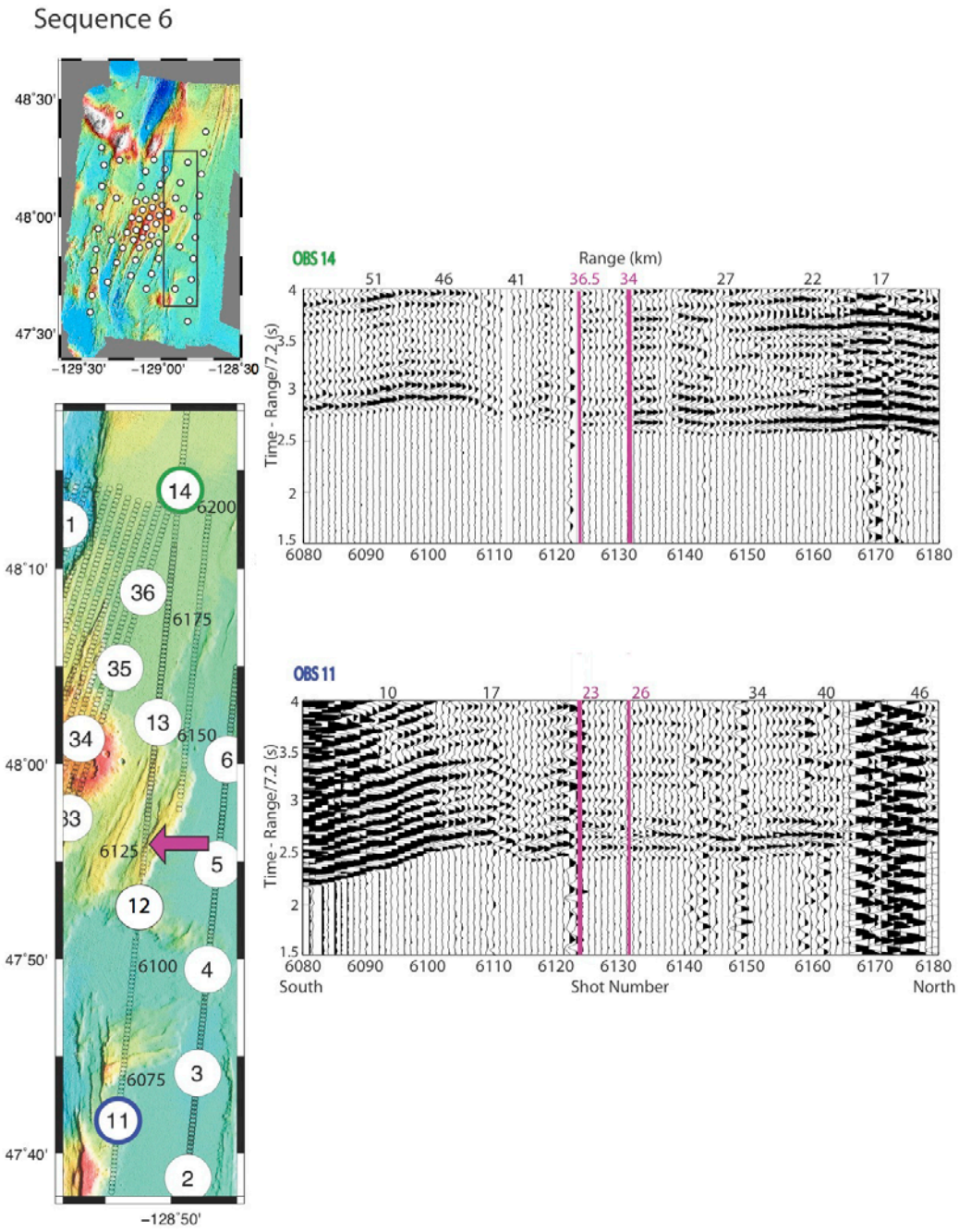

Figure 4.3. Example of topography causing a localized decrease in amplitude. Seismic records for OBSs 11 and 14 are shown with shot sequence 6 on the vertical channel. The bold magenta line shows the range and shot number where the *P* phase's amplitude decreases. These seismic records show an example of how seafloor topography can cause a decrease in wave amplitude. The location of the amplitude decrease region, shown by a magenta arrow on the bathymetric map, is at the top of a ridge where there is a rapid change in seafloor topography. The record sections are fixed scale, plotted with a velocity reduction of 7.2 km/s, and are band-pass filtered between 5 and 30 Hz.

Region 16 is the best-observed anomalous region (**Figure 4.4).** Compared to **Figure 4.5**, an example where no localized region of wave amplitude decrease is observed, a very clear loss in wave amplitude is observed in **Figure 4.3**. The bold red lines show the initial locations where the wave amplitude decreases for the *Pg* phase. The location of the *Pg* phase amplitude decrease depends on the geometry of the OBS and the amplitude anomaly (**Figure 4.6**). For the seismometers north of the amplitude anomaly (OBSs 36 and 35), the wave amplitudes decrease south of the red line (**Figure 4.4** – left side of the line). This happens because the shots' *P* waves travel directly through the region. North of the red line, the shots' *P* waves do not travel through this region on their path to the OBS, indicating that either the anomalous volume is deeper than the direct wave path from the shot to the OBS or that the anomalous volume is located further south than the shot. The reverse is observed for the seismometers south of the region (OBSs 31, 30, and 29). The shots' *P* wave amplitudes decrease north of the red line (right side of the line) since these shots travel directly through the region, whereas south of the red line, the shots' *P* waves do not travel through region on their path to the OBS. The ray paths of the shot numbers where the *P* phases' amplitudes first decreases for each OBS is shown in **Figure 4.6**.

Figure 4.4 (next page). Region 16 identified by *P* waves for profiles crossing directly over the OBSs. Seismic records for OBSs 29, 30, 31, 35, and 36 are shown with shot sequence 9 on the vertical channel, except for OBSs 31 and 35 (due to technical issues with the vertical channel, the hydrophone is utilized). The bold red lines show the ranges and shot numbers where the *P* phase's amplitude first decreases. The thinner red lines show where the zones of lowered amplitude end. The location of the initial amplitude decrease is shown by red arrow, #16, on the bathymetric map in **Figure 4.1**. The blue lines show the predicted *P* wave arrivals. The record sections are fixed scale, plotted with a velocity reduction of 7.2 km/s, and are band-pass filtered between 5 and 15 Hz.

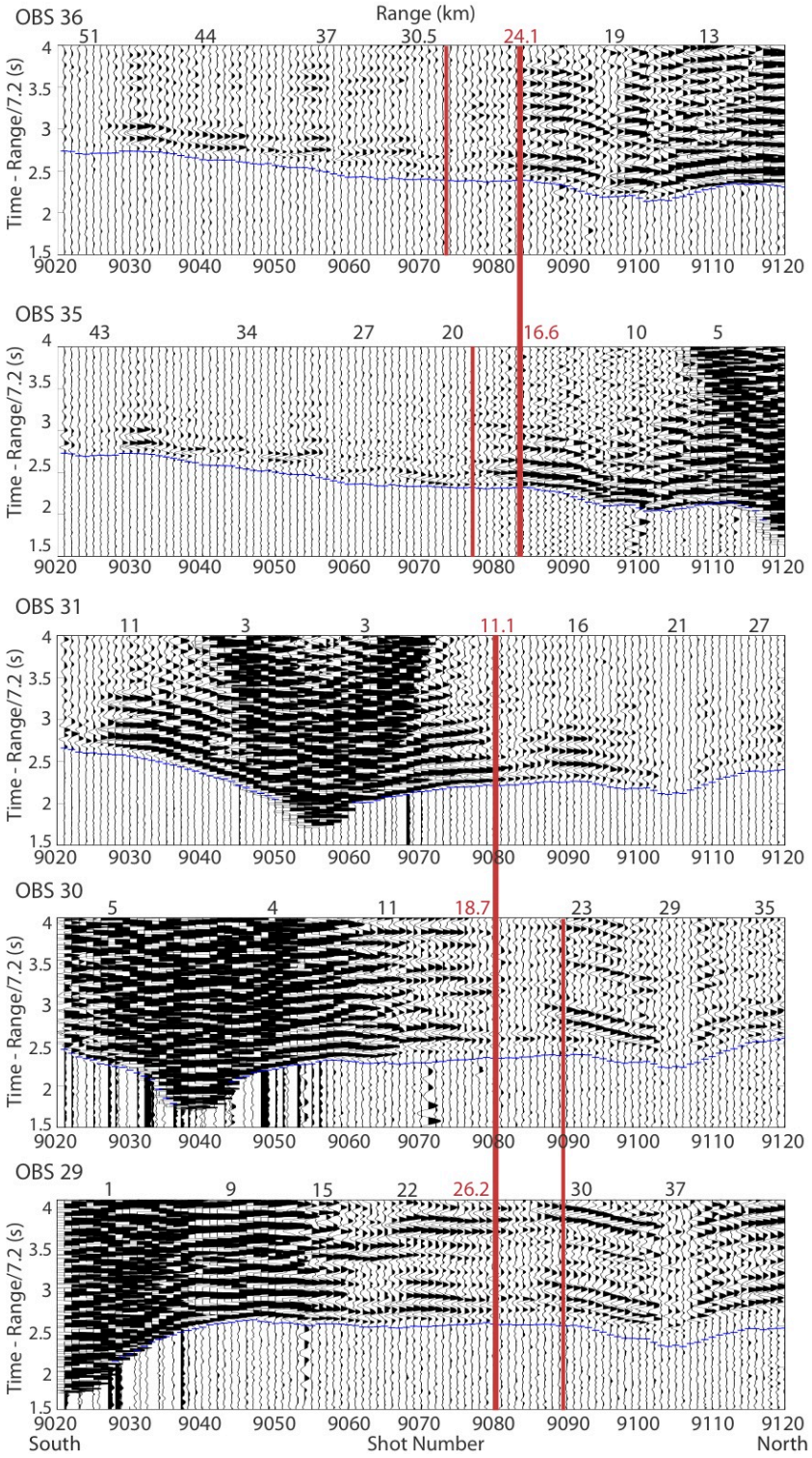
OBS 36
Range (km)
51
44
37
30.5
24.1
19
13
OBS 35
43
34
27
20
16.6
10
5
OBS 31
11
3
3
11.1
16
21
27
OBS 30
5
4
11
18.7
23
29
35
OBS 29
1
9
15
22
26.2
30
37
Time - Range/7.2 (s)
4
3.5
3
2.5
2
1.5
9020
9030
9040
9050
9060
9070
9080
9090
9100
9110
9120
South
Shot Number
North

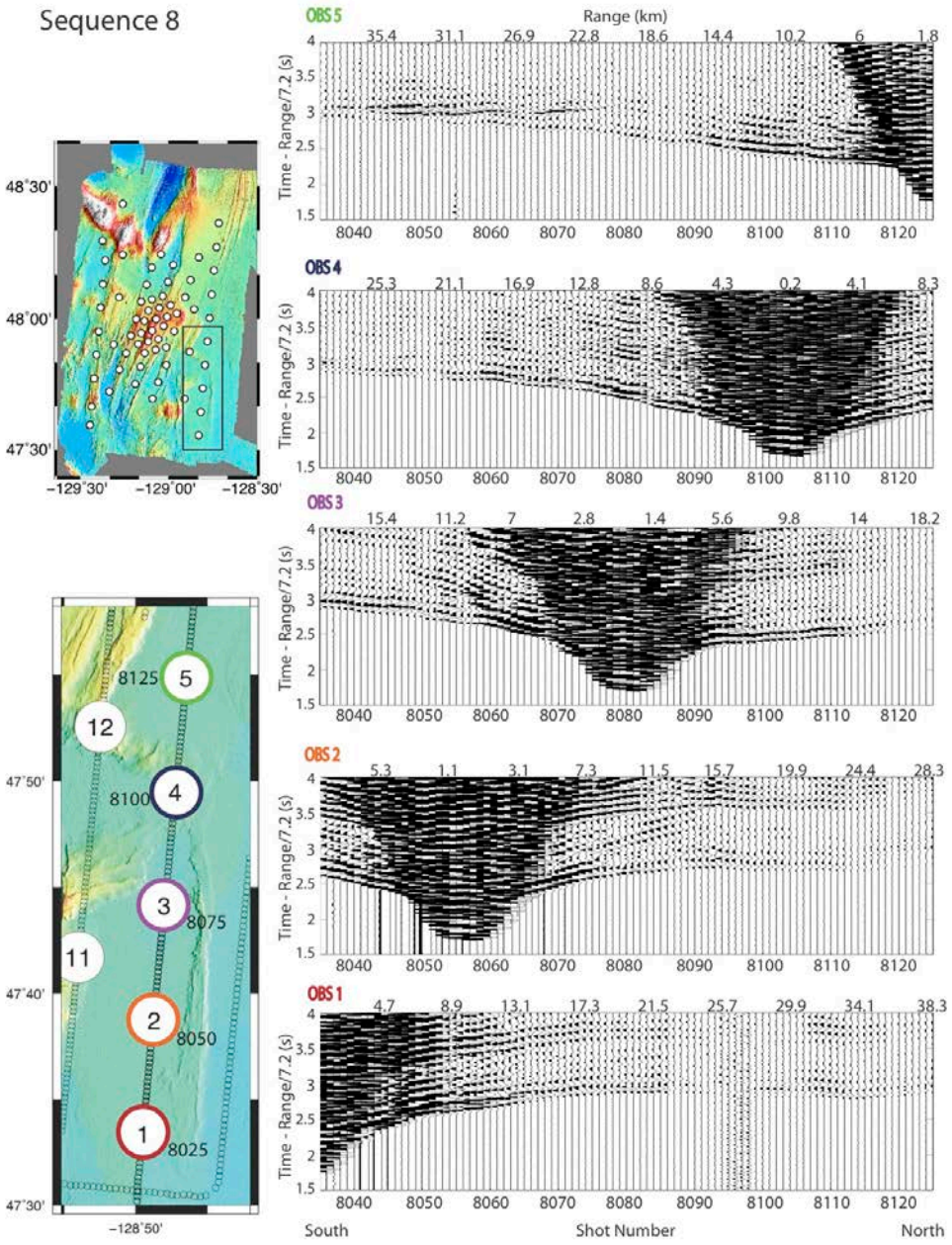

Figure 4.5. Example of a series of OBS seismic records where no localized decreases in amplitude is observed. Seismic records for OBSs 1 through 5 are shown with the shot sequence 8 on the vertical channel, except for OBS 5 (due to technical issues with the vertical channel, the hydrophone is utilized). There are visible areas with disrupted and/or low-amplitude *P* waves that could be caused by an anomalous body in the crust, but since none of these regions are localized from more than one direction, they are inferred to be caused by an unknown crustal structure (faults, crustal topography buried beneath sediment, heterogeneities in the crust, etc.). The record sections are fixed scale, plotted with a velocity reduction of 7.2 km/s, and are band-pass filtered between 5 and 30 Hz.

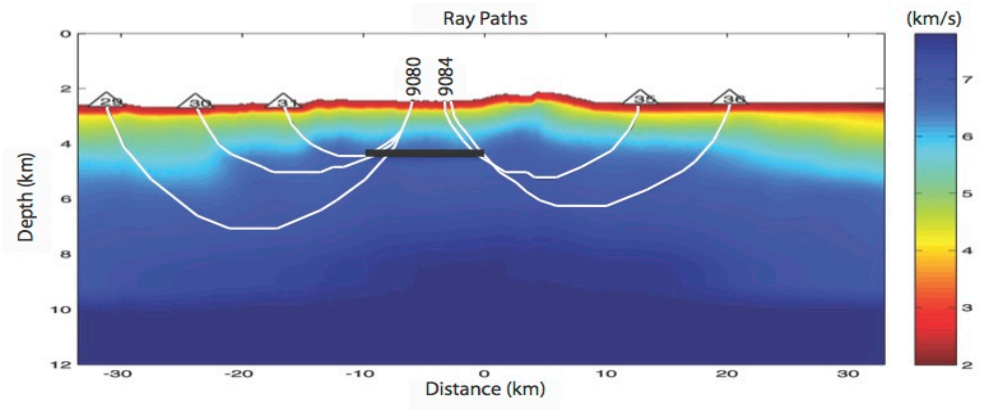

Figure 4.6. Ray paths of the shortest-range shots for each OBS, where the disrupted and low-amplitude *P* wave arrivals are first observed for region 16. By using the shortest ray path (white lines) as a guide, the amplitude anomaly would need to be at a shallowest depth of 2 km BSF (determined by OBS 31) and would need to be 10 km wide to cause the disrupted and low-amplitude waves. These dimensions are shown by the thick black line.

The localized region of *P* wave amplitude loss for region 16 has similar waveform characteristics to the attenuated arrivals observed by Canales et al. (2012) and Durant and Toomey (2009) for highly attenuated bodies at the East Pacific Rise. Durant and Toomey (2009) found *P* wave energy remains attenuated at longer ranges, indicating that the region extends into the lower crust, which is similar to the waveform characteristics observed for region 16.

P Waves for Profiles Crosscutting Through the Anomalous Volumes

The second approach I use to confirm that each amplitude anomaly is an anomaly in the crust is to examine the seismic records of *P* waves crossing from multiple directions through each of the identified nineteen amplitude anomalies (**Appendix D**). I use similar criteria for verifying each anomalous volume as when I examined the seismic record sections of *P* waves crossing directly over the OBSs. I look at seismic records for

P waves crossing from multiple directions. Due to the locations of some of amplitude anomalies along the outer edges of the ETOMO survey region (regions 1 – 4, 18), I am only able to look at two seismic records for these amplitude anomalies. For the rest of the amplitude anomalies, I examine three or more (up to fifteen for region 16) seismic records for crosscutting *P* waves. I identify *P* waves that cross directly through the region. For the amplitude anomaly to be considered an anomaly in the crust, these *P* waves must show a decrease in their *P* wave energy. The amplitude anomalies' rankings are listed in **Appendix B** (**Tables B.3** and **B.4**).

The lengths of the potential anomalous regions observed for individual seismic record sections range from 0.5 to 6.8 km with an average of 2.1 km. The largest region with anomalous waveforms observed from crosscutting *P* waves is region 9, an average length of 2.7 km, whereas the smallest is region 13, an average length of 1.2 km. The range of lengths observed for the amplitude anomalies on individual seismic record sections is much larger than the average lengths for each region. The amount of wave amplitude decrease varies between amplitude anomalies and also between individual record sections for a particular anomaly because it is dependent on the distance from the OBS to the shot location. Region 7 shows an example of a very subtle decrease in wave amplitude (**Appendix D**, **Figure D.4**, OBS 24 with shot sequence 17 and OBS 61 with shot sequence 42). Region 9 shows an example of a very evident decrease in wave amplitude (**Appendix D**, **Figure D.6**, OBS 17 with shot sequence 13) and also a very large area of wave amplitude decrease (**Appendix D**, **Figure D.6**, OBS 16 with shot sequence 22). All of the observations are ranked (3 – a very evident decrease in wave amplitude to 0 – no visible decrease in wave amplitude; **Appendix B**, **Table B.5**).

Localized decreases in amplitude for *P* waves crossing through region 16 are shown in **Figures 4.7 and 4.8**. By examining the crosscutting *P* waves with the above criteria, I am able to eliminate twelve of the previously identified amplitude anomalies. These regions are eliminated because I am not able to verify wave amplitude decreases from multiple directions and ranges. Due to the close proximity, ~2 km, for the locations of regions 13 and 14, the two regions are combined as region 13-14. The final six identified amplitude anomalies are shown in **Figure 4.9**. Details of the observations of the *P* waves for profiles crosscutting through each amplitude anomaly can be found in **Appendix B** (**Table B.5**).

Section 4.2. Three-Dimensional Velocity Model and Ray Tracing

I examine the ray paths of the shot sequences used in the profiles of *P* waves crossing directly over the OBSs (**Section 4.1**) to check if the amplitude anomalies are present as low-velocity regions in the 3-D velocity model. No rays are observed to bend around any of the amplitude anomalies. I also examine the velocity perturbations to see if low velocities are detected at the amplitude anomaly locations in the 3-D velocity model. None of the final six identified amplitude anomalies are observed in the 3-D velocity model. The majority of the picked *dPg* were not included in the inversion to create the 3-D model, which explains why the final six identified amplitude anomalies are not observed in the 3-D velocity model. **Figure 4.10** shows the velocity model, shot coverage, and velocity perturbations for shot sequence 9 and beneath this sequence. For region 16, little to no difference in velocity is seen at its location (10 km length, -8 to 2 km on the x-axis and 2 km thickness, 3.5 to 5.5 km on the y-axis).

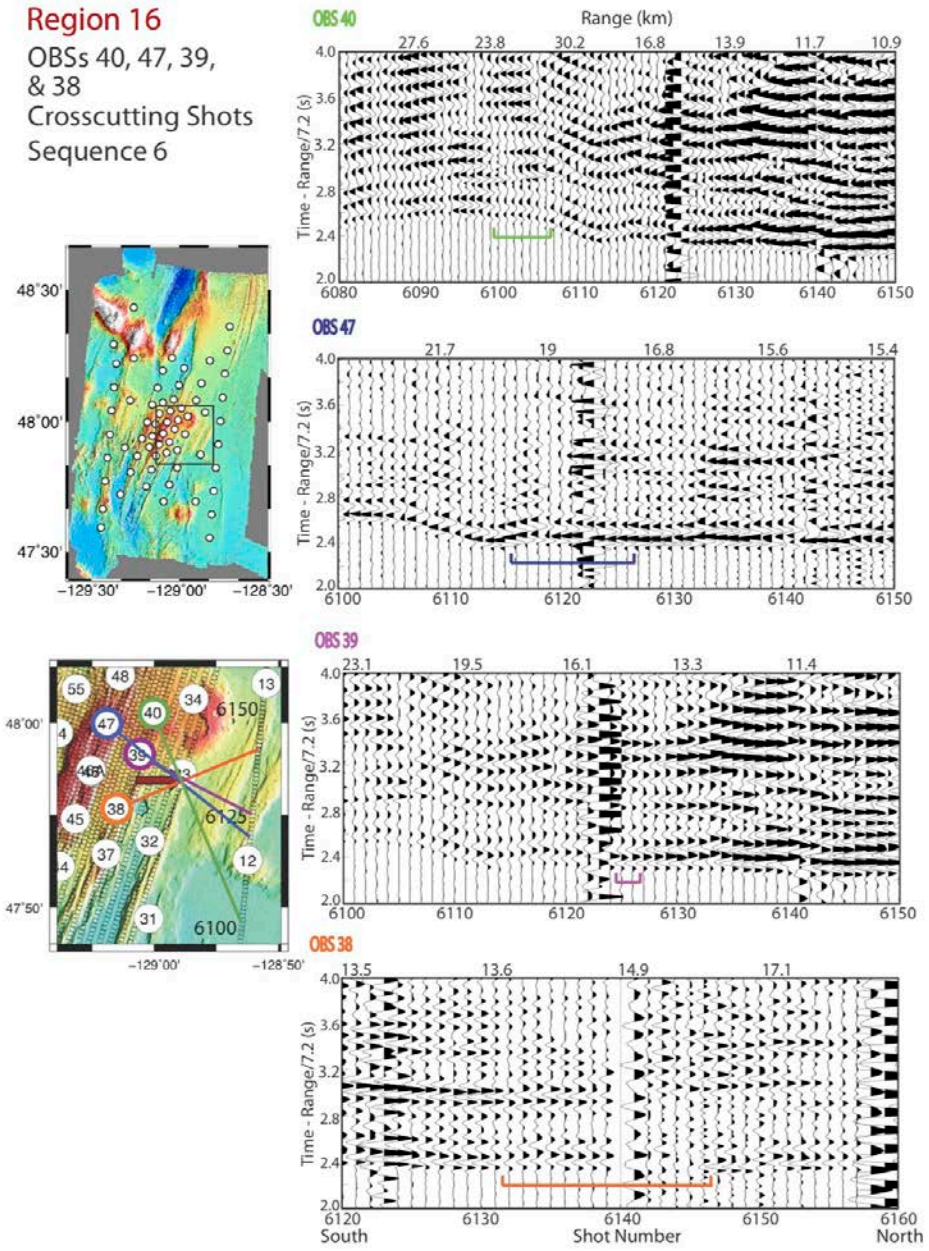

Figure 4.7. Region 16 shown by *P* waves for profiles crosscutting through the region from the eastern direction. Seismic records (OBSs 40, 47, 39, 38) are shown with shot sequence 6 for *P* wave paths crossing through the amplitude anomalies at various angles on the vertical and hydrophone channel. On the seismic records, the colored bars show the shots with attenuated *P* wave arrivals. The paths of the attenuated waves are shown on the map by a corresponding colored line. Very little loss in wave amplitude is observed for the seismic records, due to the close range between the OBSs and the amplitude anomaly. OBSs at greater ranges are not examined since wave paths would cross through the rise axis, potentially interacting with the magma chamber. The record sections are fixed scale, plotted with a velocity reduction of 7.2 km/s, and are band-pass filtered between 5 and 15 Hz.

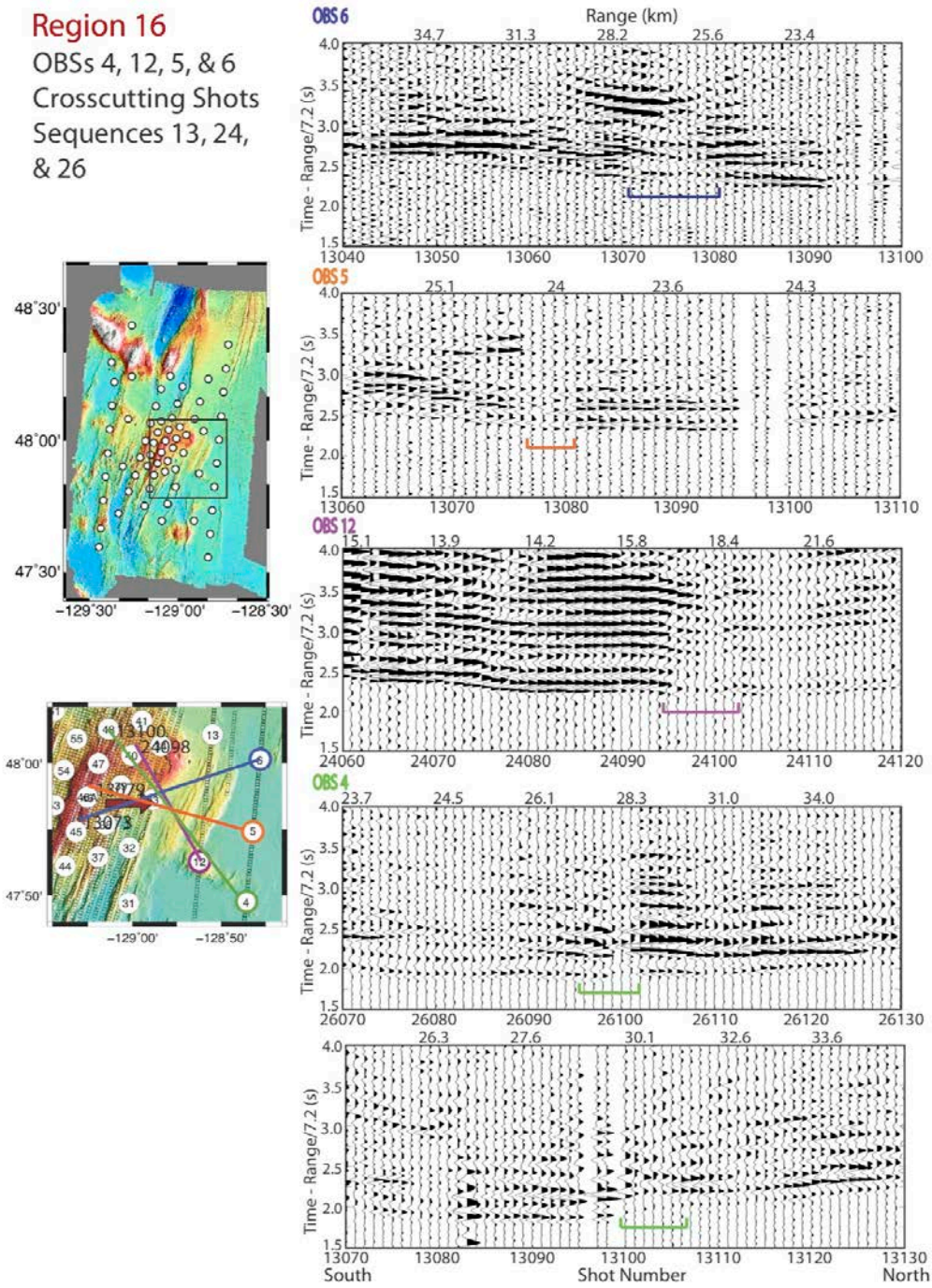

Figure 4.8. Region 16 shown by *P* waves for profiles crosscutting through the region from the western direction. Seismic records (OBSs 6, 5, 12, 4) are shown with shot sequences 13, 24, and 26 for *P* wave paths crossing through the region at various angles on the vertical and hydrophone channels. On the seismic records, the colored bars show the shots with attenuated *P* wave arrivals. The paths of the attenuated waves are shown on the map by a corresponding colored line. A clear loss in wave amplitude is seen in all the seismic records. The record sections are fixed scale, plotted with a velocity reduction of 7.2 km/s, and are band-pass filtered between 5 and 15 Hz.

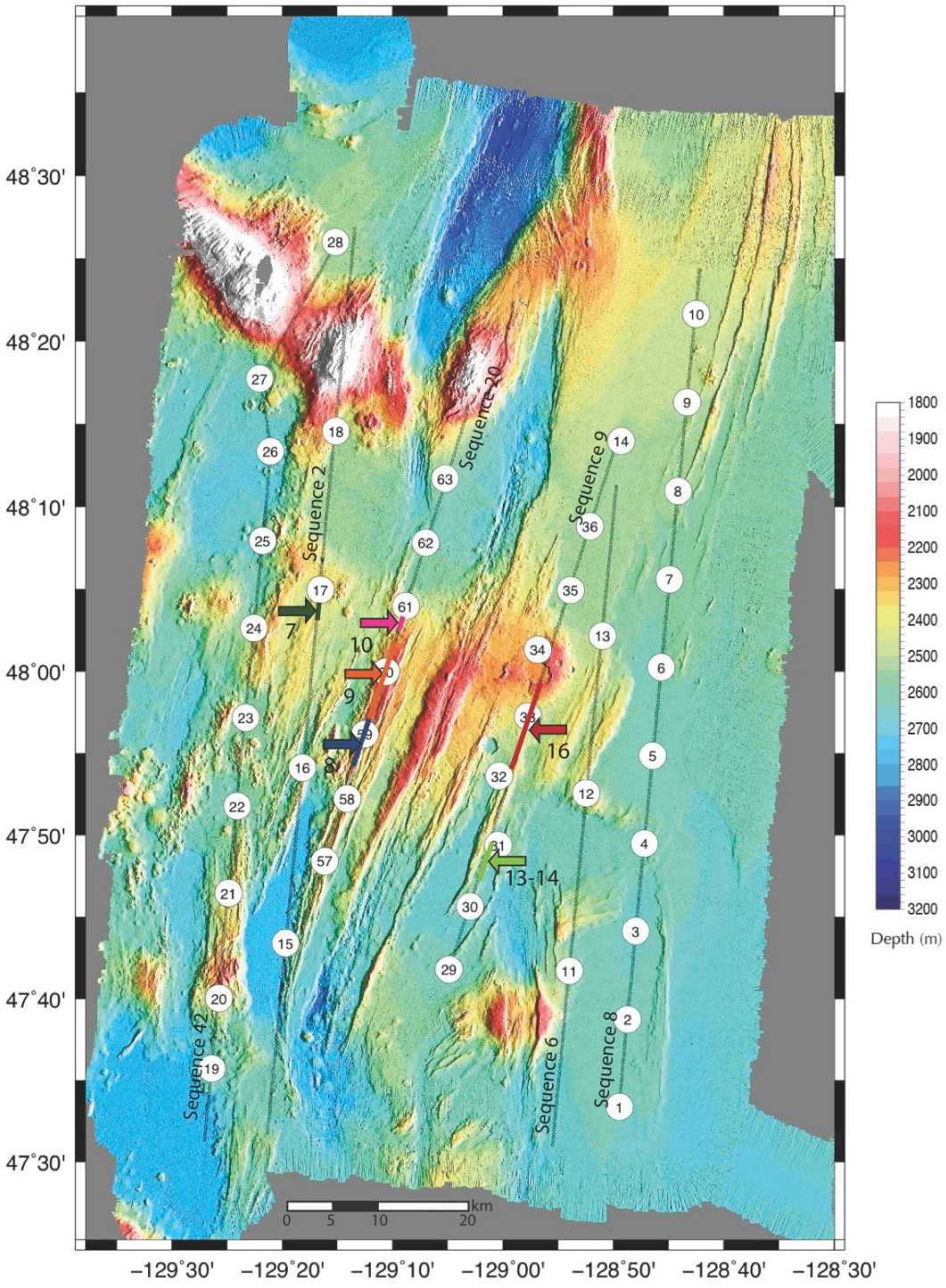

Figure 4.9. Bathymetric map of Endeavour segment with colored arrows marking the final six locations of the identified amplitude anomalies. The sizes of the regions are shown by the corresponding colored lines next to the arrows. The regions' sizes are estimated from the seismic observations, except for region 8 (blue line), region 9 (orange line), and region 16 (red line), which are inferred from finite difference modeling.

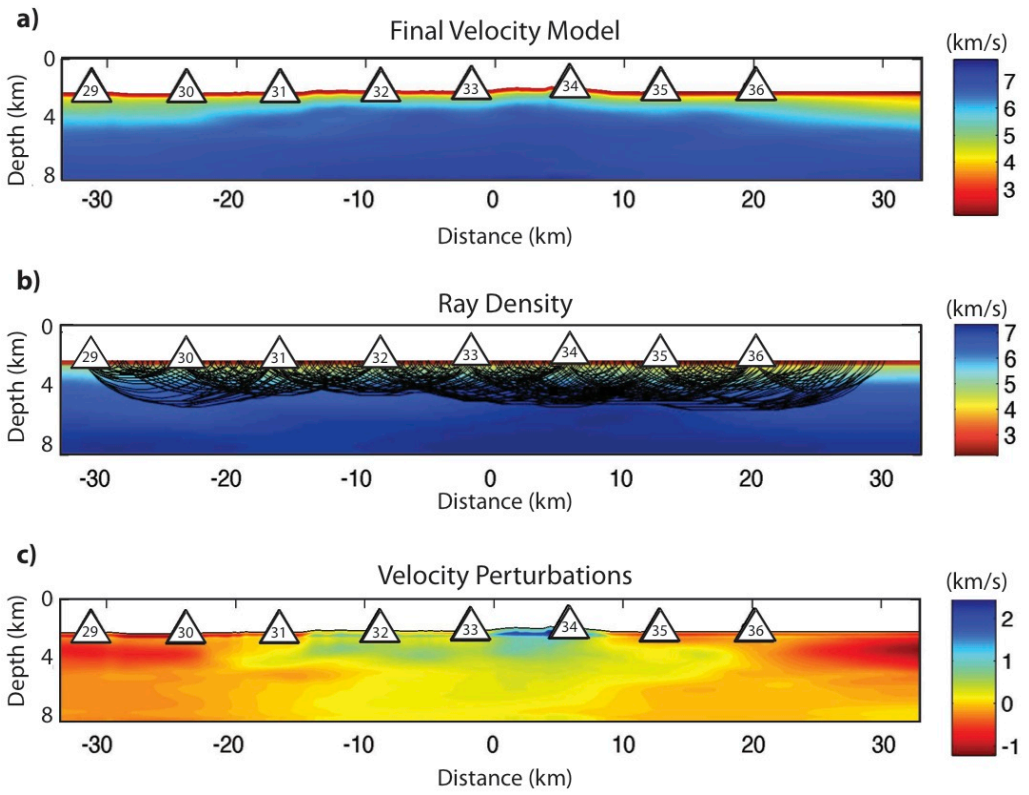

Figure 4.10. 3-D velocity model, ray coverage, and velocity perturbation for shot sequence 9. OBSs located beneath shot sequence 9 are shown by the white triangles (**Figure 4.9**). (a) The 3-D velocity model is beneath shot sequence 9. (b) Ray density coverage for shot sequence 9. **c)** Velocity difference between the 3-D velocity model and an average of the 3-D velocity model (3-D velocity model minus averaged 3-D velocity model). There is no visible anomaly in the velocity model for the area where region 16 is located (-8 to 2 km on the x-axis and 3.5 to 5.5 km on the y-axis, which is 2 to 4 km BSF). The anomaly is likely not present in the 3-D velocity model due to the majority of picked *dPg* not being included in the inversion to create the 3-D model.

I estimate the depth for the top of each amplitude anomaly by identifying the shortest-range shot with a disrupted and/or low-amplitude *P* wave for the profiles directly over the OBSs (**Appendix C**). The maximum feasible depth for the top of each amplitude anomaly is set to the turning depth of the *Pg* ray path. The maximum depths for the top of each amplitude anomaly are recorded in **Appendix B**.

For region 16, the *Pg* ray paths for the shortest-range shots with disrupted and/or low-amplitude *P* waves are shown in **Figure 4.4** for the five OBSs from **Figure 4.3**. The shortest range where wave amplitude loss is observed is ~12 km (OBS 31, shot 9080). The *Pg* ray path of a *P* wave traveling from shot 9080 to OBS 31 shows that the maximum depth for top of region 16 is 2 km BSF. At this depth, region 16 would be 10 km wide to cause the disrupted and/or low-amplitude waves for the shortest-range shots on each of the five OBSs.

Section 4.3. Finite Difference Modeling

To constrain the dimensions, depths, and physical properties of the amplitude anomalies, I forward model the three amplitude anomalies that are best-observed from the *P* waves crossing directly over the OBSs and crosscutting through the region. Based on my seismic observations, regions 16, 9, and 8 are the best-observed anomalous regions. I also investigate the other amplitude anomalies by comparing the observed arrivals to synthetic waveform models without an anomalous region.

Best-Observed Amplitude Anomaly, Region 16

Region 16, located beneath a ridge on the east flank of the segment (**Figure 4.9** – red arrow) is the best-observed amplitude anomaly. I vary the length, depth, and physical properties of the anomalous volume in order to find a model whose resultant waveform and travel time anomalies are comparable to the observed arrivals (**Figure 4.11**, **4.12**, and **4.13**). I model the overhead shots (shot sequence 9) for the five OBSs that best show the disrupted and low-amplitude *P* wave arrivals (**Figure 4.3** – OBSs 29, 30, 31, 35, and 36). The disrupted and attenuated *P* waves I observe in the seismic data (**Figure 4.3**) are very

similar to the decreased waveform amplitudes in both Durant and Toomey (2009) and Canales et al. (2012)'s studies. Based on the similarity of these waveforms, I test whether the decreases in waveform amplitude are the product of a magma sill and/or a region with lower velocity and increased attenuation in the crust.

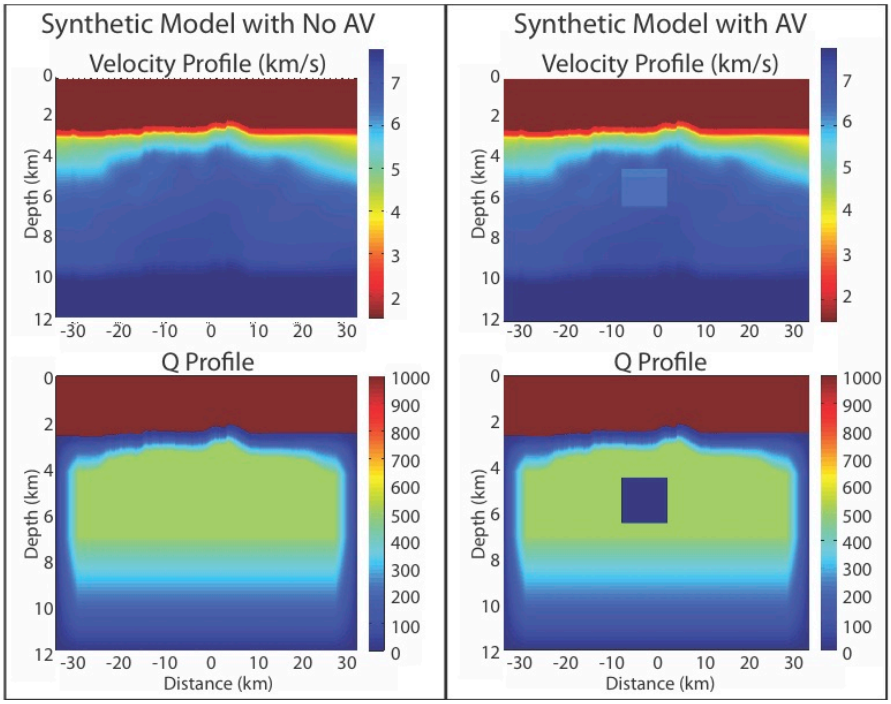

Figure 4.11. Velocity and attenuation profiles for the synthetic models (region 16). The left column shows the synthetic model with no anomalous volume; the right column shows the best-fit synthetic model with a 10 km wide, 2 km thick, and 2 km BSF, a *Q* value of 10, and a decrease in velocity of ~8%. These velocity and attenuation profiles are used in E3D to create the synthetic records in **Figures 4.12** and **4.13**.

To quantitatively compare the models with the observations, I use the $\log_{10}$ of the root-mean-square (RMS) of the waveform amplitude to compare the amount of amplitude decrease for the synthetic models to that observed for the five OBSs. I use a time window of -0.01 to 0.1 s from the initial arrival time of each wave to measure the change in

amplitude for selected shot arrivals (**Figure 4.14**). The small time window is used to avoid measuring any of the secondary phases. An example of the time window can be seen in the seismic record for OBS 35 (**Figure 4.15**). I compare the average of the arrival waves' amplitudes for shots that do not encounter the anomalous volume to the low-amplitude waves' amplitudes (**Figure 4.16**).

The observed *P* wave arrivals show a decrease in amplitude by a factor of 2.5 as the waves encounter the anomalous volume (**Figure 4.16**). To match this decrease in wave amplitude, I create several synthetic anomalous regions, varying the values listed in **Table 4.1**. I model low-velocity, high-attenuation regions and magma sills, both together and separately. I compare all of the synthetic models' wave amplitudes to the observations.

Figure 4.12 (next page). Synthetic seismic records for shot sequence 9 without an anomalous volume compared to the observed arrivals. The red lines show the locations where *P* wave amplitude decreases are detected in the observed arrivals (right column). In the synthetic seismic records (left column), no *P* wave amplitude decrease is seen in the regions that are detected in the observed arrivals. *P* wave arrivals are shown by the blue lines. These synthetic seismic records show little wave energy loss, which is different from the seismic records in **Figure 4.5**, which are for an area of the Endeavour segment where no localized areas of wave amplitude decrease are visible in the data. The loss of wave energy in the data could be from anomalous regions within the crust, but since none of the regions are localized from more than one direction, they are inferred to be caused by an unknown crustal structure (faults, crustal topography buried beneath sediment, heterogeneities in the crust, etc.). The green and blue lines show the locations where *P* wave amplitude decreases are detected in the observed arrivals for region 13 (**Appendix C**, **Figure C.12**) and region 14 (**Appendix C**, **Figure C.13**), respectively. For regions 13 and 14, no *P* wave amplitude decrease is seen in the regions that are detected in the observed arrivals. The velocity and *Q* values versus depth that are used in the finite difference model are shown in **Figure 4.11**.

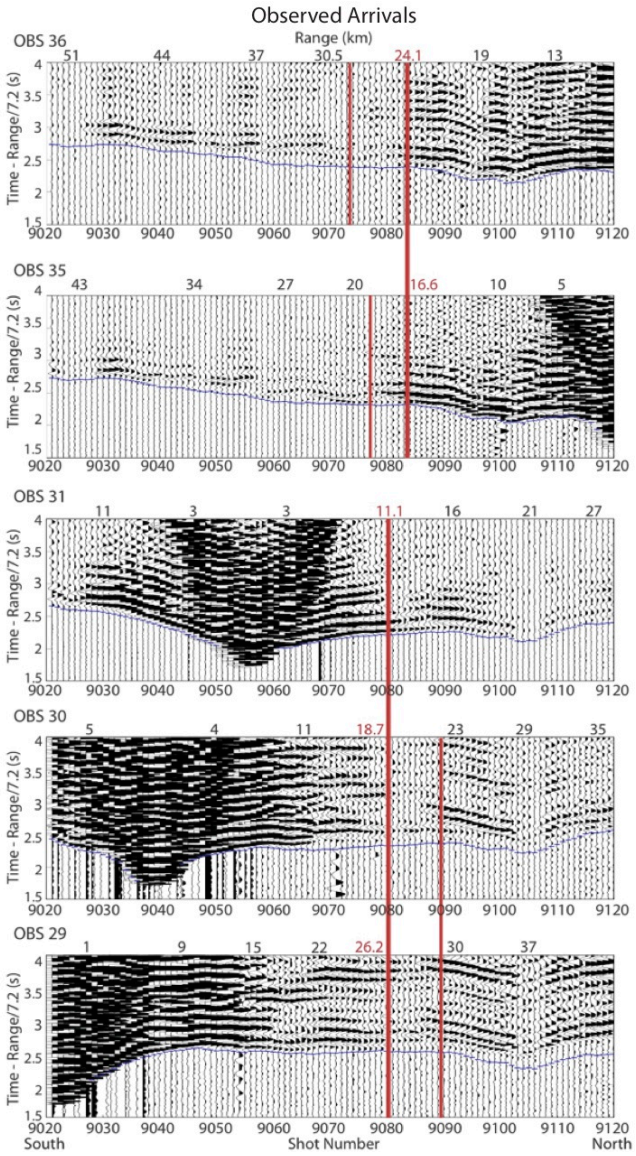
Observed Arrivals
Range (km)
OBS 36
51 44 37 30.5 24.1 19 13
OBS 35
43 34 27 20 16.6 10 5
OBS 31
11 3 3 11.1 16 21 27
OBS 30
5 4 11 18.7 23 29 35
OBS 29
1 9 15 22 26.2 30 37
Time - Range/7.2 (s)
4 3.5 3 2.5 2 1.5
9020 9030 9040 9050 9060 9070 9080 9090 9100 9110 9120
South
Shot Number
North

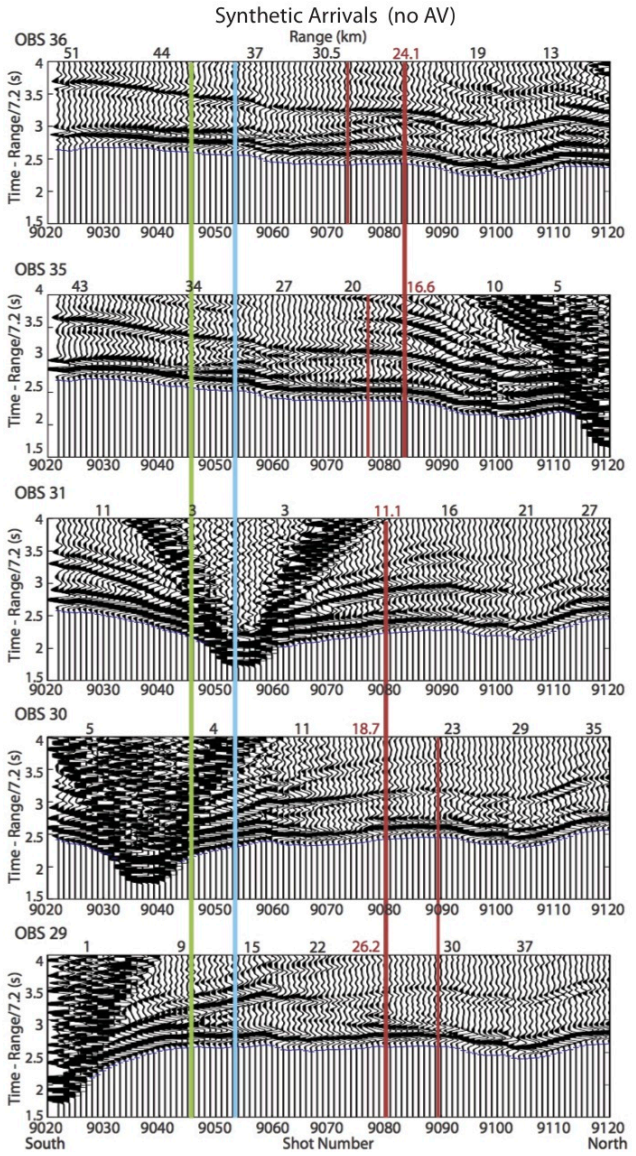
Synthetic Arrivals (no AV)
Range (km)
OBS 36
51 44 37 30.5 24.1 19 13
OBS 35
43 34 27 20 16.6 10 5
OBS 31
11 3 3 11.1 16 21 27
OBS 30
5 4 11 18.7 23 29 35
OBS 29
1 9 15 22 26.2 30 37
Time - Range/7.2 (s)
4 3.5 3 2.5 2 1.5
9020 9030 9040 9050 9060 9070 9080 9090 9100 9110 9120
South
Shot Number
North

The parameters varied in **Table 4.1** affect the *P* wave arrivals in the seismic records. The anomalous volume's dimensions (vertical and along-axis length) determine the number of shots with *P* wave arrivals that are attenuated for each seismometer; the longer the anomalous volume or the greater its vertical length, the greater the number of shots that are attenuated. An along-axis length greater than 10 km increases the range of low-amplitude arrivals more than is observed, whereas along-axis lengths less than 10 km decreases the range of low-amplitude arrivals to be less than is observed. A vertical length greater than 2 km creates larger ranges of attenuated arrivals than is observed, whereas less than 2 km does not create the necessary range of attenuated arrivals. Vertical lengths greater than 2 km also cause a loss in *P* wave energy at further ranges than is observed.

Figure 4.13 (next page). Synthetic seismic records for the best-observed amplitude anomaly (region 16) compared to the observed arrivals. The amplitude anomaly's location is shown by the red line on the map in **Figure 4.9**. The green tinted box on each synthetic seismic record (left column) shows the length (10 km) and location of the anomalous volume compared to the shot numbers. A similar *P* wave amplitude decrease is seen in the regions that are detected in the observed (right column). *P* wave arrivals are shown by the blue lines. On the synthetic seismic records, the green and blue lines show the locations where *P* wave amplitude decreases are detected in the observed arrivals for region 13 (**Appendix C**, **Figure C.12**) and region 14 (**Appendix C**, **Figure C.13**), respectively. As seen in the synthetic model with no anomalous volume (**Figure 4.12**, right column), no *P* wave amplitude decrease is seen in the regions that are detected in the observed arrivals for regions 13 and 14. The velocity and *Q* values versus depth that are used in the finite difference model are shown in **Figure 4.11**.

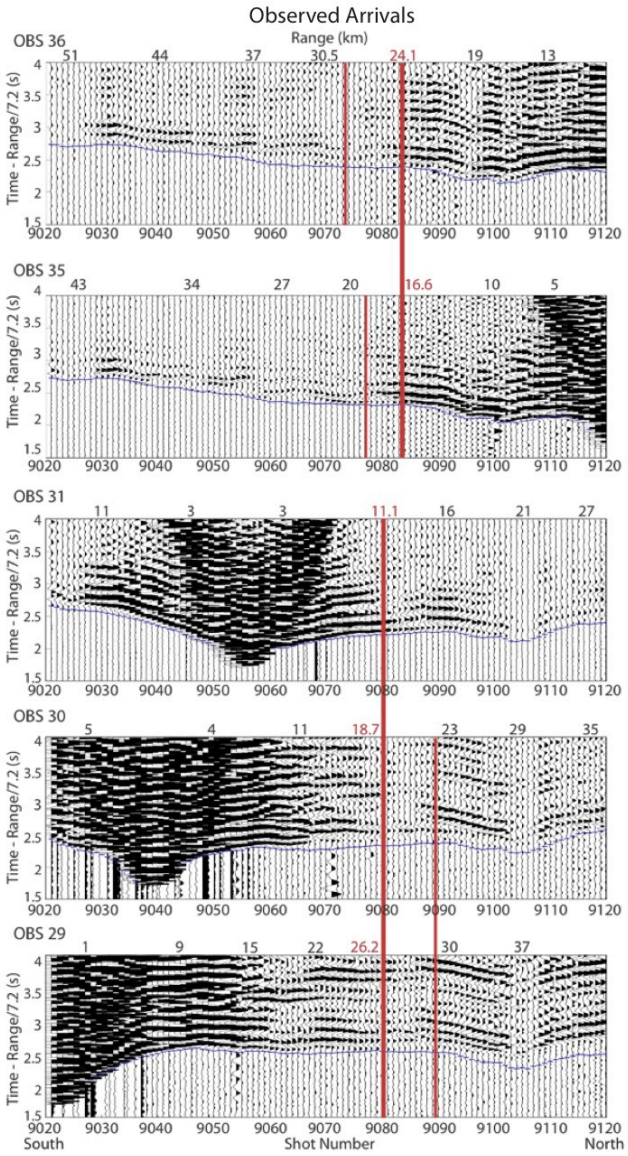
Observed Arrivals
Range (km)
OBS 36
51 44 37 30.5 24.1 19 13
OBS 35
43 34 27 20 16.6 10 5
OBS 31
11 3 3 11.1 16 21 27
OBS 30
5 4 11 18.7 23 29 35
OBS 29
1 9 15 22 26.2 30 37
Time - Range/7.2 (s)
4 3.5 3 2.5 2 1.5
9020 9030 9040 9050 9060 9070 9080 9090 9100 9110 9120
South
Shot Number
North

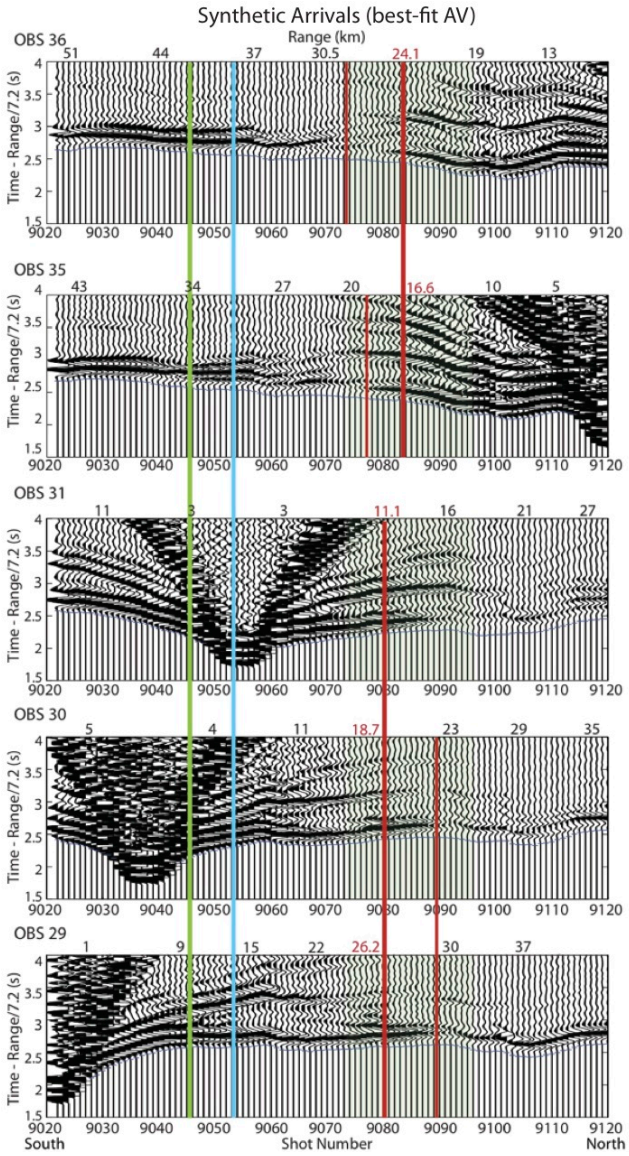
Synthetic Arrivals (best-fit AV)
Range (km)
OBS 36
51 44 37 30.5 24.1 19 13
OBS 35
43 34 27 20 16.6 10 5
OBS 31
11 3 3 11.1 16 21 27
OBS 30
5 4 11 18.7 23 29 35
OBS 29
1 9 15 22 26.2 30 37
Time - Range/7.2 (s)
4 3.5 3 2.5 2 1.5
9020 9030 9040 9050 9060 9070 9080 9090 9100 9110 9120
South
Shot Number
North

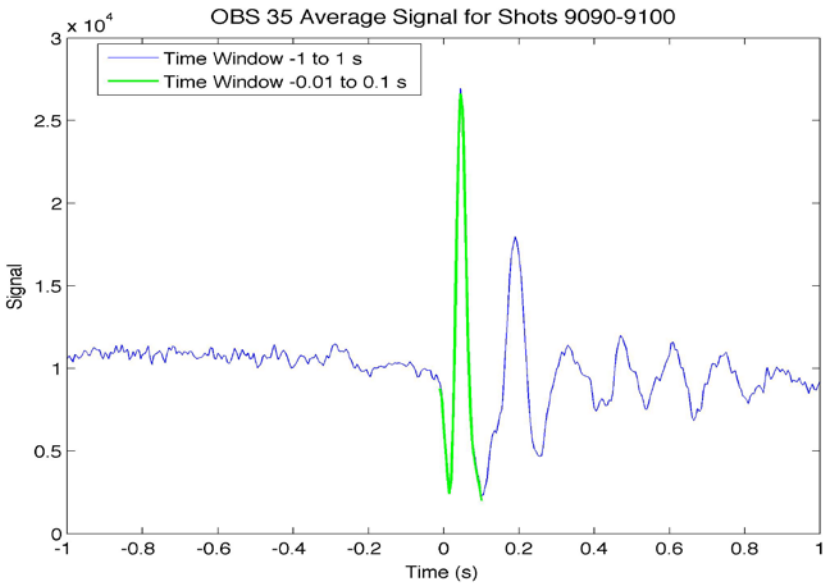

Figure 4.14. The average signal for shots 9090-9100 on OBS 35. The blue line is the average signal. The green line shows the average signal within a time window of -0.01 to 0.1 s, which is used for the amplitude comparison. Shots 9090-9100 are located ~9.8 to ~14.3 km from OBS 35.

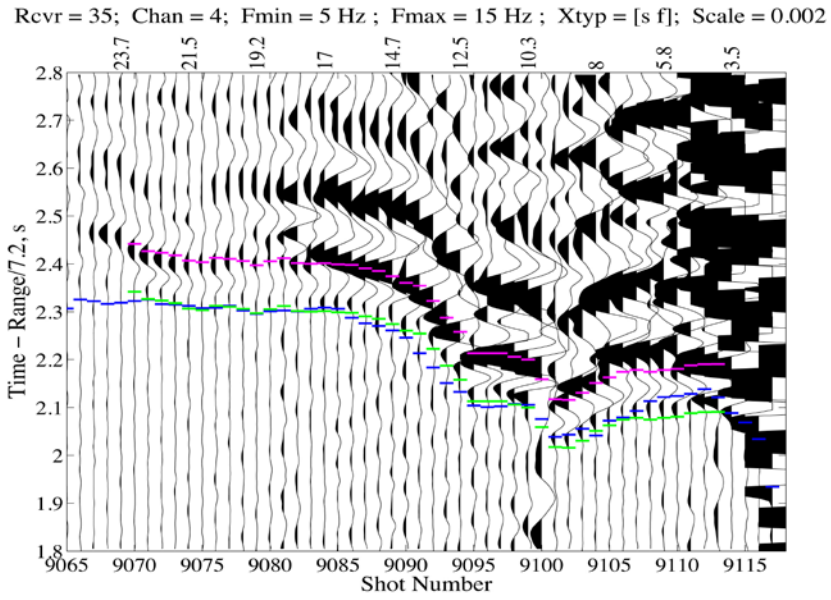

Figure 4.15. OBS 35 seismic record with the waveform window used for amplitude comparison. The green line shows the initial arrival time, and pink line shows the initial arrival time plus 0.1 s. The blue line shows the predicted arrival times. The waveform amplitudes of shots 9070 to 9113 are compared with synthetic models to constrain the amplitude anomaly.

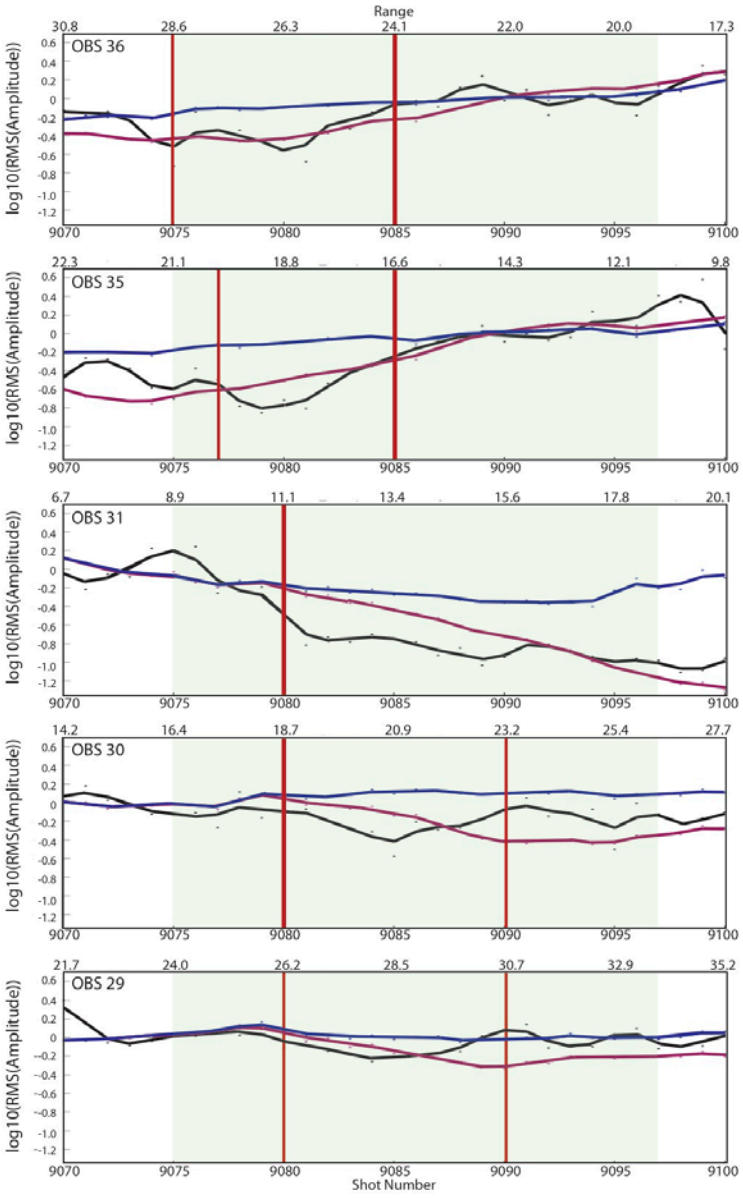

Figure 4.16. The log10 of the RMS of the *P* wave's amplitude (-0.01 to 0.1 time window) is compared for OBSs 29, 30, 31, 35, and 36. The observed arrivals (black line), synthetic model with no anomalous volume (blue line), and the best-fit synthetic model with an anomalous volume (mauve line) are compared. The green tinted box on each seismic record shows the length (10 km) and location of the anomalous volume compared to the shot numbers. The bold red lines show the ranges and shot numbers where the observed arrivals' *P* phase amplitude first decreases (same locations as **Figure 4.3**), and the darker tinted box shows the range of *P* waves that are disrupted and attenuated. The synthetic model with an anomalous volume shows a similar loss in wave amplitude as the observed, whereas the synthetic model with no anomalous volume shows no visible loss in wave amplitude. The amplitudes are normalized by a 5 to 10 shots at close range to each OBS.

Anomalous Volume	Depth (km)	Along-Axis Length (km)	Vertical Length (km)	Percent Velocity Decrease (%)	*Q* Value
Low-Velocity, High-Attenuation Region	1.8 - 4	1 - 11	0.1 - 4	0 - 27	5 - 40
Magma Sill	1.8 - 4	1 - 6	0.1 - 2	40 - 60	1000

Table 4.1. Anomalous volume values varied in synthetic models for region 16. The numbers show minimum and maximum of the ranges of values used in the models.

The anomalous volume's depth BSF also determines the number of shots with attenuated arrivals; the shallower the anomalous volume, the closer the initial attenuated arrival is seen on each OBS. From plotting the ray paths, the maximum depth BSF of for region 16 is 2 km. Modeling anomalous volumes at depths greater than 2 km does not create a decrease in amplitude for the shots closer to the OBS that show amplitude loss in observed arrivals. Modeling anomalous volumes at depths shallower than 2 km has the opposite effect. An example of how the along-axis length and depth BSF affect the number of shots with attenuated arrivals is shown in **Figure 4.6**.

The attenuation and velocity change the amount of wave energy loss. The higher the attenuation (lower *Q* value) or the greater the velocity decrease, the more amplitude is lost. Because both the attenuation and velocity reduction affect the amount of energy that is lost, there is a tradeoff between these values. Thus, the exact values of *Q* and the velocity decrease cannot be determined.

The best-fit model to match the number of shots with attenuated *P* wave arrivals on the five OBSs is an anomalous volume that is 10 km wide, 2 km thick, and 2 km BSF.

These parameters match the length and maximum depth estimated from the shortest ray paths for the shortest-range shots with disrupted *P* waves (**Figure 4.4**). The best-fit model to match the amount of wave amplitude decrease is an anomalous volume with a *Q* value of 10 and a decrease in velocity of ~8% (**Figure 4.11**). Little change in wave amplitude is noticed when modeling a sill. To match the ranges of the low-amplitude arrival from the north and south, a length of 10 km best fits the observed arrivals. Because of the tradeoff between velocity and attenuation change, I am unable to determine the exact *Q* value and the velocity decrease; however, I find a *Q* value of 10 with a velocity decrease of 8 create a similar loss in wave energy as in the observed arrivals.

The synthetic seismic records for the model without an anomalous volume (**Figure 4.12**) are compared to the model with the best-fit anomalous volume (**Figure 4.13)**. The same scaling is used for both figures. A localized decrease in wave amplitude in the synthetic anomalous volume model matches the observed (**Figure 4.3**). The model verifies that an anomalous volume with high attenuation in the mid- to lower-crust can cause the decreases of wave amplitude of the first arrivals.

To determine if the anomalous region can be resolved by delay-time tomographic methods, I compare the *P* wave arrival times for synthetic models (**Figure 4.17**). The *P* wave travel time for the synthetic model without an anomalous volume is compared to the *P* wave arrival time for the observed (black line), predicted (light blue line), and the best-fit synthetic model with an anomalous volume (mauve line) for OBSs 29, 30, 31, 35, and 36. The time difference is found by subtracting the observed, predicted, and synthetic (best-fit anomalous volume) from the synthetic (no anomalous volume). A positive value means the synthetic (no anomalous volume) arrival time is slower than the other arrivals;

a negative value means the synthetic (no anomalous volume) arrival time is faster than the other arrivals. The travel time delays for the anomalous volumes are shown in **Table 4.2**. Raising and lowering the velocity decrease of the anomalous volume affects the time delay for the *P* arrivals that interact with the anomalous region. The higher percent velocity decrease for the anomalous region, the greater the time delays for the *P* arrivals.

The best-fit anomalous volume model has an average travel time delay of 44 ms for the five OBSs, which should be detectable in the 3-D velocity model. Since the majority of the disrupted and/or low-amplitude *P* arrivals were not included in the inversion, the travel time delay is not detected. In **Figure 4.17**, shots 9070 through 9100 are shown for the five OBSs where the anomalous volume is observed. Only 14 *P* wave arrivals with travel time delays from interacting with the anomalous volume are included in the inversion. These 14 arrivals with travel time delays are recorded by OBS 35 (shots 9070 through 9084). For OBSs 29, 30, and 36 the *P* wave arrivals that interacted with the anomalous volume were either too disrupted or out of range to pick the arrival times. For OBS 31, the arrival times for shots 9070 through 9095 were included in the inversion, but as can be seen in **Figure 4.17**, these arrival times were not delayed when compared to the synthetic model without an anomalous volume. Due to the majority of disrupted and/or low-amplitude arrivals not being included in the inversion, the anomalous regions are not resolved by delay-time tomographic methods.

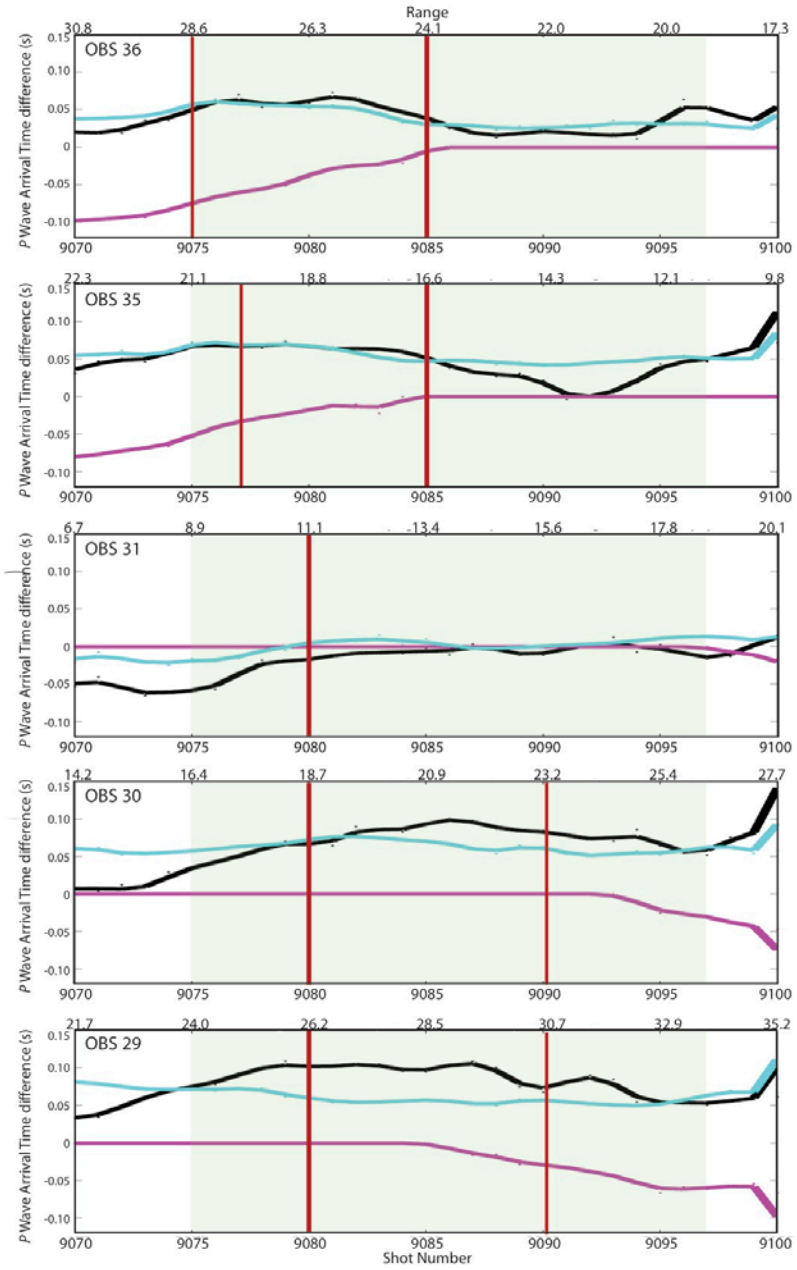

Figure 4.17. The travel time of the synthetic model without an anomalous volume *P* wave arrival time compared to the observed (black line), predicted (light blue line), and synthetic model with the best-fit anomalous volume (mauve line) for OBSs 29, 30, 31, 35, and 36. The time difference is found by subtracting the observed, predicted, and synthetic (best-fit anomalous volume) from the synthetic (no anomalous volume). The green tinted box on each seismic record shows the length (10 km) and location of the anomalous volume compared to the shot numbers. The bold red lines show the ranges and shot numbers where the observed arrivals' *P* phase amplitude first decreases (same locations as **Figure 4.4**). A positive value means the synthetic (no anomalous volume) arrival time is slower than the other arrivals; a negative value means the synthetic (no anomalous volume) arrival time is faster than the other arrivals.

OBS	OBS distance from shot sequence 9 (m)	Anomalous Volume delay time (ms)
29	110	50
30	240	38
31	1,040	10
35	130	53
36	220	67

Table 4.2. The travel time delays for the anomalous volume. The second column shows the distance of the OBS from shot sequence 9. The third column shows the average difference between the travel times for the synthetic model without an anomalous volume compared to the synthetic model with the best-fit anomalous volume (absolute value of the synthetic model without an anomalous volume –synthetic model with best-fit anomalous volume) for the shots affected by the anomalous volume (**Figure 4.17** – shots right of the left red line for OBSs 35 and 36 and right of the bold red line for OBSs 29, 30, and 31). The delay time values are listed as positive to show the amount of time delay, but the values are actually negative because the synthetic model with the best-fit anomalous volume is slower for that time interval. For all the OBSs, the average travel time delay caused by the anomalous volume is 44 ms.

For finite difference modeling, all the OBSs are placed directly beneath shot sequence 9, but in the ETOMO study, the OBSs are not directly beneath shot sequence 9. All of the OBSs modeled are within 240 m of shot sequence 9 in the ETOMO study, except for OBS 31, which is ~1 km to the east of the shot line. Because the modeling does not exactly match the experiment layout, travel time differences are created; the observed and predicted arrival times are within a 145 ms window of the synthetic arrivals for a model without an anomalous volume.

Second and Third Best-Observed Amplitude Anomalies, Regions 9 and 8

The second best-observed amplitude anomaly is region 9, located on a ridge on the western flank (**Figure 4.9** – orange arrow) interpreted to be where the ridge axis was

before jumping east to its current location less than 200,000 years ago (Carbotte et al., 2007). I model the overhead shots (shot sequence 20) for the five OBSs that best show the disrupted and low-amplitude *P* wave arrivals (**Figure 4.18**, **4.19**, **4.20**, and **4.21**). The disrupted and attenuated *P* waves I observe in the seismic data (**Figure 4.19**, right column) are very similar to the decreased waveform amplitudes observed for region 16. Based on of these similarities, I test whether the decreases in waveform amplitude are the product of a low-velocity body with increased attenuation in the crust. I use length, depth, and physical properties of the anomalous volume similar to the values used when modeling region 16 (p. 36) to find a model whose resultant waveform and travel time anomalies are similar to the observed arrivals. I create several synthetic models with anomalous volumes and compare these to the observations. Since little change in wave amplitude is noticed when modeling a sill in region 16, I do not generate models with magma sills for region 9.

The best-fit model to match the number of shots with attenuated *P* wave arrivals on the five OBSs is an anomalous volume that is 10 km wide, 2 km thick, and 2 km BSF. These parameters match the length, vertical thickness, and depth of the best-fit anomalous volume identified for region 16. The best-fit model to match the amount of wave amplitude decrease is an anomalous volume with a *Q* value of 40 and a decrease in velocity of ~8% (**Figure 4.21**). To match the ranges of the low-amplitude arrival from the north and south, a length of 10 km best fits the observed arrivals. A *Q* value of 40 with a velocity decrease of 8 percent is the best-fit pair of values for creating a similar loss in wave energy as in the observed arrivals.

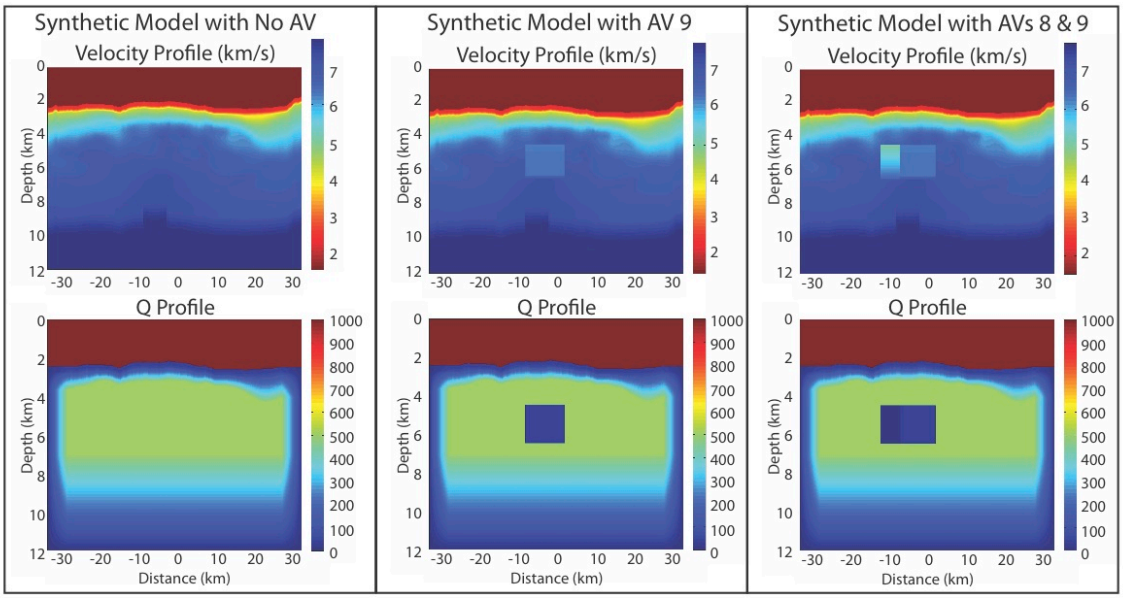

Figure 4.18. Velocity and attenuation profiles for the synthetic models (regions 9 and 8). The left column shows the synthetic model with no anomalous volume; the middle column shows the best-fit synthetic model for region 9, a 10 km wide, 2 km thick, and 2 km BSF volume with a *Q* value of 40 and a decrease in velocity of ~8%; the right column shows the best-fit synthetic model for region 9 along with the best-fit synthetic model for region 8, a 5 km wide, 2 km thick, and 2 km BSF volume with a *Q* value of 8 and a decrease in velocity of ~8%. Region 8 overlays region 9 by 1 km, making the total length of the combined regions 14 km. These velocity and attenuation profiles are used in E3D to create the synthetic records in **Figures 4.19, 4.20, 4.21**.

Figure 4.19 (next page). Regions 8, 9, and 10 identified by *P* waves for profiles crossing directly over the OBSs compared to a synthetic model without an anomalous volume. Seismic records for OBSs 57, 58, 61, 62, and 63 are shown with shot sequence 20 on the vertical channel. The bold, colored lines show the ranges and shot numbers where *P* wave amplitude decreases are detected in the observed arrivals (right column) for region 8 (blue line), region 9 (orange line), and region 10 (pink line). The thinner lines show where the zones of lowered amplitude end. In the synthetic seismic records (left column), no *P* wave amplitude decrease is seen in the regions that are detected in the observed arrivals. The velocity and *Q* values versus depth that are used in the finite difference model are shown in **Figure 4.19**.The locations of the initial amplitude decrease in the observed arrivals are shown by corresponding colored arrows on the bathymetric map in **Figure 4.1**. The record sections are fixed scale, plotted with a velocity reduction of 7.2 km/s, and are band-pass filtered between 5 and 15 Hz.

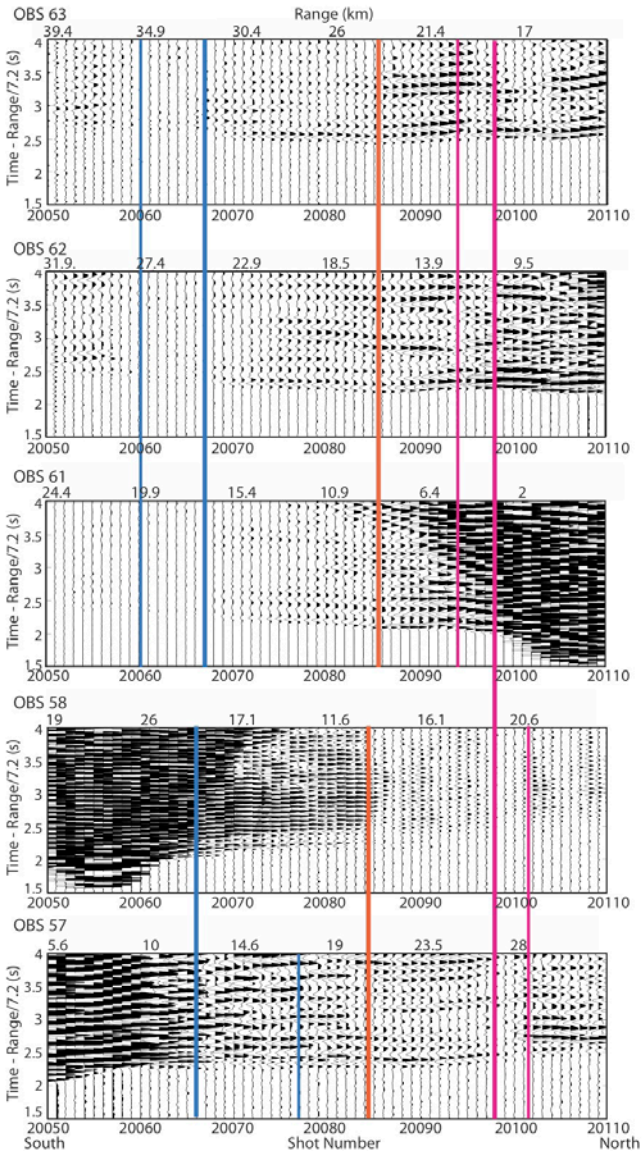
OBS 63
Range (km)
39.4 34.9 30.4 26 21.4 17
OBS 62
31.9 27.4 22.9 18.5 13.9 9.5
OBS 61
24.4 19.9 15.4 10.9 6.4 2
OBS 58
19 26 17.1 11.6 16.1 20.6
OBS 57
5.6 10 14.6 19 23.5 28
Time - Range/7.2 (s)
4 3.5 3 2.5 2 1.5
20050 20060 20070 20080 20090 20100 20110
South
Shot Number
North

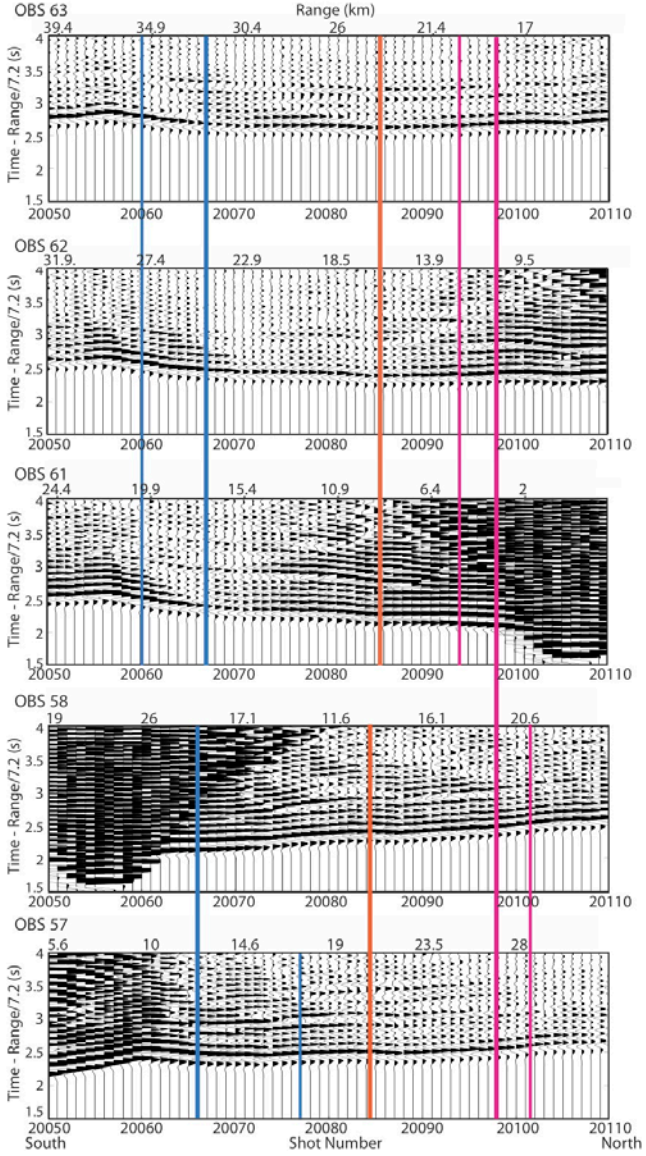
OBS 63
Range (km)
39.4 34.9 30.4 26 21.4 17
OBS 62
31.9 27.4 22.9 18.5 13.9 9.5
OBS 61
24.4 19.9 15.4 10.9 6.4 2
OBS 58
19 26 17.1 11.6 16.1 20.6
OBS 57
5.6 10 14.6 19 23.5 28
Time - Range/7.2 (s)
4 3.5 3 2.5 2 1.5
20050 20060 20070 20080 20090 20100 20110
South
Shot Number
North

The synthetic seismic records for the model without an anomalous volume (**Figure 4.20**) are compared to the model with the best-fit anomalous volume (**Figure 4.21)**. The same scaling is used for both figures. A localized decrease in wave amplitude in the synthetic anomalous volumes model matches the observed (**Figure 4.18**).

The third best-observed amplitude anomaly, region 8, is located on the same western flank ridge as region 9 (**Figure 4.9** – blue arrow). I model region 8 along with region 9 to further show that these anomalous regions are caused by an extended low-velocity, high attenuation volume within the crust. I model the same overhead shots (shot sequence 20) and five OBSs (OBSs 57, 58, 61, 62, and 63) as used for modeling region 9. For region 8, the best-fit model to match the number of shots with attenuated *P* wave arrivals on the five OBSs is an anomalous volume that is 5 km wide, 2 km thick, and 2 km BSF. The best-fit model to match the amount of wave amplitude decrease is an anomalous volume with a *Q* value of 8 and a decrease in velocity of ~8% (**Figure 4.21**). The synthetic seismic records for the model without an anomalous volume (**Figure 4.19**, left column) are compared to the model with the best-fit anomalous volumes for regions 8 and 9 (**Figure 4.21**, left column**)**. The same scaling is used for both figures. A localized decrease in wave amplitude in the synthetic anomalous volume model matches the observations (**Figure 4.21**). The best-fit model suggests that regions 8 and 9 are connected to form one large region (**Figure 4.18**, column 3).

Additional Amplitude Anomalies, Regions 7, 10, and 13-14

To further analyze regions 7, 10, and 13-14, I compare the observed arrivals to synthetic waveform models without an anomalous region. Topography itself will

introduce scattering in 2-D models, since topography acts as an inhomogeneity. Since the 2-D model in E3D is strictly 2-D, it does not account for 3-D scattering (scattering perpendicular to the plane of the model). An example would be that if there is a ridge, the model acts as if the ridge has infinite extent perpendicular to the model (S. Larsen pers. comm.).

Region 7 is located on a western flank of the segment, ~16 km from the ridge axis (**Figure 4.9** – green arrow). I generate a synthetic model without an anomalous region by modeling the overhead shots (shot sequence 2) for the five OBSs (OBSs 15B, 16, 17, and 18) that best show the disrupted and low-amplitude *P* wave arrivals. The velocity and *Q* values versus depth used in the finite difference model are shown in **Figure 4.22**. The observed arrivals (**Figure 4.23**, left column) show a clear decrease in *P* wave amplitude through region 7 that is not seen in the synthetic seismic records without an anomalous volume (**Figure 4.23**, right column).

Figure 4.20 (next page). Synthetic model for the second best-observed amplitude anomaly, region 9, compared to the observed arrivals. For the synthetic seismic records (left column), the orange tinted box on each seismic record shows the length (10 km) and location of the anomalous volume compared to the shot numbers. The amplitude anomaly's location is shown by the orange line on the map in **Figure 4.9**. A similar *P* wave amplitude decrease is seen in the regions that are detected in the observed arrivals for region 9 (right column). For regions 8 and 10, no *P* wave amplitude decrease is seen in the regions that are detected in the observed arrivals. The bold, colored lines show the locations where *P* wave amplitude decreases are detected in the observed arrivals for regions 8, 9, and 10 (right column). The thinner lines show where the zones of lowered amplitude end for the observed arrivals. The velocity and *Q* values versus depth that are used in the finite difference model are shown in **Figure 4.18**.

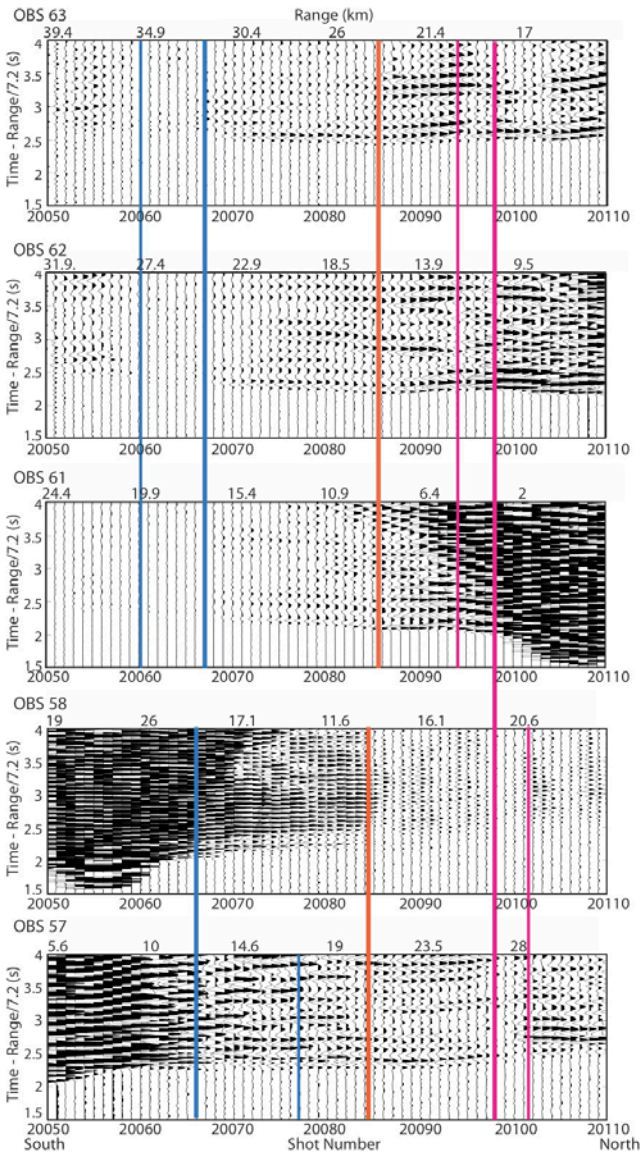
OBS 63
Range (km)
39.4 34.9 30.4 26 21.4 17
OBS 62
31.9. 27.4 22.9 18.5 13.9 9.5
OBS 61
24.4 19.9 15.4 10.9 6.4 2
OBS 58
19 26 17.1 11.6 16.1 20.6
OBS 57
5.6 10 14.6 19 23.5 28
Time - Range/7.2 (s)
1.5 2 2.5 3 3.5 4
20050 20060 20070 20080 20090 20100 20110
South
Shot Number
North

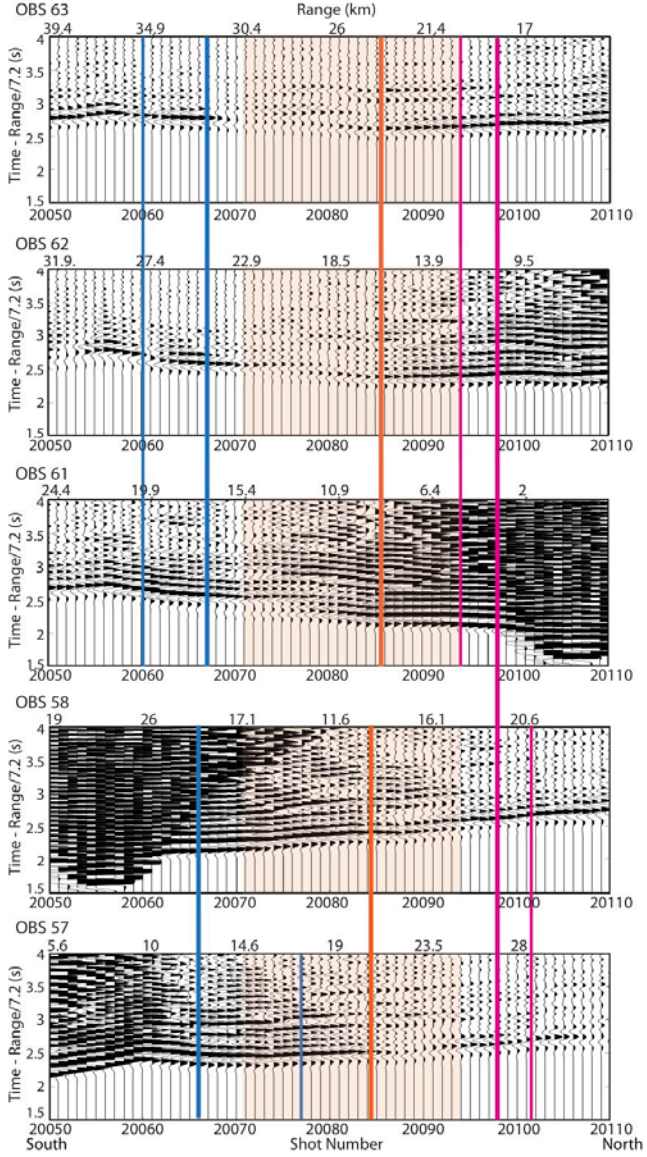
OBS 63
Range (km)
39.4 34.9 30.4 26 21.4 17
OBS 62
31.9. 27.4 22.9 18.5 13.9 9.5
OBS 61
24.4 19.9 15.4 10.9 6.4 2
OBS 58
19 26 17.1 11.6 16.1 20.6
OBS 57
5.6 10 14.6 19 23.5 28
Time - Range/7.2 (s)
1.5 2 2.5 3 3.5 4
20050 20060 20070 20080 20090 20100 20110
South
Shot Number
North

Region 10 is located on the same western flank as regions 8 and 9 (**Figure 4.9** – pink arrow), and region 13-14 is located on the same eastern flank as region 16 (**Figure 4.9** – light green arrow). I compare the synthetic seismic records without an anomalous region (**Figure 4.21**, right column, for region 10 and **Figure 4.12**, right column, for region 13-14) to the observed arrivals (**Appendix C**, **Figure C.9** for region 10 and **Appendix C**, **Figures C.12** and **C.13** for region 13-14). Similarly to region 7, the synthetic seismic records without an anomalous volume do not show a decrease in *P* wave amplitude in the regions that are identified from the observed arrivals for regions 10 and 13-14. Since topography can cause scattering in 2-D models, by comparing the synthetic seismic records for models without an anomalous volume to the observed arrivals, I show that topography is not likely the cause of the anomalous waveform regions. I infer that an anomalous volume with high attenuation in the mid- to lower-crust is needed to decrease the wave amplitude of the first arrivals.

Figure 4.21 (next page). Synthetic model for the regions 8 and 9 (left column) compared to the observed arrivals (right column). The blue tinted box on each seismic record shows the length (5 km) and location of the region 8 compared to the shot numbers. The blue tinted box overlays the orange box representing region 9. The amplitude anomalies' locations are shown by the orange line on the map in **Figure 4.9**. For regions 8 and 9, the *P* wave amplitude decrease is similar to the regions that are detected in the observed**.** For region 10, no *P* wave amplitude decrease is seen in the region that is detected in the observed arrivals. The bold, colored lines show the locations where *P* wave amplitude decreases are detected in the observed arrivals for regions 8, 9, and 10 (right column). The thinner lines show where the zones of lowered amplitude end for the observed arrivals. The velocity and *Q* values versus depth that are used in the finite difference model are shown in **Figure 4.18**.

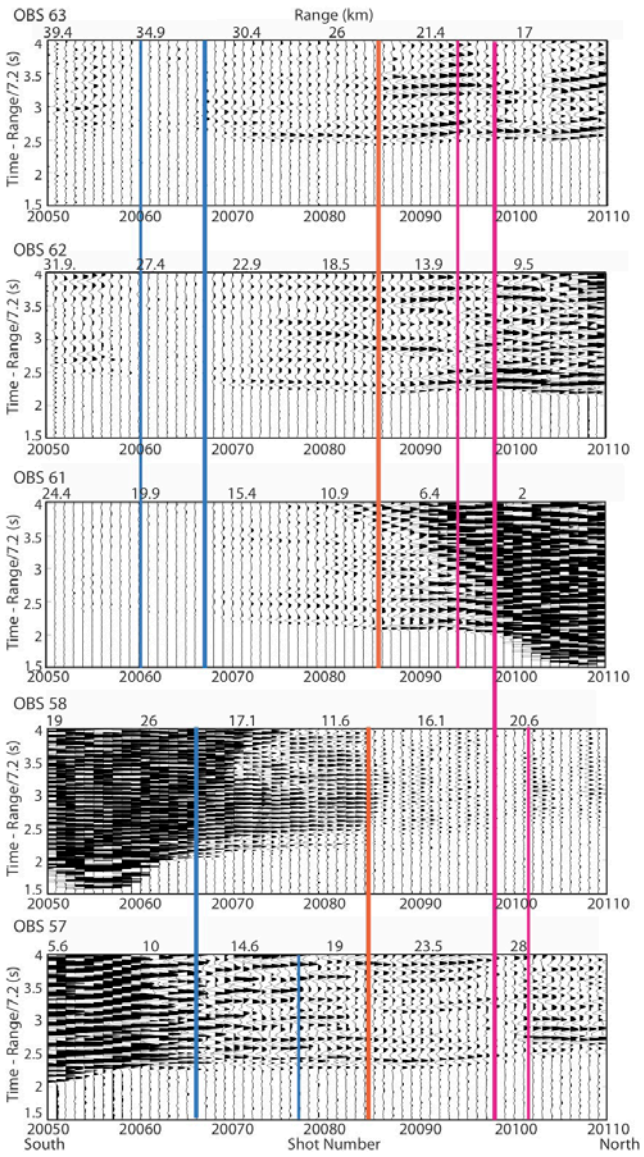
OBS 63
Range (km)
39.4 34.9 30.4 26 21.4 17
OBS 62
31.9 27.4 22.9 18.5 13.9 9.5
OBS 61
24.4 19.9 15.4 10.9 6.4 2
OBS 58
19 26 17.1 11.6 16.1 20.6
OBS 57
5.6 10 14.6 19 23.5 28
Time - Range/7.2 (s)
20050 20060 20070 20080 20090 20100 20110
South
Shot Number
North

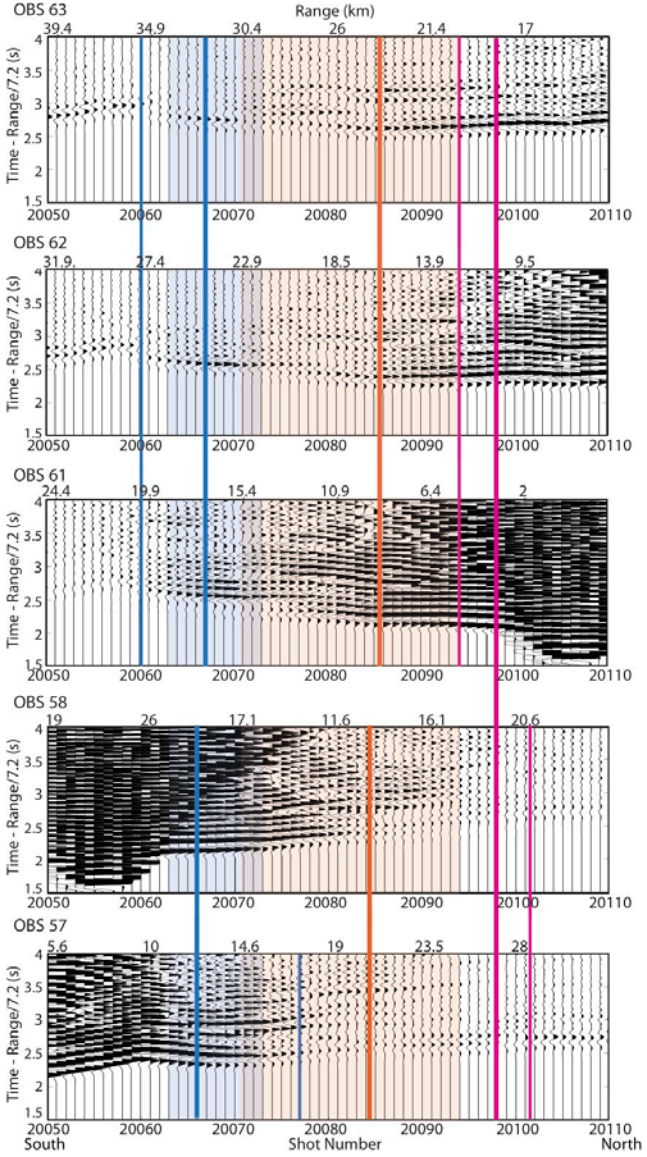
OBS 63
Range (km)
39.4 34.9 30.4 26 21.4 17
OBS 62
31.9 27.4 22.9 18.5 13.9 9.5
OBS 61
24.4 19.9 15.4 10.9 6.4 2
OBS 58
19 26 17.1 11.6 16.1 20.6
OBS 57
5.6 10 14.6 19 23.5 28
Time - Range/7.2 (s)
20050 20060 20070 20080 20090 20100 20110
South
Shot Number
North

Modeling results show that the observed disrupted and attenuated *P* waves help to constrain the dimensions, depths, and physical properties of the anomalous volumes. Model results show the relative dimensions, depths, and physical properties of regions 16, 8, and 9. Comparison of the observed arrivals to synthetic models without an anomalous region indicates that an anomalous body in the mid- to lower-crust may be needed to decrease the wave amplitude of the first arrivals for regions 7, 10, and 13-14. Because the models are 2D, the widths in the direction perpendicular to the ridge axis cannot be determined. The models do not require a sill to be present to create the low-amplitude arrivals. Durant and Toomey (2009) were able to identify a melt sill within the crust by observing large amplitude secondary arrivals on the radial channel of a seismometer. I would need to examine and model the radial channels to determine whether the data require a melt sill to be present.

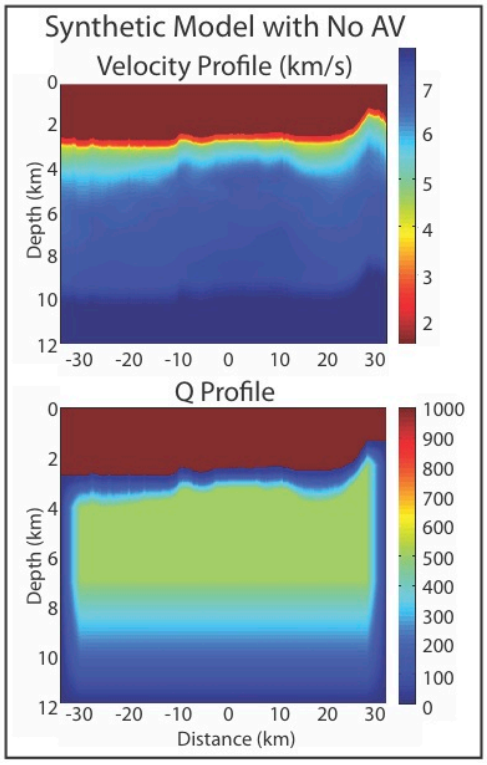

Figure 4.22. Velocity and attenuation profiles for the synthetic model with no anomalous volume for shot sequence 2. These velocity and attenuation profiles are used in E3D to create the synthetic records in **Figure 4.23**. Region 7 is estimated to be located 4 to 6 km on the x-axis and 3.5 to 5.5 km on the y-axis, which is 2 to 4 km BSF. Region 7 is estimated to be located 4 to 6 km on the x-axis and assuming the amplitude anomaly is 2 km thick, 3.5 to 5.5 km on the y-axis, which is 2 to 4 km BSF. Regions 5 and 6 are also located on shot sequence 2. Assuming that both amplitude anomalies are 2 km thick, region 5 is estimated to be located -17 to -10 km on the x-axis and 3.5 to 5.5 km on the y-axis, and region 6 is estimated to be located -8 to -4 km on the x-axis and 2.5 to 4.5 km on the y-axis.

Figure 4.23 (next page). Synthetic model without an anomalous volume (left column) compared to the observed arrivals (right column) for shot sequence 2. Regions 5, 6, and 7 are located beneath shot sequence 2. Their locations are shown in **Figure 4.1** by colored arrows (region 5 – purple, region 6 – blue, and region 7 – green). The bold, colored lines show the locations where *P* wave amplitude decreases are detected in the observed arrivals for the amplitude anomalies. The thinner lines show where the zones of lowered amplitude end for the observed arrivals. For regions 5 and 6, the synthetic seismic records show *P* wave energy loss. For region 5, wave energy loss is shown by a decrease in *P* wave amplitude on the right side of the bold purple line on OBS 15B seismic record. OBS 16 is too close to the region 5 to tell if energy is loss. It is difficult to see the *P* wave energy loss on OBSs 16 and 17 seismic records due to the scaling. For region 6, wave energy loss is shown by a decrease in *P* wave amplitude on the right side of the bold blue line on OBS 15B seismic record. There is a slight decrease in *P* wave energy loss on the left side of the bold blue line on OBSs 16, 17, and 18 seismic records. The *P* wave amplitude decreases are similar to the regions that are detected in the observed arrivals for regions 5 and 6, indicating these regions of wave amplitude decrease are likely caused by topography rather than an anomalous region within the crust. No decrease in *P* wave energy is observed for region 7 for all of the seismic records. The lack of *P* wave energy decrease is not similar to the observed arrivals, indicating an anomalous anomaly within the crust likely causes the observed *P* wave amplitude losses. The velocity and *Q* values versus depth that are used in the finite difference model are shown in **Figure 4.22**.

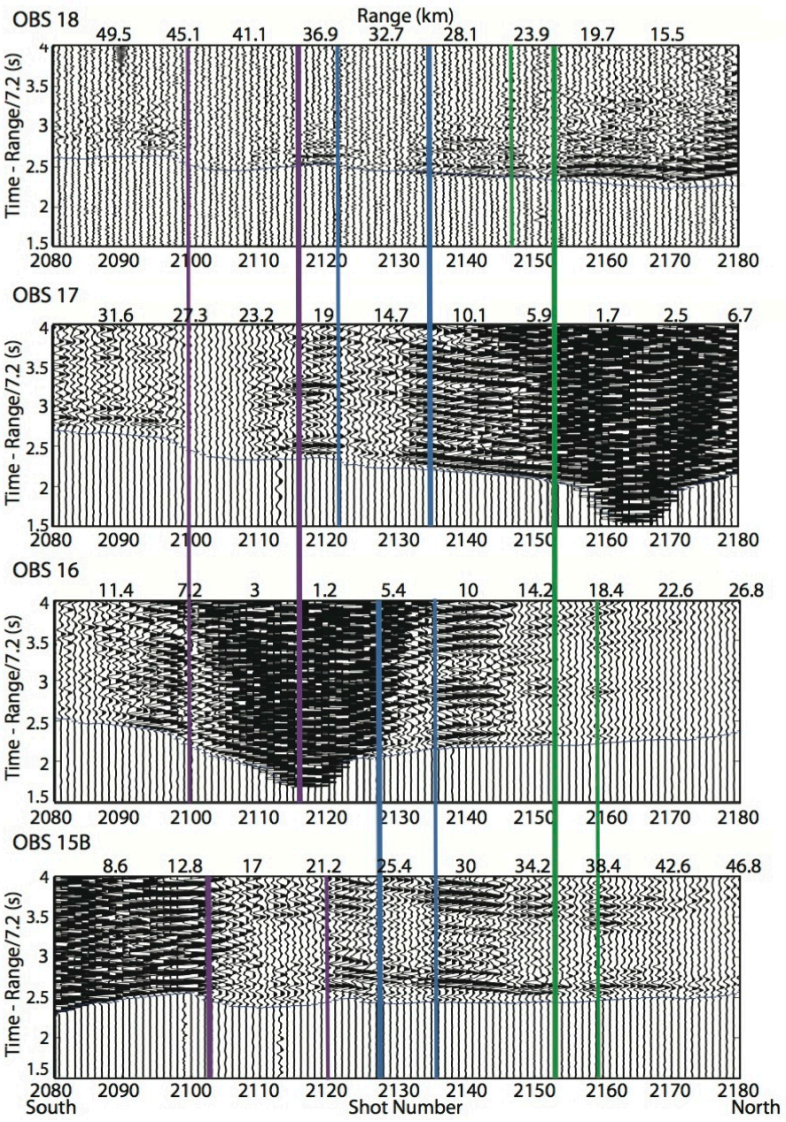
OBS 18
Range (km)
49.5 45.1 41.1 36.9 32.7 28.1 23.9 19.7 15.5
OBS 17
31.6 27.3 23.2 19 14.7 10.1 5.9 1.7 2.5 6.7
OBS 16
11.4 7.2 3 1.2 5.4 10 14.2 18.4 22.6 26.8
OBS 15B
8.6 12.8 17 21.2 25.4 30 34.2 38.4 42.6 46.8
Time - Range/7.2 (s)
4 3.5 3 2.5 2 1.5
2080 2090 2100 2110 2120 2130 2140 2150 2160 2170 2180
South
Shot Number
North

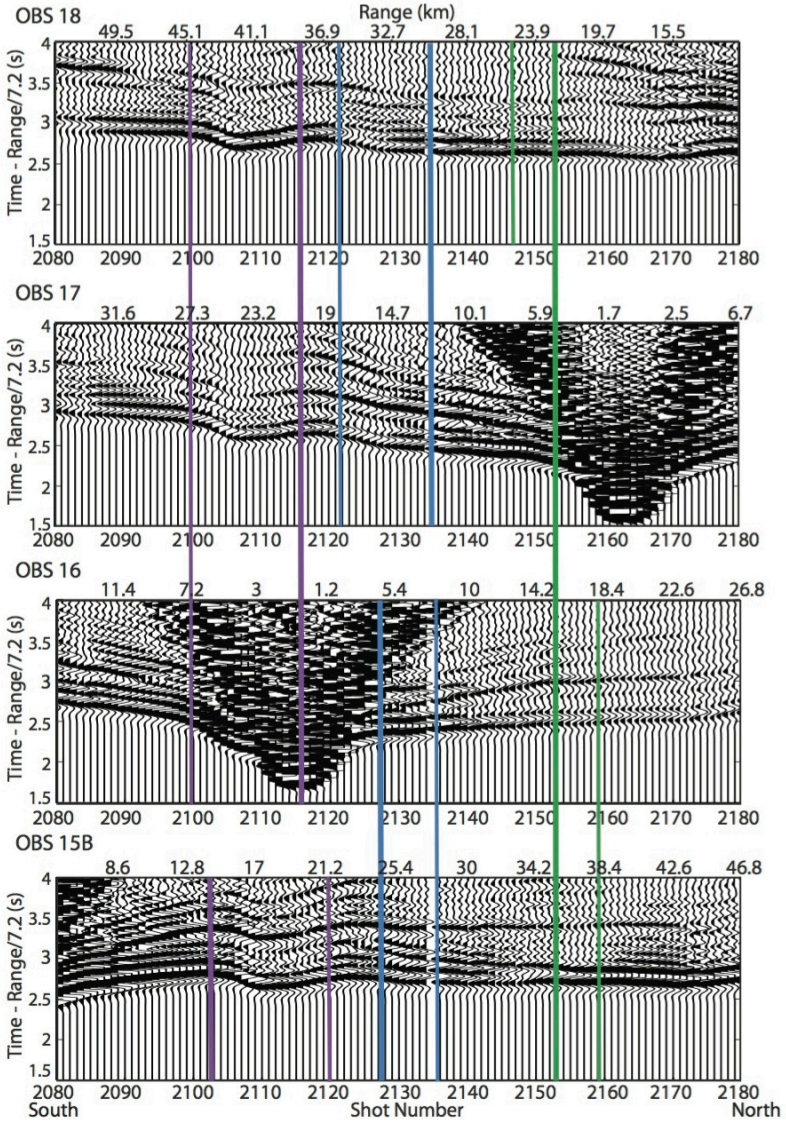
OBS 18
Range (km)
49.5 45.1 41.1 36.9 32.7 28.1 23.9 19.7 15.5
OBS 17
31.6 27.3 23.2 19 14.7 10.1 5.9 1.7 2.5 6.7
OBS 16
11.4 7.2 3 1.2 5.4 10 14.2 18.4 22.6 26.8
OBS 15B
8.6 12.8 17 21.2 25.4 30 34.2 38.4 42.6 46.8
Time - Range/7.2 (s)
4 3.5 3 2.5 2 1.5
2080 2090 2100 2110 2120 2130 2140 2150 2160 2170 2180
South
Shot Number
North

CHAPTER V

DISCUSSION

Section 5.1. Anomalous Volumes

From the seismic observations and modeling, I conclude that regions 8-9 and 16 are velocity and attenuation anomalies located ~7 to 9.5 km west and east of the ridge axis. For region 16, the simplest structure consistent with the data is a large, low-velocity region (10 km long, ~8% decrease in velocity) that is very attenuated. My estimated *Q* value of 10 indicates an increase in attenuation by an order of magnitude from off-axis crustal values. Without evidence for high amplitude P-to-S conversions on radial component seismograms, I cannot determine whether a melt sill is present or not. The anomalous volume causes an average travel time delay of 44 ms, which should be detectable by delay-time tomographic methods; however, since only a few of the arrivals with travel time delays caused by the anomalous volume were included in the inversion to create the 3-D velocity model, the anomalous volume is not detected by delay-time tomographic methods.

Barclay et al. (1998) interpret a low-velocity anomaly at the Mid-Atlantic Ridge as a region of near solidus temperatures with possibly a small degree of partial melt in the crust. Their anomaly has a maximum velocity difference of 0.8 km/s. Barclay et al. (1998) assumes a constant derivative of *P* wave velocity with respect to temperature of -0.5 m/(s K) (Christensen1979; Creager and Jordan, 1986; Humphreys and Duekar, 1994) and attribute ~0.6 km/s of the low-velocity anomaly in the crust to subsolidus temperature variations, given basalt solidus temperatures of ~1150°C (Hess, 1992).

Barclay et al. (1998) interpret the remaining anomaly of 0.2 km/s to show the presence of partial melt. Region 16 has an average maximum velocity difference of 0.5 km/s, which can be attributed to subsolidus temperature variations. For the upper mantle, Hammond and Humphreys (2000) find a velocity reduction of 8% would mean approximately 1% partial melt. For region 16, a velocity decrease of 8% implies the volume's temperature is increased to the solidus and that there is no partial melt; however, due to the tradeoff between velocity reduction and attenuation when modeling the anomalous volume, there may be more velocity reduction and less attenuation, which could imply the presence of partial melt within the region. Because I cannot determine the exact amount of velocity reduction or attenuation, I cannot resolve if there is partial melt within the anomalous volume. I interpret region 16 to have been created from previous or current magmatic activity at this ridge on the east flank, which could possibly contain a very small percent of partial melt.

Region 8-9 is very similar to region 16 in that it is an extended, low-velocity region (10 km long, ~8% decrease in velocity) that is very attenuated, *Q* values of 8 to 40. Region 8-9 is located parallel to region 16 and the spreading axis. The extended region can be seen in the velocity profile for the synthetic model with regions 8 & 9 in **Figure 4.19** and is located on the western flank, 7 km from the ridge axis. Based on these results and the location of region 10 close to region 9 (~1.5 km apart), I infer that region 10 is likely connected to this extended region as well. I interpret these regions to be a large region, created from previous or current magmatic activity at this ridge on the west flank. Similar to region 16, I cannot resolve if there is partial melt within the anomalous volume. **Figure 5.1** shows an interpretation of regions 8-9 and 16 in relation to the ridge axis.

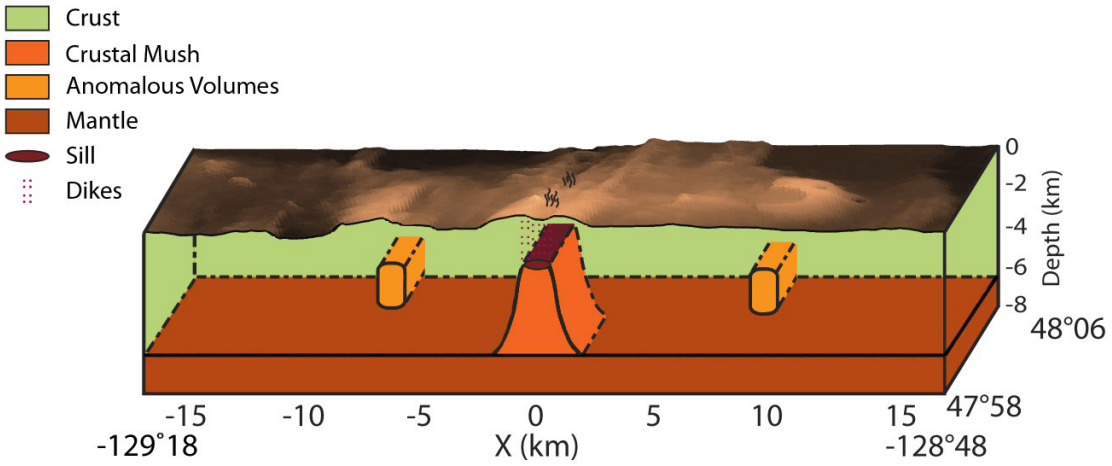

Figure 5.1. Cartoon of regions 8-9 and 16 in relation to the ridge axis. Top surface shows the bathymetry from the segment center to the north, 129°18' W to -128°48' W and 47°248' N to 48°06' N. The anomalous volumes are interpreted as regions of previous or current magmatic activity (light orange) beneath bathymetric ridges that parallel the neovolcanic axis. There may be sills (red) present within the regions, but that cannot be determined from this study.

I infer that regions 7 and 13-14 are similar to regions 8, 9, and 16, indicating that there are multiple seismic velocity and attenuation anomalies on the eastern and western flanks 7 to 16 km from the neovolcanic zone, located 2 to 3 km beneath bathymetric highs at the Endeavour segment of the Juan de Fuca Ridge. Without finite difference modeling, I cannot determine if these regions contain partial melt. From the seismic observations, ray tracing and finite difference modeling, I cannot determine if any of the six identified regions contain melt sills or dikes.

I did not model the exact dimensions, depths, and physical properties of regions 7, 10, and 13-14; however, I estimate the lengths and maximum feasible depths from the seismic observations (**Appendix B**, **Table B.5**). On the eastern flank, region 13-14 is

located approximately 9 km from the axis, ~4 to ~7 km in along-axis extent, beneath the off-axis ridge, parallel to region 16, and 11 km south of it. On the western flank, region 10 is 7 km from the ridge axis, around 2 km in along-axis extent. The amplitude anomaly, region 7, is ~16 km west of the axis, around 2.4 km in extent. The amplitude anomaly locations are shown in **Figure 4.9**. It is very probable that there are more velocity and attenuation anomalies that are not detected due to their locations not being beneath shot lines that are examined in the analysis. Since the anomalous volumes identified are beneath ridges, I infer that there are likely more anomalous regions beneath ridges where there were no shot lines in this study.

Reflection Study

Suzanne Carbotte identified several off-axis, crustal-level reflectors in her reflection survey, EW02-07. A seismic reflection occurs when a wave intercepts an interface separating media of different impendences; part of the wave's energy is reflected back towards the surface, which can be detected in the processed MCS data. The multichannel seismic survey (MCS) included 30-to 40-km-long lines perpendicular to the ridge spaced 3-10 km apart and also lines parallel to the ridge on ridge flanks, 7.5 and 15 km from the spreading axis. Two of the 11 cross-axis lines extend to 40 km on the east flank. The reflection study utilized a 6-km long, 480-channel streamer and a 10-element, 3005 in^3 airgun array, fired every 37.5 m (Carbotte et al., 2002).

One of the crustal-level reflectors (blue circle in **Figure 5.2**; S. M. Carbotte pers. comm.) is coincident with region 6 (blue arrow in **Figure 4.1**), is located at an approximate depth of 3.2 km, and has normal polarity. Region 6 is identified in the

overhead and crosscutting *P* wave analysis but is not included with the identified anomalous regions due to the presence of topography at its location (**Figure 4.23**). The yellow-circled reflector in **Figure 5.2** has reversed polarity to the seafloor and is at an approximate depth of 3.5 km. Due to its location ~3.6 km from the closest shot sequence, 2, this area was not examined in my study. The reflectors' depths were calculated using a two way travel time of 1.4 and 1.5 s, a layer 2A thickness of 0.5 km with a velocity of 2.63 km/s, and a layer 2B with a velocity of 5.53 km/s (Van Ark et al., 2007).

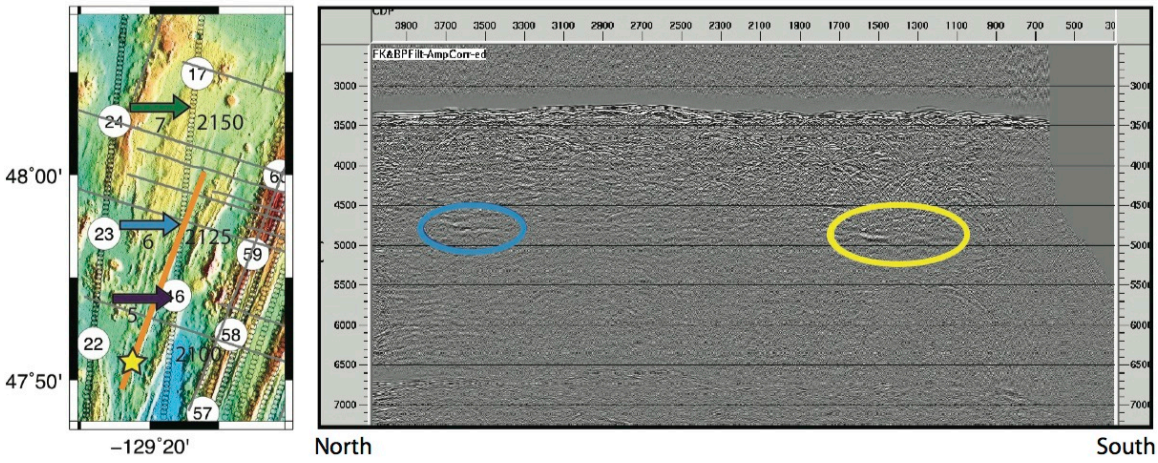

Figure 5.2. ETOMO map and reflection image for line 16 of the EW0207 reflection survey courtesy of Suzanne Carbotte. On the bathymetric map, EW0207 reflection survey lines are shown in gray with Line 16 highlighted in orange. The reflector circled in blue spans from CDP ~3300 to ~3800 and is in the same location as region 6 (blue arrow). The purple arrow shows the location of region 5, and the green arrow shows the location of region 7. The reflector circled in yellow spans CDP ~1100 to ~1800 and has reversed polarity. Its location is shown by the star on the map.

These crustal-level reflectors may be indicative of a magma body. One of the identified crustal-level reflectors showed a reversal in polarity (yellow circle in **Figure 5.2**). This change in the polarity is typically due to a decrease in seismic velocity as the near-vertical reflection travels from solid rock to pure melt or partially molten magma

(Van Ark et al., 2007). The change in polarity could also be due to waves intercepting part of the hydrothermal system. These crustal-level reflectors may possibly indicate the locations of crustal-level magma sills, further supporting the presence of off-axis volcanism at the Endeavour segment.

Section 5.2. Origins of the Anomalous Volumes

The observation of off-axis, crustal-level, anomalous regions at both the East Pacific Rise and the Endeavour segment show that off-axis volcanism is likely a common feature at mid-ocean ridges; however, the question remains of what process or processes contribute to its occurrence. There are multiple processes that could account for the crustal-level, anomalous regions away from the ridge axis. The four main processes at the Endeavour segment are (1) distributed magmatism related to the Juan de Fuca Ridge overriding the Heckle hotspot, (2) the Endeavour and Cobb OSCs propagating and cutting into the Endeavour segment, (3) Sovanco Fracture Zone and fault orientation, or (4) weak focusing of mantle melt delivery resulting in magmatic intrusion beneath the off-axis bathymetric highs at the Endeavour segment. These four topics are discussed separately, although they may be related.

Heckle Hotspot

All of the identified anomalous volumes are located within the ~40 km wide plateau of inferred thicker crust that is associated with the interpreted Heckle hotspot. Part of region 16 lies beneath the caldera northwest of the ridge axis (**Figure 5.3** – large, black circle). Region 16 extends ~8 km south of the caldera, beneath a topographic high that parallels the ridge axis, and is interpreted to be a large region created from previous

or current magmatic activity. It is possible the anomalous region is connected or related to the formation of the caldera. The caldera likely formed during a large volume eruption. The magma for the eruption may have been delivered through the attenuating region I observe to the south. After the volcanic activity ended, the region beneath cooled. For magmatic intrusions in a region 2 km in vertical length, the timescale for the region to solidify would be from ~4000 to 30,000 years depending upon interaction with hydrothermal circulation (calculations are shown in **Appendix E**). From this study, I cannot determine the exact age of the caldera's formation. If the region does contain partial melt, the caldera would have formed less than 30,000 years ago, and if the region contains no partial melt, the caldera likely formed more than ~4,000 years ago.

The bathymetry follows the same pattern that *Hammond 1997* found for seamount chains in that the collapsed side of the caldera is on the opposite side of the seafloor spreading direction (**Figure 5.3**). Another area of greater elevation (small circle in **Figure 5.3**) may have been created from the same melt supply that created the caldera. Both the caldera and the smaller elevated region are on elevated ridgelines parallel to the ridge axis, indicating the magma supply may have followed older conduits created by dike injections when the areas were in the neovolcanic zone.

The caldera is much smaller than the Heckle seamounts and larger than the smaller elevated region (small circle in **Figure 5.3**), which is closer to the ridge axis, consistent with evidence that the Heckle hotspot may be waning. The ridge axis is interpreted to currently be over the waning Heckle hotspot (Carbotte et al., 2007). If the spreading center did jump to its current location over the hotspot, the size of the caldera compared to the Heckle seamounts may not support the idea that the hotspot is waning

since the hotspot's melt is being focused primarily towards the ridge axis. Since region 16 is not located exactly beneath the caldera, the magma that formed the caldera may not have interacted with the region. Region 13-14 is beneath the same off-axis ridge as region 16, indicating region 13-14 may be associated with or have formed at the same time as region 16.

Figure 5.3 (next page). Region 16 in relation to the caldera. (a) Zoomed in map of the Endeavour segment. Region 16's location is shown by the redline. Region 16 is part way under the caldera (large black circle). Black arrows show spreading directions, 30 mm/yr half-spreading rate. Red arrow shows the direction the Juan de Fuca Ridge is moving in a hotspot reference frame, ~31 mm/yr (Carbotte, 2007). Purple arrow shows the absolute spreading direction for the Juan de Fuca Plate side of the Endeavour segment in a hotspot reference frame, ~21.6 mm/yr, and the blue arrow shows the absolute spreading direction for the Pacific Plate side of the Endeavour segment in a hotspot reference frame, ~52.5 mm/yr, calculated from the HS3-Nuvel1a plate motion model (Gripp and Gordon, 2002). (b) Model of the formation of flank volcanoes on the Juan de Fuca Ridge taken from Hammond (1997) Fig. 5A-D. Pulses of magma delivered from a stationary source create the volcanoes. Over time, there are periods of magma supply and withdrawal forming craters and calderas. As the volcano is moved away from the magma source, the volcano becomes extinct and summit collapse predominates over constructive activity. The collapse structure has been found to be located on the volcano's side overylying the most recent active conduit. A new magma pulse ruptures through the younger crust overlying the magma source. The red arrows show the magma source in the mantle. The smaller black arrows show either rising magma (up arrows) or declining magma supply (down arrows) (Hammond, 1997). The caldera in (a) has a similar structure to Hammond (1997)'s model for volcanic chains. The caldera lies to the east of the ridge axis, coinsiding with the absolute motion direction for the Juan de Fuca plate (purple arrow). The smaller circle shows another area of higher topography that may have been created by the same source of magma supply that created the larger caldera.

a)

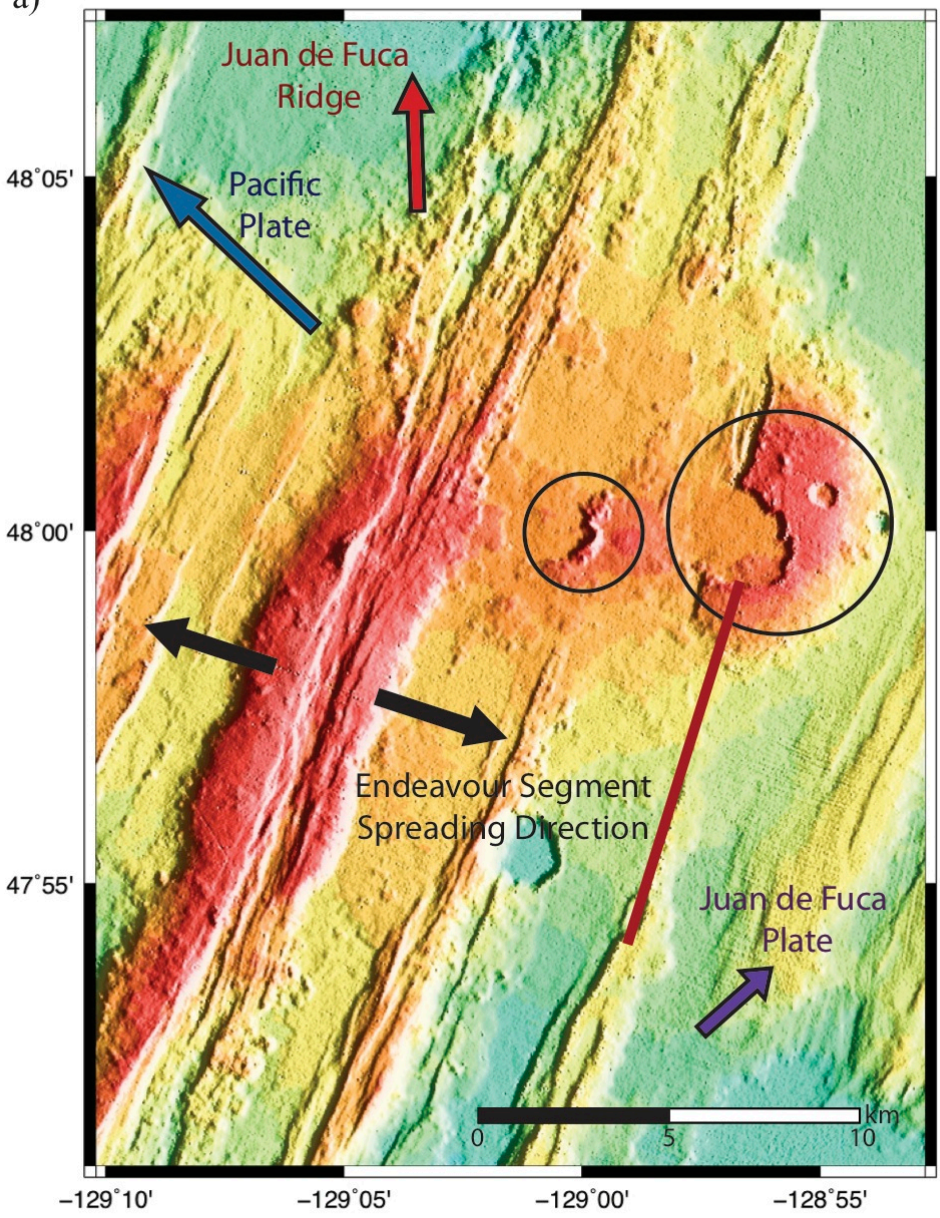
Juan de Fuca
Ridge
Pacific
Plate
48˚05'
48˚00'
47˚55'
Endeavour Segment
Spreading Direction
Juan de Fuca
Plate
0
5
10
km
−129˚10'
−129˚05'
−129˚00'
−128˚55'

b)

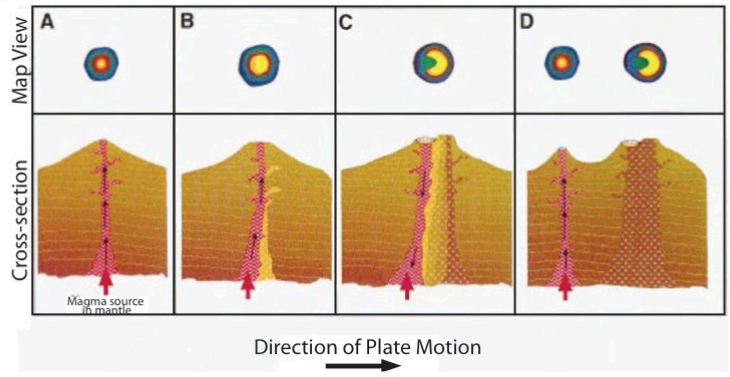
A
B
C
D
Map View
Cross-section
Magma source
in mantle
Direction of Plate Motion

Geochemical sampling of the Heckle seamounts imply the lavas came from a highly depleted mantle source, whereas samples from the ridge axis are enriched in incompatible elements (Leybourne and Van Wagoner, 1991; Karsten, 1988). The Vance seamounts and Vance segment (southern Juan de Fuca Ridge) have similar compositional differences between the depleted seamounts and enriched mid-ocean ridge basalts (MORB) ridge axis lavas (Wendt et al., 2007). The depleted seamounts would necessitate a depleted mantle source with a shallow thermal anomaly rather than an enriched compositional heterogeneity (Leybourne and Van Wagoner, 1991), which may or may not be stationary in the hotspot reference frame. At the Endeavour segment, MORBs have not been tested to see if there is a compositional difference between the on-axis and off-axis basalts. Compositional testing and age dating of the caldera and off-axis ridge would better help to determine their sources and time of formation.

Evidence at crustal ages <200,000 years indicate a small eastward jump of the spreading axis (**Figure 1.2** – black star), suggesting the spreading center jumped east onto the Heckle hotspot (Carbotte et al., 2007). Regions 8-9 and 10 are beneath the ridge on the west flank interpreted to have been the previous spreading center before it jumped east to its current location These regions are seen very clearly in the seismic data and are parallel to the locations of the segmented crustal magma lenses under the main rise axis (Van Ark et al., 2007). If the spreading center recently jumped from this ridge to its current location, these anomalous volumes may be regions remaining from when the spreading center was located over this ridge. If the spreading center did jump to the east, that would explain the large region (>14km) of anomalous volumes on the western side of the current ridge axis. I cannot determine the exact time the spreading center jumped to

its current location. If the region does contain partial melt, the spreading center would have jumped to its current location less than 30,000 years ago, and if the region contains no partial melt, the spreading center would have jumped to its current location more than ~4,000 years ago (calculations are shown in **Appendix E**).

Region 7 is located near an off-axis ridge further west than regions 8-9 and 10. Region 7 may be an anomalous region showing the track of plate movement over the Heckle hotspot. Region 7 appears to be smaller in size compared to the other anomalous volumes. Its smaller size may be due to its distance from the hotspot and/or the ridge axis. The greater distance indicates the more time it has had to cool.

Interactions with Overlapping Spreading Centers

Both the segments north and south of Endeavour, Middle/West Valley and Northern Symmetric respectively, are interpreted to be propagating into the Endeavour segment (Carbotte et al., 2008; Van Wagoner and Leybour, 1991). Interactions with these propagating segments may play a part in the presence of the anomalous volumes. Region 13-14 is located in front of the propagating tip of Northern Symmetric. Region 13-14 may have had previous magmatic activity and is now being heated by the propagating tip. The other identified anomalous volumes are at greater distances (>10 km) to the propagating tips. There is a great amount of earthquake activity in the center of the Endeavour segment and in the Endeavour and the Cobb OSCs (Hooft et al., 2010). The OSCs may be creating additional stresses that weaken the crust to an extent great enough to allow weak focusing of mantle melt deliver.

Sovanco Fracture Zone and Fault Orientation

Dziak (2006) interprets the Sovanco Fracture Zone to include the Heckle seamounts and potentially extend as far south as the Cobb offset. Dziak (2006) argues that bathymetric data shows evidence of right-lateral strike slip deformation at the Heckle seamounts and that the seamounts may have formed due to volcanic activity from an upper mantle melt, which used preexisting strike-slip faults as a conduit for magma. It is possible that the off-axis volcanism found at the Endeavour segment is due to fractures created from the Sovanco Fracture Zone, fractures parallel to the Sovanco fracture zone and oblique (~65**°)** to the Endeavour segment, and also from Endeavour's fault orientation, which is parallel to the ridge axis (Dziak, 2006). The fractures and faults could provide easy conduits for magma to travel from the upper mantle. If the Sovanco Fracture Zone and fault orientation around the ridge account for the presence of the anomalous volumes, that suggests that melt is present in the mantle over a large region, at least16 x 18 km, at the Endeavour segment.

Weak Focusing of Mantle Melt Delivery

Weak focusing of mantle melt delivery could explain the presence of the off-axis anomalous volumes. The off-axis, crustal-level, anomalous regions at the East Pacific Rise support the idea that mantle melt delivery may not be completely focused towards the neovolcanic zone. The anomalous volumes could be regions left from off-axis intrusive activity or show locations of current magmatic intrusions. All of the anomalous volumes are located beneath bathymetric highs parallel to the spreading axis and are also within the plateau of interpreted thicker crust (**Figure 5.1**). Weak focusing of melt could

account for the plateau at the center of the Endeavour segment, or more accretion at the ridge axis when the crust formed. The seismic evidence of multiple anomalous regions, shown in **Figure 4.9**, located off-axis support the idea of weak focusing of melt. Region 7 appears to be smaller in size compared to the other regions and is also furthest from the spreading axis. If poor focusing of melt created the anomalous volumes, this could show that the greater the distance from the spreading axis, the smaller the melt supply.

From this study, I cannot determine the exact process or processes that created these off-axis anomalous regions. I infer from the cooling times that these regions were created off axis and are not a remnant of on-axis volcanism. I find several areas on the plateau of interpreted thicker crust, which supports the Heckle hotspot theory. In addition to the Heckle hotspot, the tectonic geometry might create lines of weakness that allow off-axis volcanism. One question is whether off-axis volcanism is dependent on mechanisms other than heating by melt from below to create melt pathways.

CHAPTER VI

CONCLUSION

Using seismic data from the Endeavour segment of the Juan de Fuca Ridge, I identify several crustal-level, low-velocity, high-attenuation regions on the eastern and western ridge flanks 7 to 16 km from the neovolcanic zone. I constrain the geometry and physical properties of these regions with finite difference waveform modeling. The anomalous regions extend 10-15 km beneath axis-parallel bathymetric highs and from 2 to 4 km below the seafloor. With a relatively small velocity reduction (~8%) and large attenuation (*Q* values of 8 to 40), I infer the regions to have formed from previous or current volcanic activity. Due to the tradeoff between velocity reduction and attenuation when modeling the regions, I cannot determine whether the regions contain partial melt. It is very likely that there are more velocity and attenuation anomalies that are not detected from this study. From the pattern of the anomalous volumes being located beneath ridges, I surmise that there are likely more anomalous regions beneath ridges where there were no shot lines.

The presence of anomalous magmatic activity 7 to 16 km from the neovolcanic zone conflicts with the generally held view that oceanic crust forms primarily within a 1–2 km of the spreading ridge axis. These magmatic regions at the Endeavour segment and East Pacific Rise show that off-axis volcanism is likely a general feature at mid-ocean ridges. The exact processes that contribute to their formation cannot be determined from this study. More detailed seismic imaging of the lower crust and compositional testing of

off-axis MORB are needed to resolve the exact causes of these off-axis, low-velocity regions.

From the current movements of the ridge and the OSCs propagating and cutting into Endeavour from both the north and south, I interpret that the Heckle hotspot and tectonic geometries created crustal-level, off-axis anomalous regions, which have cooled within the crust, potentially leaving a small percent of partial melt. The location of the large anomalous region beneath the ridge on the west side of the spreading axis supports the concept of the spreading center jumping from the western ridge to its current location. I infer that the large caldera likely formed a large volume eruption due to the Heckle hotspot. The magmatic volume may have traveled through the attenuating region.

The OSCs from the north and south have been propagating and cutting into the Endeavour segment. These OSCs may additionally be weakening the crust, allowing diffuse flow of melt. It is possible that the off-axis volcanism found at the Endeavour segment is due to fractures created from the Sovanco Fracture Zone, fractures parallel to the Sovanco fracture zone and oblique (~65**°)** to the Endeavour segment, and also from Endeavour's fault orientation, which is parallel to the ridge axis (Dziak, 2006). The Sovanco Fracture Zone is interpreted to extend into the Endeavour segment, creating fractures parallel to the Sovanco fracture zone and oblique (~65**°)** to the segment, and the Endeavour segment has a fault orientation parallel to the ridge axis (Dziak, 2006). Fractures from the Sovanco Fracture Zone and the segment's fault orientation may provide easy conduits for melt to flow from the mantle. From this study, I cannot determine if the Heckle hotspot or Sovanco Fracture Zone or a combination of the two created the Heckle seamount chain. If the OSCs are propagating into the Endeavour

segment, I am unable to determine the extent of which they might weaken the crust to allow off-axis volcanism. Therefore, I cannot determine the exact process or processes that account for the off-axis volcanism.

The tectonic settings may have enhanced, if not caused, the diffuse focusing of melt delivery. Due to Endeavour's complex tectonic history, it cannot be assumed that weak focusing of melt is common for spreading centers. More comprehensive observations of off-axis areas at other spreading centers would help to determine which processes influence their formation. My results present further evidence of off-axis magmatic activity, adding to our overall understanding of mid-ocean spreading centers.

APPENDIX A

WAVEFORM MODEL PARAMETERIZATIONS

To forward model region 16, I use two models. One consists of a 1701 x 301 nodal grid with a 40 m nodal spacing and the other consists of a 6801 x 1201 nodal grid with a 10 m nodal spacing in both vertical and horizontal directions. To forward model regions 9 and 8, I use a model consisting of a 1626 x 301 nodal grid with a 40 m nodal spacing in both vertical and horizontal directions. I use one model to examine region 7, consisting of a 2101 x 301 nodal grid with a 40 m nodal spacing in both vertical and horizontal directions. The locations of the models are shown in **Figure A.1** by the colored lines, red – region 16, blue – regions 9 and 8, and purple – region 7. The OBSs modeled are shown by corresponding, bold colored circles on each shot line.

Table A.1 shows the *Vp*/*Vs* ratios, *Q* values, and *Qp*/*Qs* ratios taken from Durant and Toomey (2009) that I use in the finite difference models.

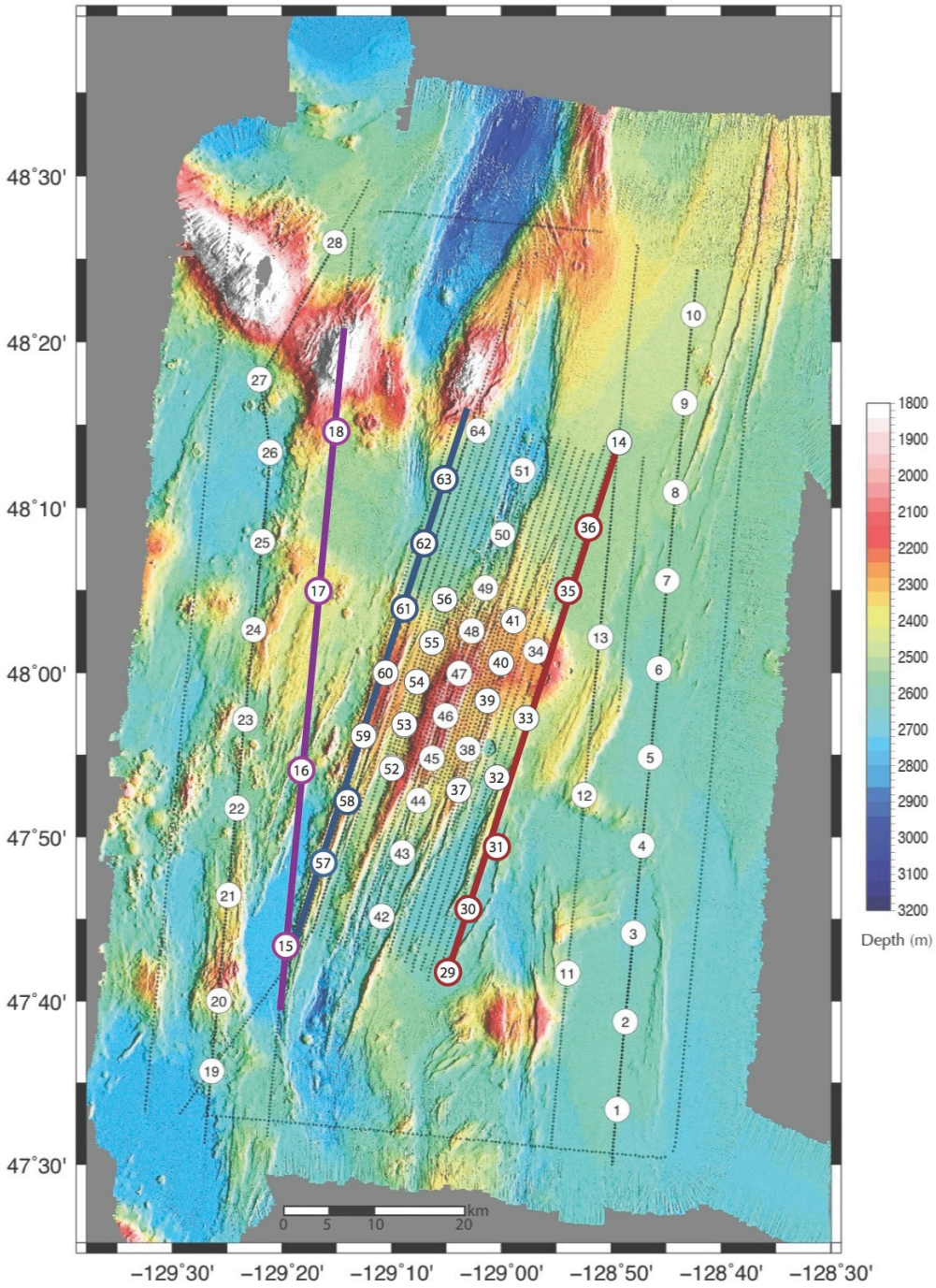

Figure A.1. Bathymetric map of Endeavour segment with colored lines showing the sequence shot lines used in the finite difference model (Sequence 9 – red, sequence 20 – blue, sequence 2 – purple). The OBSs modeled are shown by corresponding, bold colored circles on each shot line. ETOMO shot locations are shown by small black circles, and the OBS locations are shown by the larger white circles with each OBS's number in the middle. The scale shows the surface depth.

Layer	*Vp/Vs* ratio	*Q* value	*Qp/Qs* ratio
2A	1.9	35-50	2.25
2B	1.85	50-500	2.25
2C	1.85	500	2.25
3	1.8	500	2.25
Mantle	1.8	500	2.25

Table A.1. *Vp*/*Vs* ratios, *Q* values, and *Qp*/*Qs* ratios used for finite difference modeling. Values are taken from Durant and Toomey (2009). The *Q* values for layers 2A and 2B are gradients of 35 to 50 and 50 to 500, respectively.

APPENDIX B

OBSERVATIONS OF IDENTIFIED AMPLITUDE ANOMALIES

Observations for each amplitude anomaly from the overhead and crosscutting *P* waves from the figures in **Appendices C** and **D** are listed in **Tables B.1** through **B.5**. The amplitude anomalies' map locations are shown in **Figure 4.1** and **4.9**. The OBSs and shot sequence numbers that are examined for each amplitude anomaly are listed along with the initial shot where wave amplitude is lost and the last shot where amplitude increases again. From these numbers, the total size of the region is estimated. Using ray tracing, the shallowest depth of the top of each of the seven identified amplitude anomalies is estimated. The observations are ranked in quality from highest to lowest (3 - clear drop in amplitude with a loss of amplitude in the following shots; 2 - clear drop in amplitude without a loss of amplitude in the following shots; 1 - not as clear a drop in amplitude; 0 - no observed drop in amplitude). The overhead *P* wave observations are listed in **Tables B.1** and **B.2**. The crosscutting *P* wave observations are listed in **Tables B.3** and **B.4**. All the amplitude anomalies are ranked by their overall quality in **Table B.5**. The seven identified amplitude anomalies are placed in three tier groups by their quality ranking. Regions 8, 9, and 16 are the best-observed anomalous regions.

Region	OBS #	Seq. #	1st Shot #	Last Shot #	Range Start (km)	Range End (km)	Total Size (km)	Quality (1-low 3-high)	Estimated Max Depth of AV (km)	Notes
1	19	42	42074	42078	17.5	18.5	1	2		Decrease in amplitude can clear be seen on both sides of the OBS. Small region.
	22	42	42071	42075	12	13.7	1.7	1		
	24	42	42071	42075	31	33.7	2.7	1		
	25	42	42071	42074	42	43	1	1		
2	21	42	42142	42150	25.6	29.5	3.9	1		Clear drop in amplitude on both sides
	22	42	42142	42150	15.6	19.5	3.9	1		
	25	42	42135	42143	14	16.5	2.5	2		
	26	42	42135	42143	24.2	26.7	2.5	2		
3	23	42	42170		18			2		Amplitude never returns
	26	42	42167	42171	12	13.5	1.5	2		
	27	42	42171		20			1		Amplitude never returns
4	24	42	42179		12			3		Amplitude never returns
	26	42	42180		8			2		
	27	42	42180		16			3		
5	15B	2	2117	2121	20	21.5	1.5	2		Small Region
	17	2	2117		19.5			2		Amplitude never returns. Possibly caused by topography.
	18	2	2118		38			3		
6	15B	2	2127	2135	24	29	5	2	0.8	Very clear drop in amplitude on both sides. Large region. The anomalous region seems to be deeper.
	16	2	2127	2135	4.2	8	3.8	2		
	17	2	2122	2132	13.9	18	4.1	2		
	18	2	2122	2131	31.8	36	4.2	2		
7	15B	2	2153	2159	35.2	37.5	2.3	2	2.4	Clear drop in amplitude on both sides.
	16	2	2153	2159	15.2	17.5	2.3	2		
	18	2	2154	2158	22	24.5	2.5	2		
8	15B	20	2066	20077	22.5	27	4.5	3	2.2	Clear drop in amplitude on both sides.
	57	20	20066	20077	13	17.5	4.5	3		
	60	20	20058	20066	9.5	13.8	4.3	3		
	61	20	20058	20068	16.7	21.3	4.6	3		
	62	20	20058	20068	24.3	28.8	4.5	3		
	63	20	20058	20068	31	36.3	5.3	3		
9	57	20	20085		21			1	2.2	Amplitude never returns.
	58	20	20085		13			3		
	61	20	20085		9			3		
	62	20	20085		16			1		
	63	20	20085		24			1		
10	57	20	20098	20102	26.5	28	1.5	2	2.2	Small Region. Clear drop in amplitude, but not very large.
	58	20	20095	20102	19	20.5	1.5	1		
	59	20	20096	20102	11	13	2	2		
	62	20	20093	20098	11	13	2	2		
	63	20	20093	20098	18.5	20	1.5	2		

Table B.1. Overhead *P* wave observations for regions 1 – 10.

Region	OBS #	Seq. #	1st Shot #	Last Shot #	Range Start (km)	Range End (km)	Total Size (km)	Quality (1-low 3-high)	Estimated Max Depth of AV (km)	Notes
11	57	20	20119	20125	35.6	38.5	2.9	2		Clearly seen from the southern side but not as well from the north.
	59	20	20119	20125	20.7	23	2.3	2		
	60	20	20119	20125	13.2	16	2.8	3		
	63	20	20120		8			3		Amplitude never returns.
12	30	9	9028	9021	4	7.9	3.9	1		Shots do not cover wide enough of a region to examine. Only see on one side.
	32	9	9028	9021	19	22.9	3.9	2		
	33	9	9028	9022	27	30	3	2		
	34	9	9028	9023	34	37.5	3.5	1		
13	29	9	9045		12			2	2.4	Amplitude never returns.
	32	9	9032	9045	17	25.8	8.8	2		Large region. Not as clear as others.
	33	9	9033	9045	25	32	7	1		
	34	9	9033	9045	33	37	4	1		
14	29	9	9053		14			3	2	Amplitude never returns on either side. Anomaly looks clear on both sides, but does not seem very deep.
	32	9	9054		8			3		
	33	9	9054		16			2		
	34	9	9054		23.5			1		
15	30	9	9067		12.5			3		Amplitude never returns on either side. Anomaly does not look as clear on both sides & does not seem deep.
	33	9	9067		10			2		
	34	9	9067		17			1		
16	29	9	9080	9090	26	30	4	3	2.2	Slight drop in amplitude.
	30	9	9080	9090	19	23	4	3		Amplitude drop and waveform change.
	31	9	9080	9090	12	16	4	3		Slight drop in amplitude.
	34	9	9077	9084	9.5	13	3.5	3		
	35	9	9077	9084	17	20	3	3		
	36	9	9073	9085	24.5	29.5	5	3		
17	30	9	9102	9108	36	38.5	2.5	2		Clear drop In amplitude. Size is different for northern vs. southern directions.
	32	9	9102	9108	29	31.5	2.5	2		
	34	9	9102	9108	13.5	16	2.5	3		
	35	9	9100	9106	7.2	9.5	2.3	1		
	36	9	9100	9106	14.9	17.2	2.3	1		
18	3	8	8119		16			3		Amplitude never returns.
	6	8	8112	8120	14	17	3	3		Clear drop in amplitude on both sides.
	7	8	8112	8121	23.8	27	3.2	2		
	8	8	8112	8121	53.8	57	3.2	2		
19	5	8	8192	8197	26	28	2	3		Clear drop in amplitude on both sides. Same size on both sides.
	6	8	8192	8197	16	18	2	3		
	10	8	8186	8193	24	26	2	2		

Table B.2. Overhead *P* wave observations for regions 11 – 19.

Region	OBS #	Seq. #	Crosscutting P	1st Shot #	Last Shot #	Range (km)	Total Size (km)	Quality (1-low 3-high)	Notes
1	15C	2	yes	43078	43081	17	1.4	1	Seen on two OBSs from one direction. Small region.
	16	2	yes	43034	43039	35	2.3	2	
2	16	2	no	43140	43154	26		0	Large drop in amplitude over a huge region. Might be due to range.
	17	2	no	43098	43103	25		0	Change in waveforms; not really a drop in amplitude.
3	17	2	no	43157	43161	17		0	
	18	2	yes	43114	43119	33	2.3	2	Clear drop in amplitude
4	17	2	no	43169	43181	22		0	Large area with drop in amplitude. Might be due to range.
	18	2	no	43131	43134	25		0	No visible decrease in amplitude.
5	58	42	yes	42125	42128	14	1.4	1	Amp drop seen from one direction but not other. Possibly structural.
	60	42	yes	42084	42090	27.5	2.7	1	Very slight decrease in amplitude.
	22	17	no	17068	17070	15		0	No visible drop in amplitude
	23	17	no	17048	17052	14.3		0	
6	58	42	yes	42158	42159	24.5	0.5	1	Very slight decrease in amplitude.
	60	42	yes	42112	42115	20.3	1.4	1	
	22	17	yes	17110	17115	31.2	2.3	1	
	24	17	yes	17059	17063	19	1.8	2	
7	53	42	yes	42157	42162	22.4	2.3	1	
	60	42	yes	42157	42163	14.7	2.7	1	
	61	42	yes	42146	42150	17.5	1.8	1	Very slight decrease in amplitude.
	24	17	yes	17094	17099	16.5	2.3	1	Decrease and waveform change
8	52	2	yes	2129	2139	12	4.5	1	Slight decrease in amplitude. Region size changes from different directions
	53	2	yes	2107	2111	14	1.8	1	
	56	2	yes	2075	2077	40	0.9	2	
	16	15	yes	15071	15077	13	2.7	1	
9	53	2	yes	2156	2160	16	1.8	3	Multiple areas with decreases in wave amplitude.
	53	2	yes	2172	2174	20.5	0.9	3	
	53	2	yes	2193	2198	29	2.3	3	
	54	2	no	2144	2146	12.4		0	
	47	2	yes	2134	2136	17.4	0.9	1	
	55	2	yes	2127	2128	17	0.5	1	
	56	2	yes	2099	2110	29	5.0	3	Large area with same shot numbers as other OBS. Might be from a topographic affect.
	49	2	yes	2100	2110	33	4.5	3	
	49	2	yes	2115	2117	29	0.9	2	
	23	15	yes	15091	15091	20.5	1.0	1	Very slight decrease in amplitude, possibly due to range.
	23	24	yes	24098	24103	29.6	2.3	3	
	24	15	no	15077	15092	19.7		0	
	24	24	yes	24077	24092	27.5	6.8	3	Could be a reflector or possible PmP interferance.
	16	22	yes	22098	22111	23.5	5.9	3	Large area with amp drop. Possible PmP interferance.
	17	13	yes	13065	13070	23.5	2.3	3	

Table B.3. Crosscutting *P* wave observations for regions 1 – 9.

Region	OBS #	Seq. #	Crosscutting P	1st Shot #	Last Shot #	Range (km)	Total Size (km)	Quality (1-low 3-high)	Notes
10	55	2	yes	2166	2175	15	4.1	3	Nice clear drop in amp.
	49	2	yes	2128	2136	23	3.6	2	
	17	15	yes	15088	15093	14.7	2.3	1	
11	49	2	no	2190	2195	21		0	
	50	2	no	2171	2175	20.7		0	
	17	13	yes	13134	13139	22	2.3	1	
12	42	6	no	6067	6068	22		0	Seen on two OBSs from 2 directions but ruling out since looks like surface topography on Seq. 24.
	43	6	yes	6041	6047	29	2.7	2	
	3	26	no	26020	26024	27.9		0	
	11	26	no	26024	26028	20		2	
	11	24	yes	24025	24028	18	1.4	0	
13	42	6	no	6101	6103	29.5		0	Mostly small regions.
	43	6	yes	6076	6078	21	0.9	1	
	44	6	yes	6054	6056	30	0.9	2	
	11	24	yes	24050	24055	21	2.3	2	
	12	24	yes	24023	24027	26	1.8	3	
14	42	6	yes	6118	6121	27.8	1.4	1	Very small decreases in amplitude.
	43	6	yes	6094	6108	20.2	6.3	1	
	11	24	yes	24061	24066	23	2.3	1	
	12	24	yes	24038	24044	20.4	2.7	1	
15	43	6	no	6128	6130	24		0	Slight drop in amplitude in from only one direction.
	45	6	no	6109	6111	18.5		0	
	38	6	no	6095	6098	18		0	
	12	24	yes	24061	24063	15	0.9	1	
16	40	6	yes	6100	6106	23	2.7	1	
	47	6	yes	6116	6121	18.5	2.3	1	Very slight decrease in amplitude.
	39	6	yes	6125	6126	13.3	0.5	1	
	46	6	no	6131	6132	16.6		0	
	38	6	yes	6132	6145	15	5.9	2	
	6	13	yes	13071	13080	26	4.1	3	
	5	13	yes	13076	13080	24	1.8	1	
	12	24	yes	24095	24101	18	2.7	3	Clear drop in amplitude
	4	26	yes	26096	26101	28.3	2.3	3	
	4	13	yes	13100	13106	30.5	2.7	3	
17	39	6	no	6161	6163	15		0	
	40	6	no	6153	6156	11.2		0	
	12	24	no	24120	24123	25.2		0	
18	11	40	no	40152	40154	43		0	
	12	40	no	40108	40114	15		0	
19	35	40	no	40179	40187	25		0	
	36	40	no	40170	40175	17.5		0	
	14	40	no	40152	40160	18		0	

Table B.4. Crosscutting *P* wave observations for regions 10 – 19.

Region	(1) Ranking	(1) Number of OBSs	(2) Ranking	(2) Number of OBSs	Overall Ranking	Estimated Max Depth of Anomaly (km)	Average Size of Anomalous Region (1) (km)	Average Size of Anomalous Region (2) (km)	Comments
16	3.0	6	1.3	10	2.2	2.2	3.9	2.8	Slight decrease in amplitude from overhead shots. Very clear drop in amplitude from several crosscutting shots.
9	1.5	4	2.1	10	2.0	2.2		2.7	Amplitude does not return on the overhead shots. Unable to determine size of area due to this. Multiple and large areas are observed in the crosscutting shots. Seen from several crosscutting shots.
8	3.0	6	1.3	4	1.8	2.2	4.6	2.5	Clear decrease in amplitude seen on Northern and Southern sides of OBSs in overhead shots. Slight decrease in amplitude in crosscutting shots. Region size changes from different directions
10	1.8	5	2.0	3	1.9	2.2	1.7	2.6	Small regions. Clear drop in amplitude from overhead and crosscutting shots.
18	2.5	4	0.0	2	1.7		3.0		Clear decrease in amplitude seen on Northern and Southern sides of OBSs in overhead shots. No amplitude loss seen in crosscutting shots. Will not include in list of identified LVVs.
6	2.0	4	1.3	4	1.6	0.8	4.3	1.5	Very clear decrease in amplitude on both sides from overhead shots. Large region. Very slight decrease in amplitude in crosscutting shots. Due to a significant change in topography at this location, AV 6 is not included in list of identified LVVs.
14	2.3	4	1.0	4	1.6	2.0		3.2	Amplitude never returns on either side on overhead shots. Anomaly looks clear on both sides, but does not seem deep. Very small decreases in amplitude for crosscutting shots.
13	1.5	4	1.6	5	1.6	2.4	6.6	1.2	Large region; not as clear as other regions. Crosscutting shots show the region as being small.
4	2.7	3	0.0	2	1.6			3.6	Amplitude never returns for overhead shots. Not visible in crosscutting shots. LVVs 4 and 5 may possibly be one zone.
11	2.5	4	0.3	3	1.6		2.7	2.1	Clearly seen from the southern side but not as well from the north.
7	2.0	3	1.0	4	1.4	2.4	2.4	2.3	Clear drop in amplitude on both sides from overhead shots. Decrease and waveform change observed from crosscutting shots.
3	1.7	3	1.0	2	1.4		1.5	2.0	Amplitude does not return on the overhead shots. No amplitude decrease is observed in crosscutting shots.
1	1.3	4	1.5	2	1.3		1.6	1.8	Decrease in amplitude can clear be seen on both sides of the OBS. Small region. Seen on two OBSs from one direction with crosscutting waves. Small region.
19	2.7	3	0.0	3	1.3		2.0	3.2	clear drop in amplitude on both sides. Same size on both sides. Not visible from crosscutting shots.
5	2.3	3	0.5	4	1.3		1.5	1.7	Small region. Decrease in amplitude from overhead shots. Amplitude decrease seen from only one direction in crosscutting shots. Possibly caused by topography.
2	1.5	4	0.5	2	1.2		3.2	4.3	Clear drop in amplitude on both sides from overhead shots. Not visible from crosscutting shots.
17	1.8	5	0.0	3	1.1		2.4	1.2	Clear drop In amplitude. Size is different for northern vs. southern directions. Not visible from crosscutting shots.
12	1.5	4	0.8	5	1.1		3.6	1.6	Shots do not cover wide enough of a region to examine from overhead shots. Only see on one side. Seen on two OBSs from 2 directions (crosscutting shots) but ruling out since looks like surface topography on shot sequence 24
15	2.0	3	0.3	4	1.0			1.0	Amplitude never returns on either side (overhead shots). Anomaly does not look as clear on both sides & does not seem deep. Slight decrease in amplitude is seen from only one direction in crosscutting shots.

Table B.5. Regions listed by their overall quality rank. The seven identified amplitude anomalies are placed in three tier groups by their overall quality. The best-observed potentially anomalous regions are regions 16 and 9 (blue), followed by regions 8 and 10 (green), and lastly regions 14, 13, and 7 (yellow). The seven identified amplitude anomaly locations are shown in **Figure 4.8** (regions 13 and 14 are combined as one zone, region 13-14). All the amplitude anomaly locations are shown in **Figure 4.1**.

APPENDIX C

P WAVES FOR PROFILES CROSSING DIRECTLY OVER OBSS

I examine the outer eastern and western regions of the Endeavour segment, observing the *P* wave travel times and amplitudes. I look through seismic records for shot sequences that passed directly over specific OBSs. **Figures C.1** through **C.19** show the nineteen amplitude anomalies that are identified. The record sections are shown for the vertical or hydrophone channel, dependent upon which channel has the clearest recorded waveforms. The bold colored line shows the range and shot number where the *P* wave's amplitude decreases, and the thinner lines show where the zones of lowered amplitude end. A corresponding colored arrow on the bathymetric map shows the location of the initial amplitude decrease. On the bathymetric maps, EW0207 reflection survey lines are shown in gray. The lines on the seismic records show the predicted (blue), picked (red), and disrupted and/or low-amplitude (green) *P* wave arrivals. Comments for each record section are listed in **Appendix B** (**Tables B.1** and **B.2**). The record sections are fix scaled, plotted with a velocity reduction of 7.2 km/s, and are band-pass filtered between 5 and 15 Hz or 5 and 30 Hz, dependent upon waveform clarity.

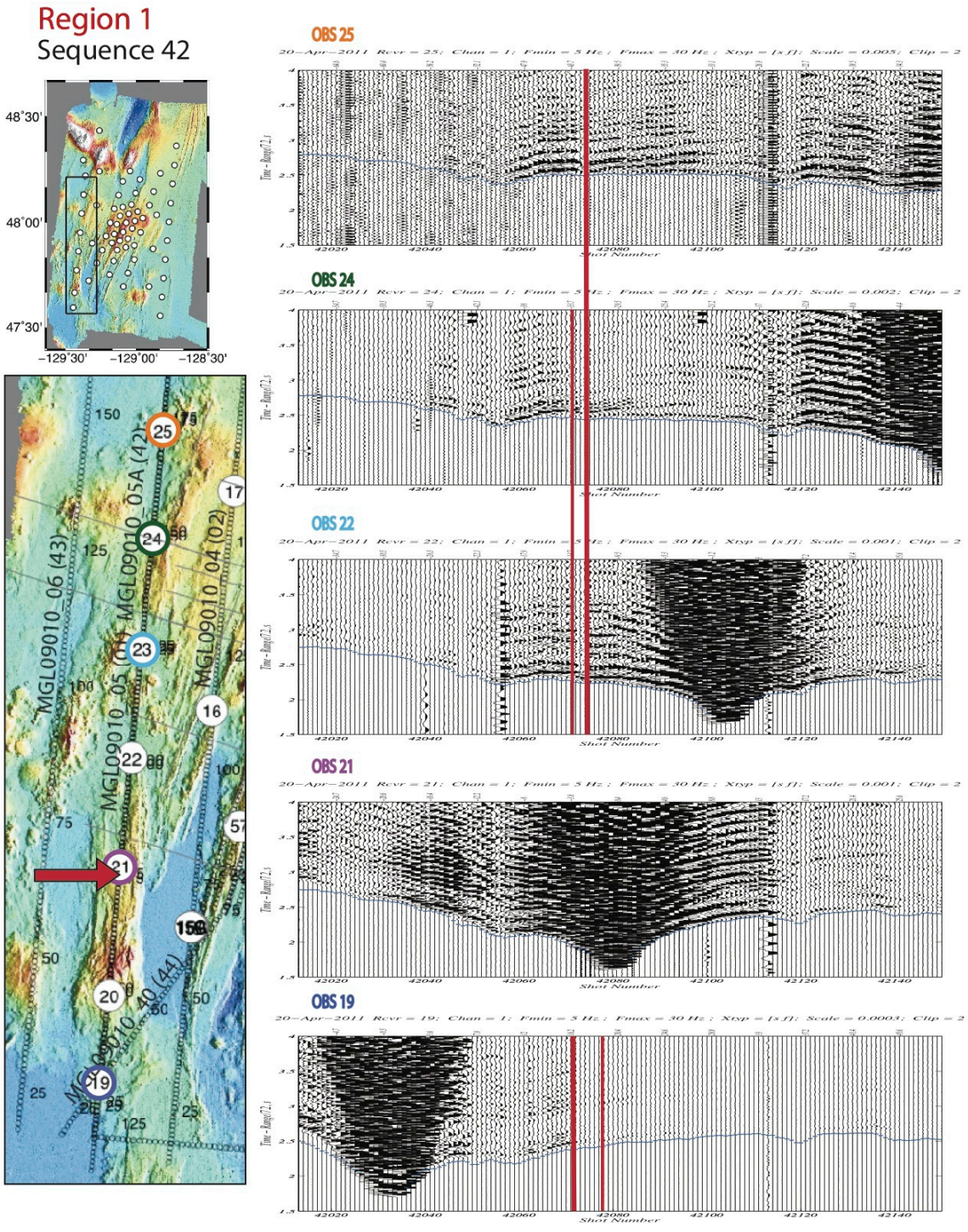

Figure C.1. Region 1 (red).

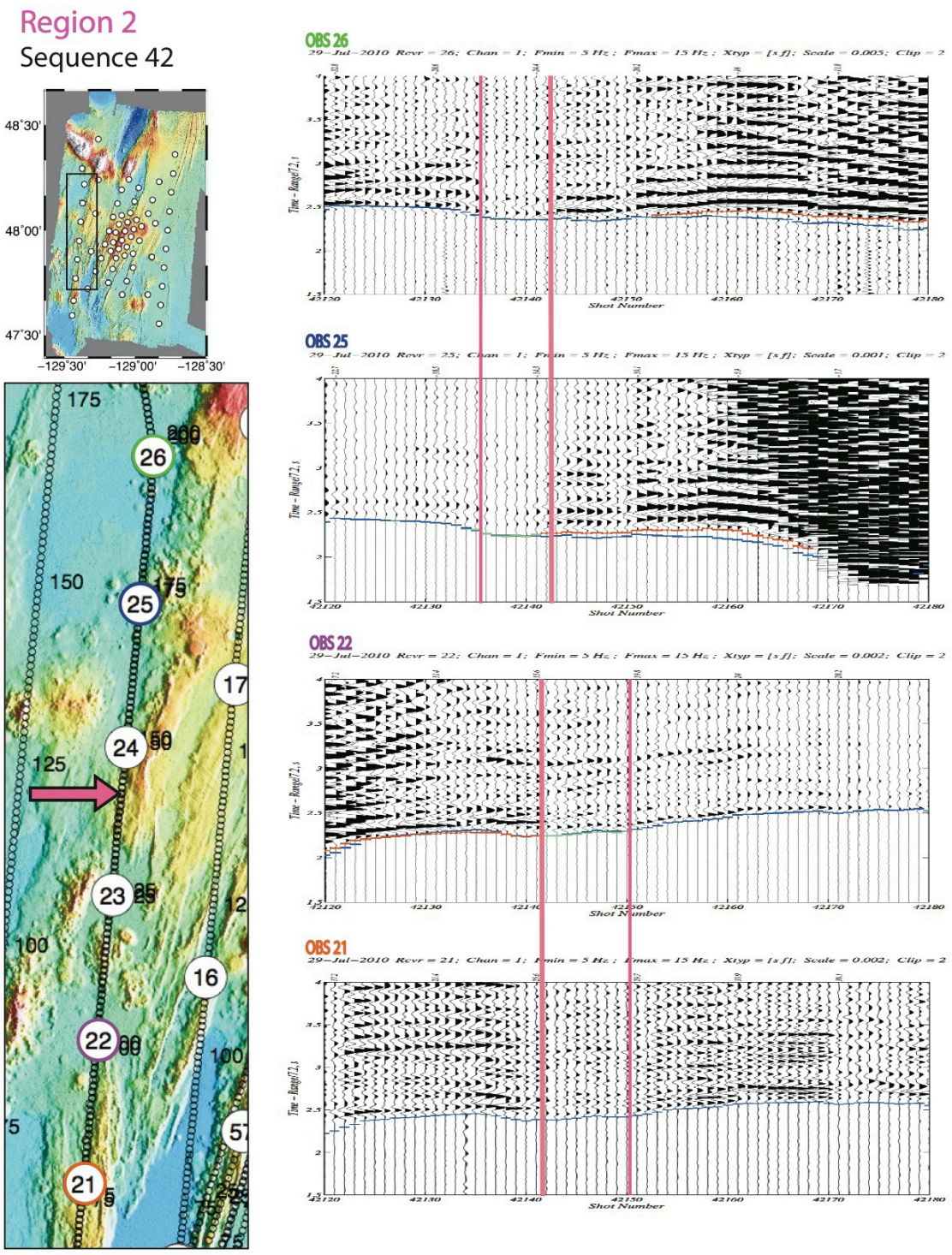

Figure C.2. Region 2 (pink).

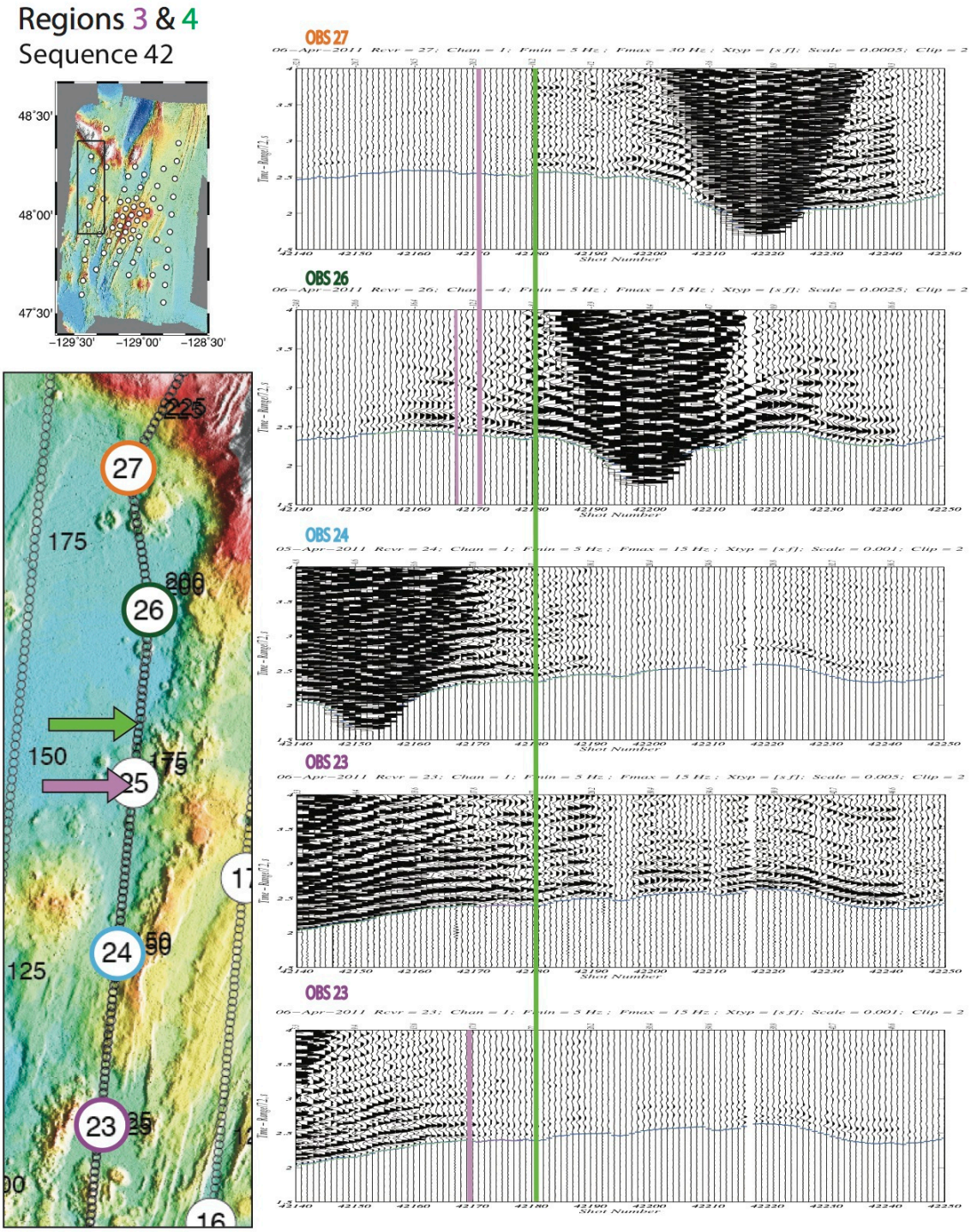

Figure C.3. Regions 3 (lavender) and 4 (light green).

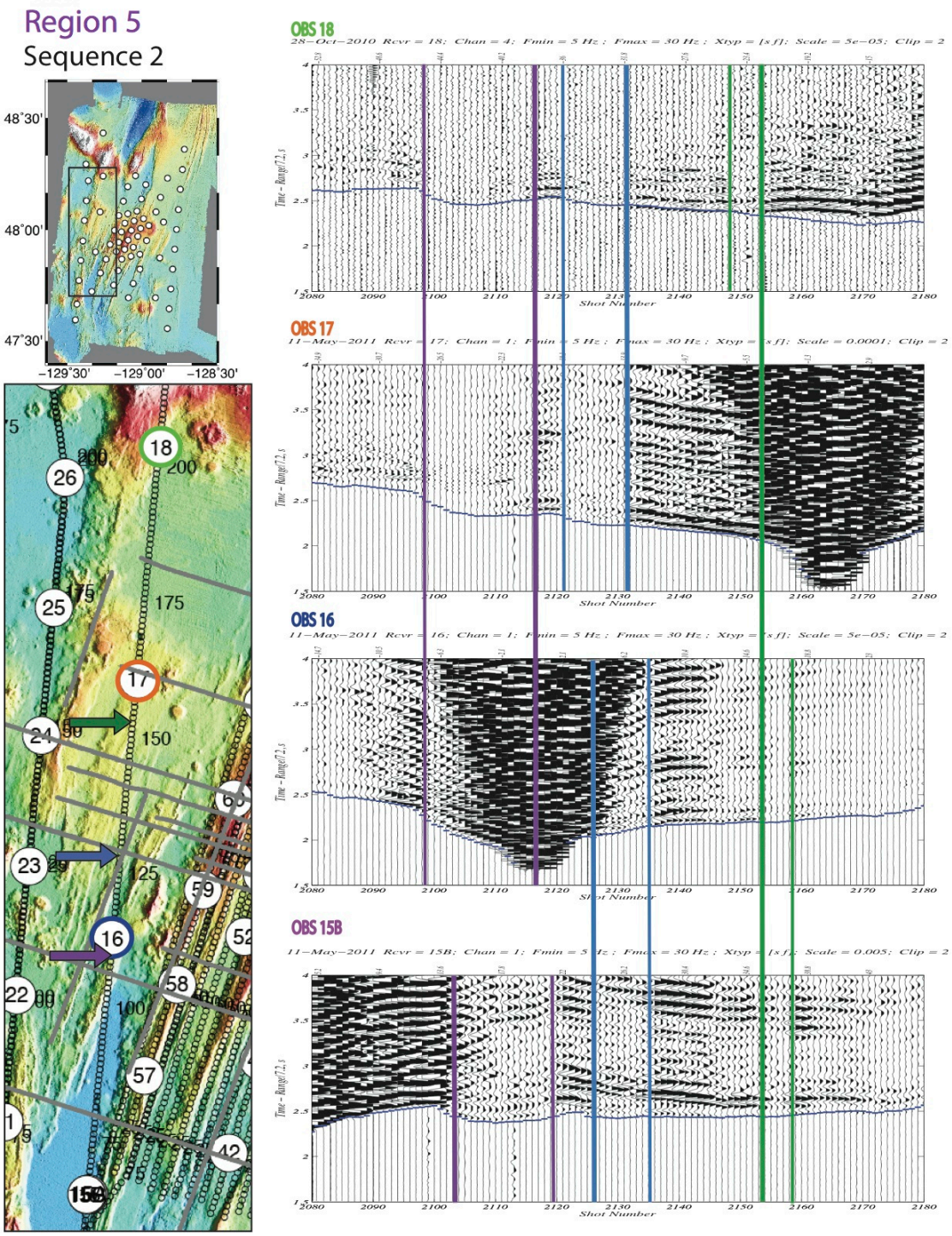

Figure C.4. Region 5 (purple).

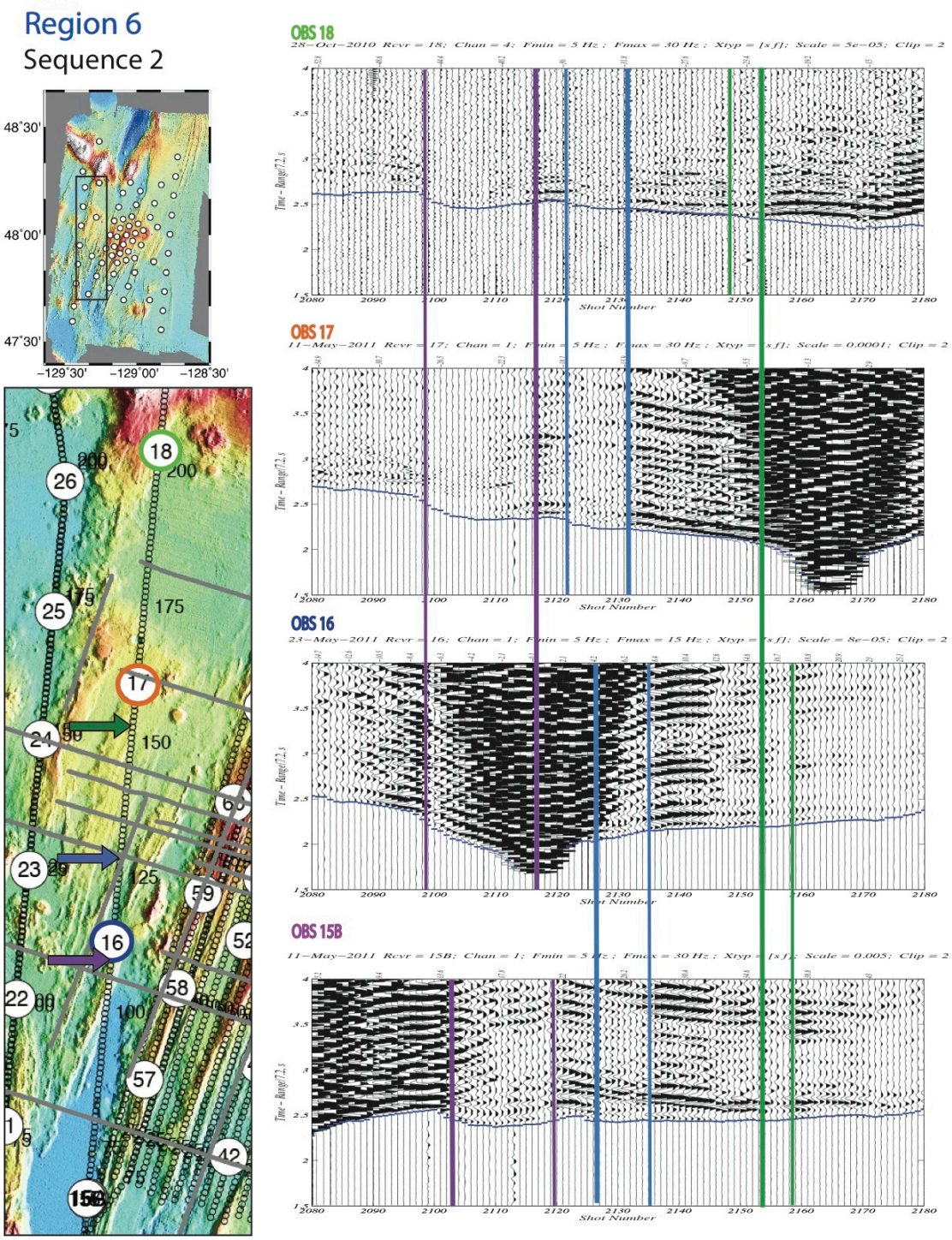

Figure C.5. Region 6 (blue).

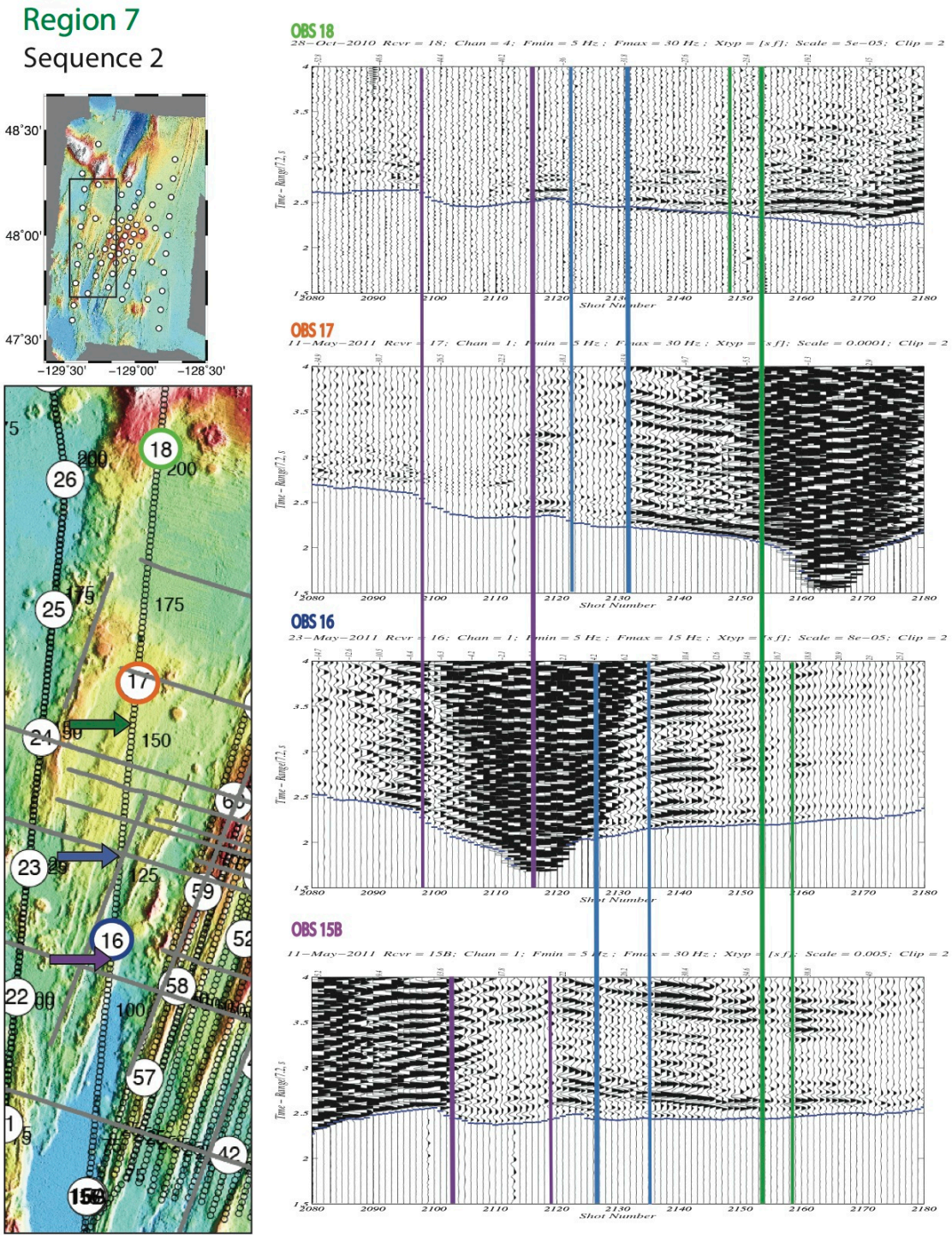

Figure C.6. Region 7 (green).

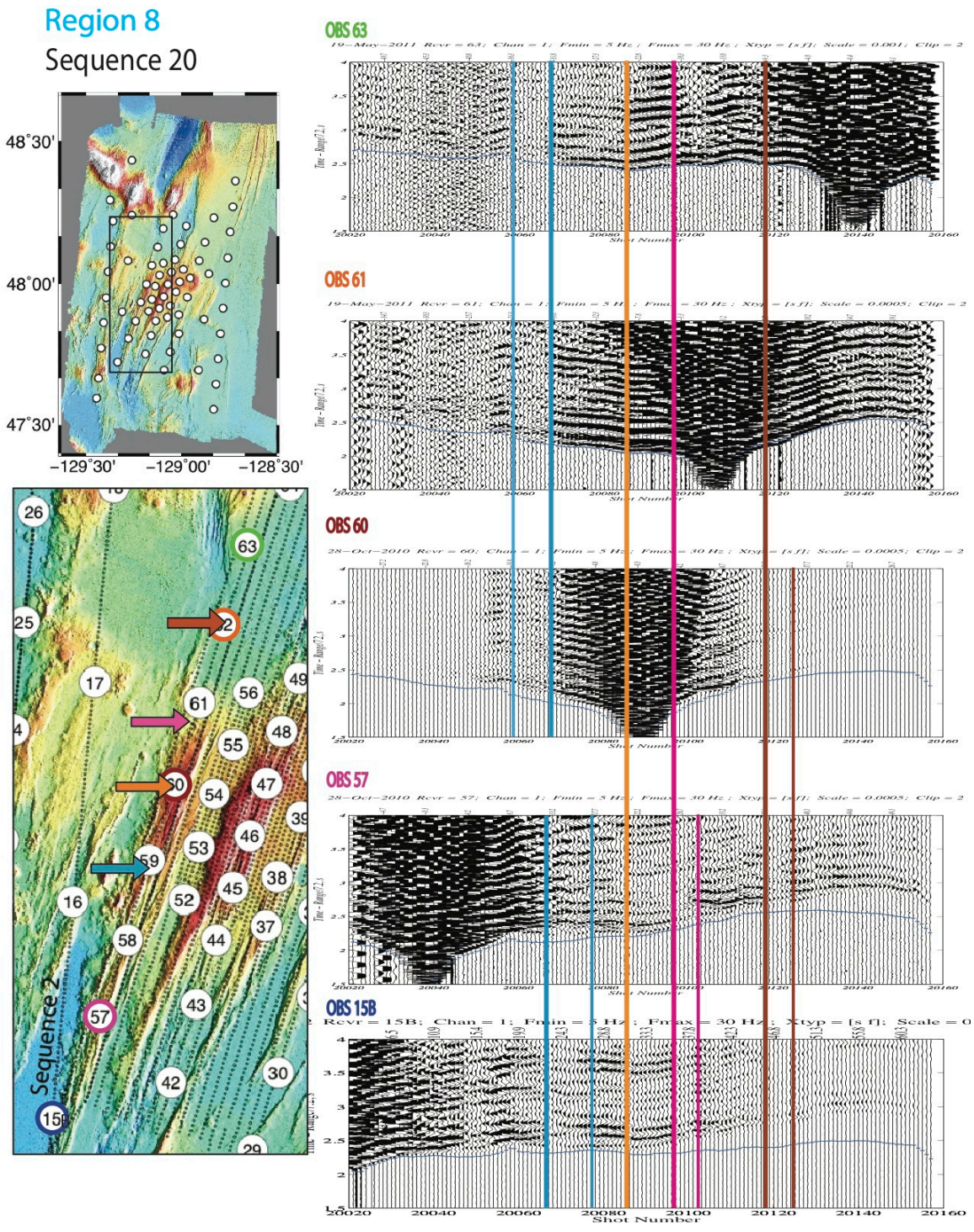

Figure C.7. Region 8 (blue).

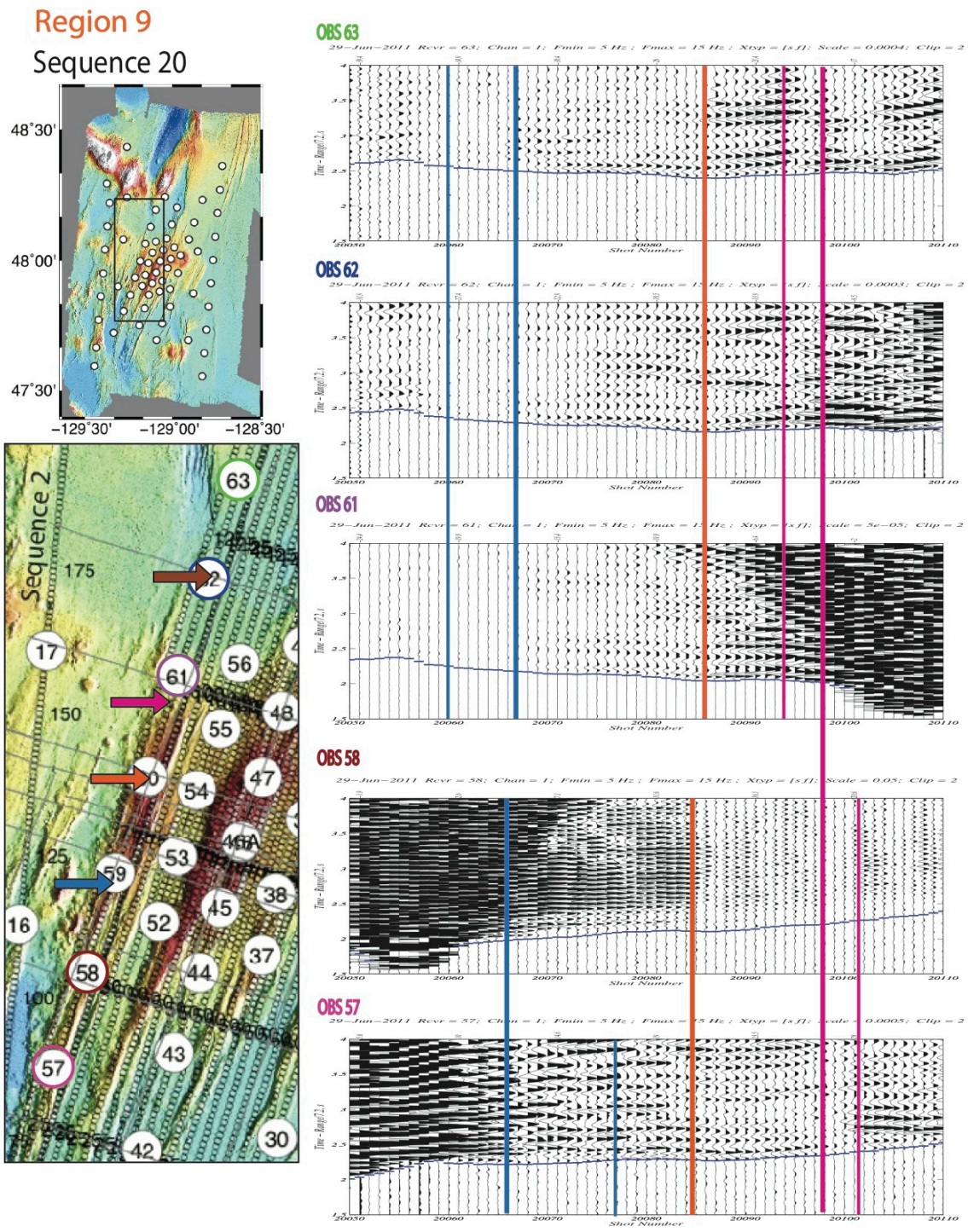

Figure C.8. Region 9 (orange).

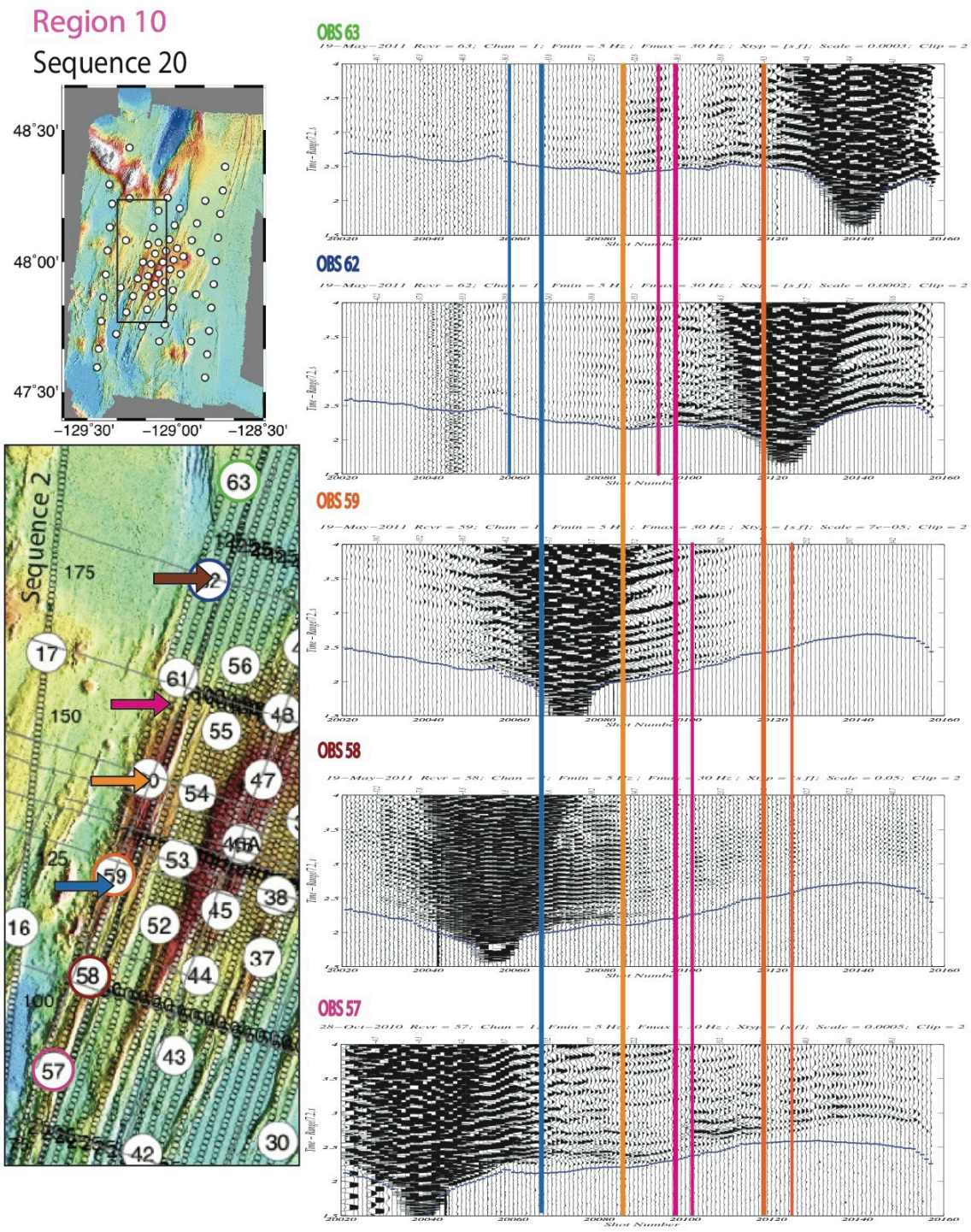

Figure C.9. Region10 (pink).

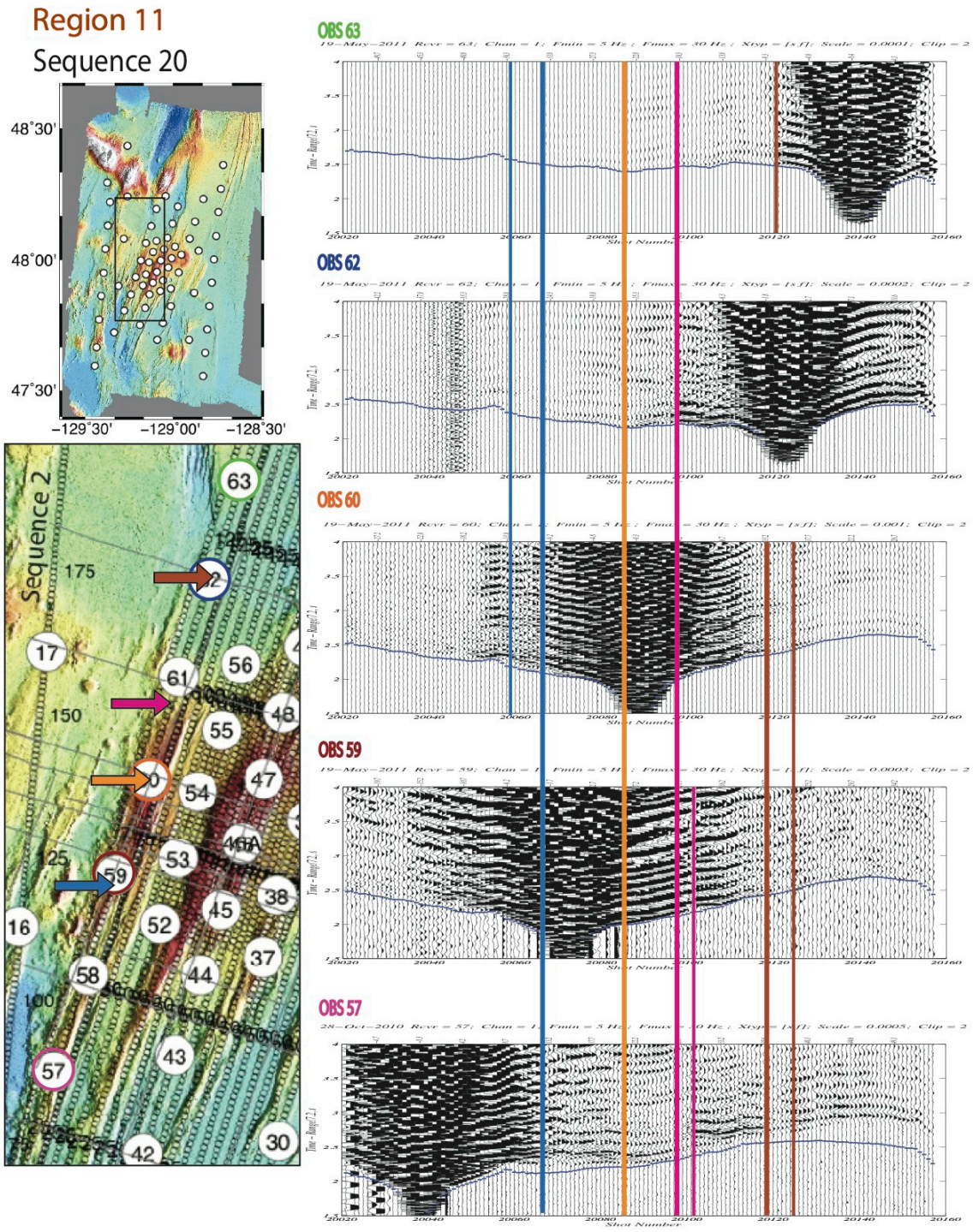

Figure C.10. Region 11 (dark orange).

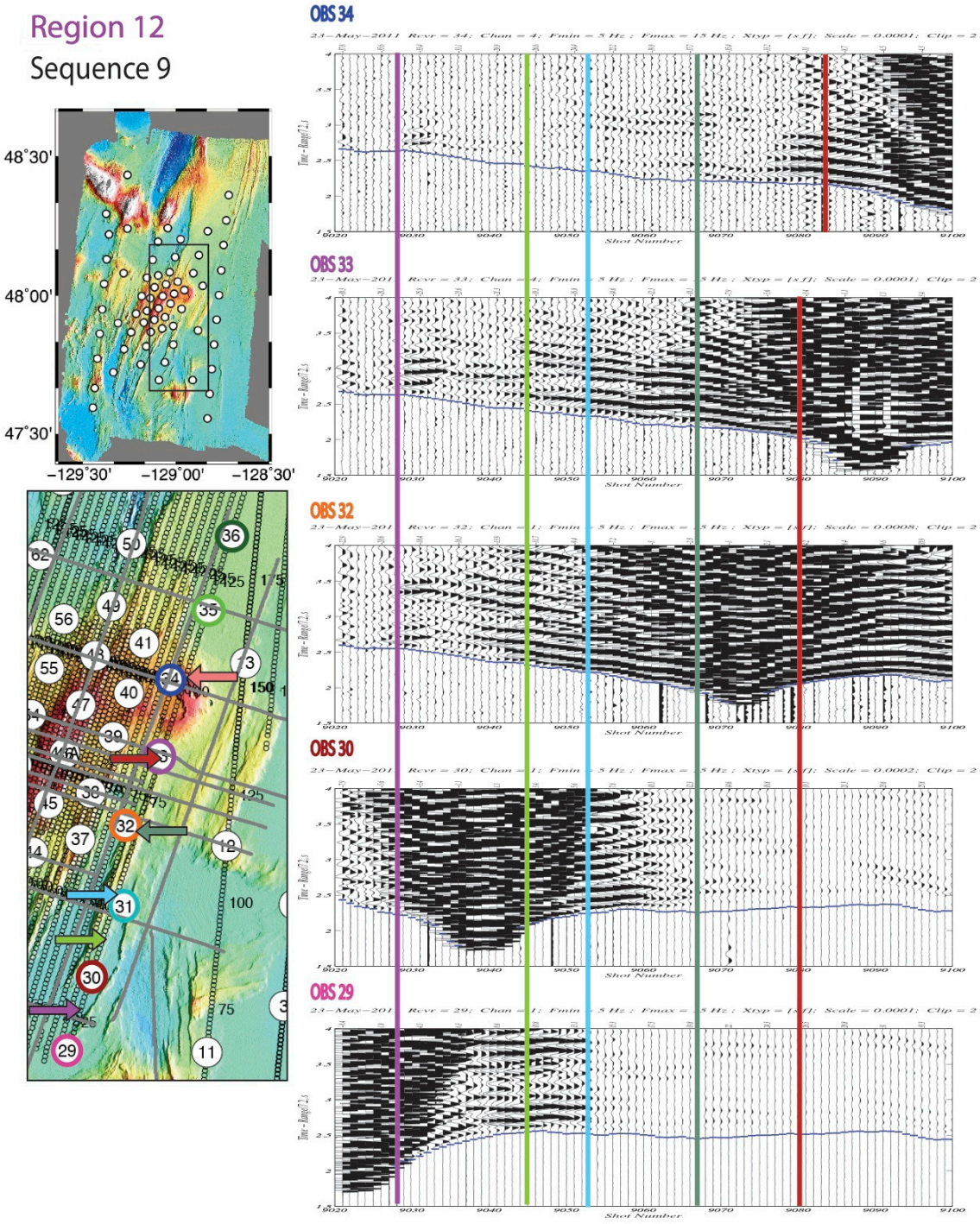

Figure C.11. Region 12 (purple).

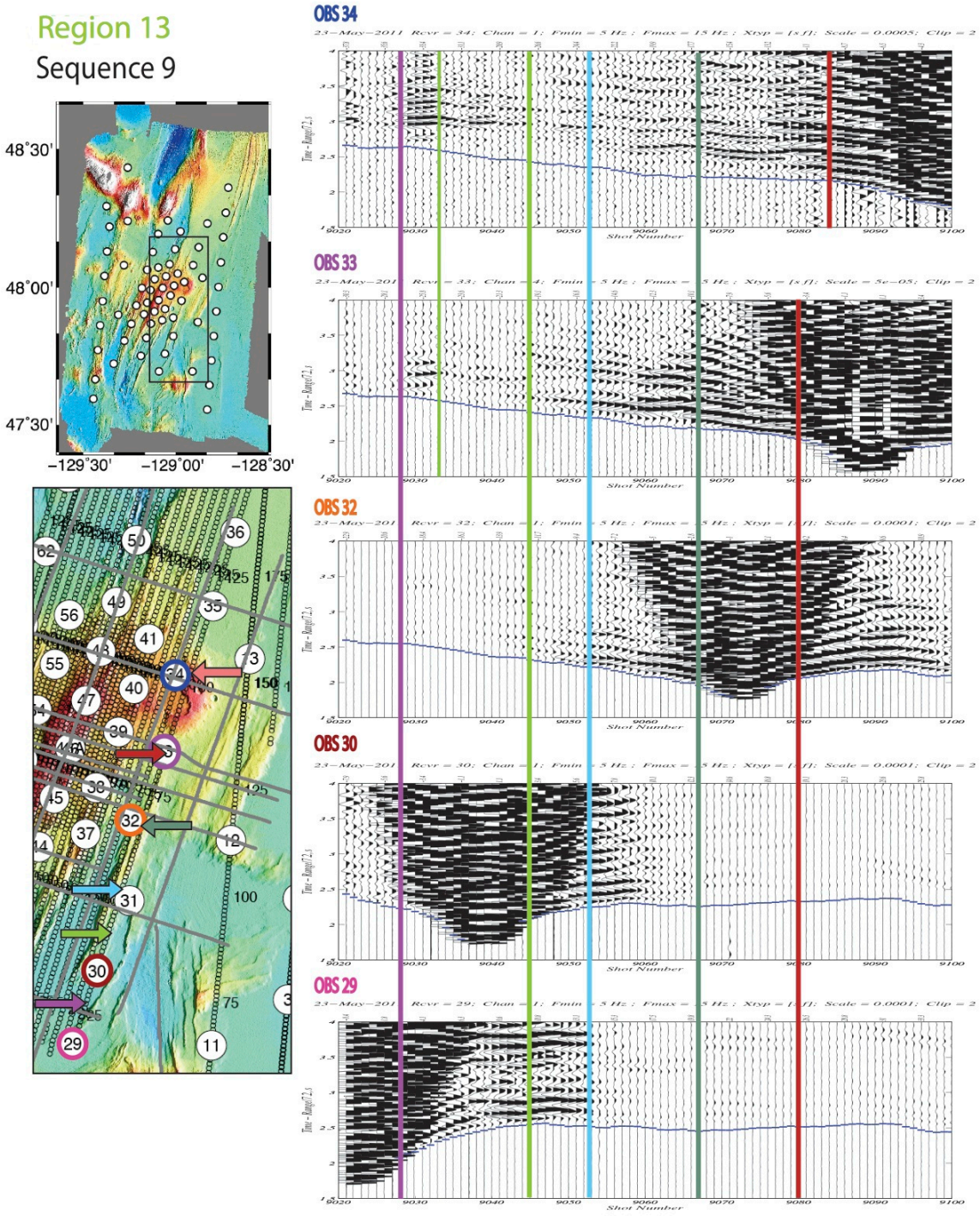

Figure C.12. Region 13 (light green).

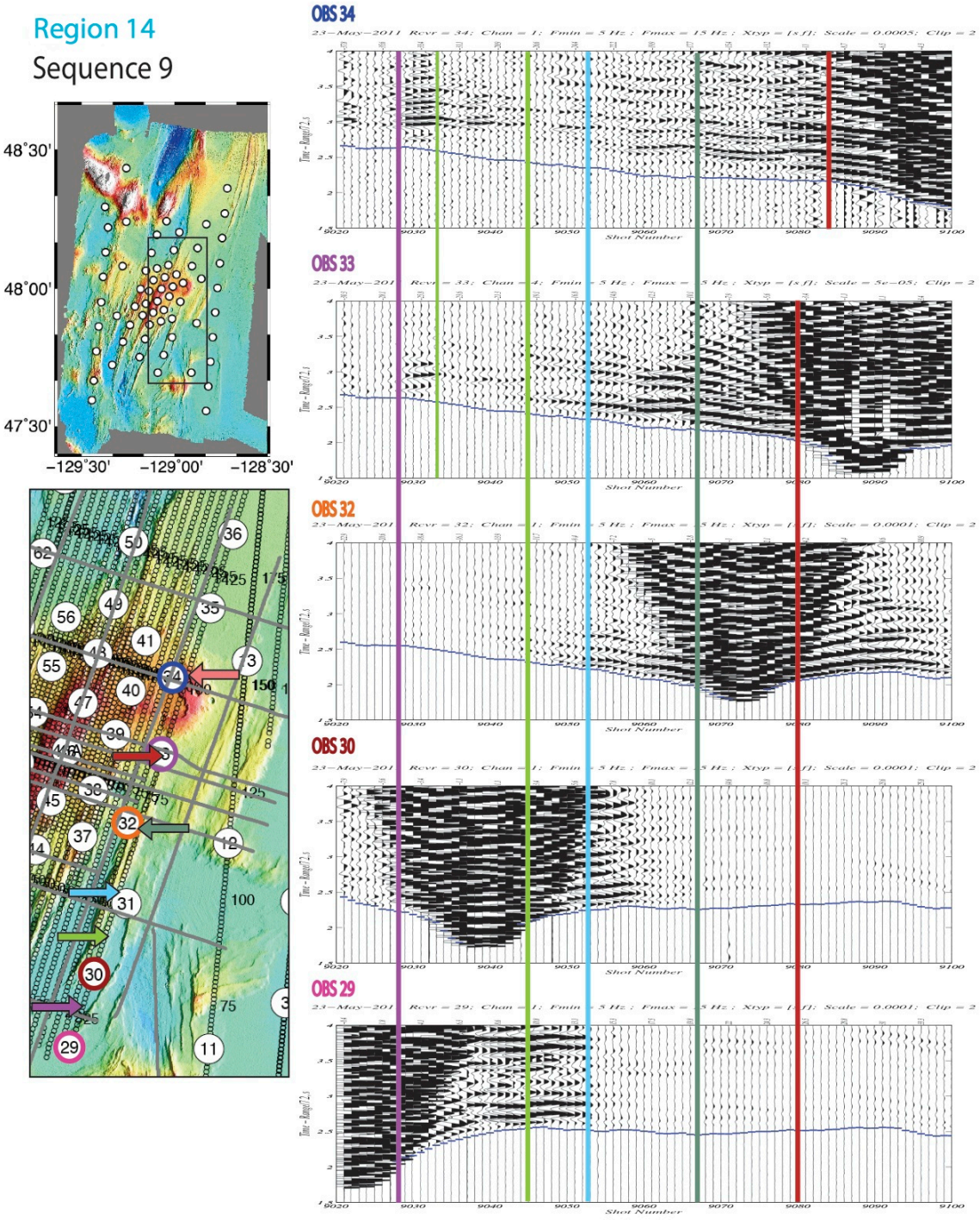

Figure C.13. Region 14 (light blue).

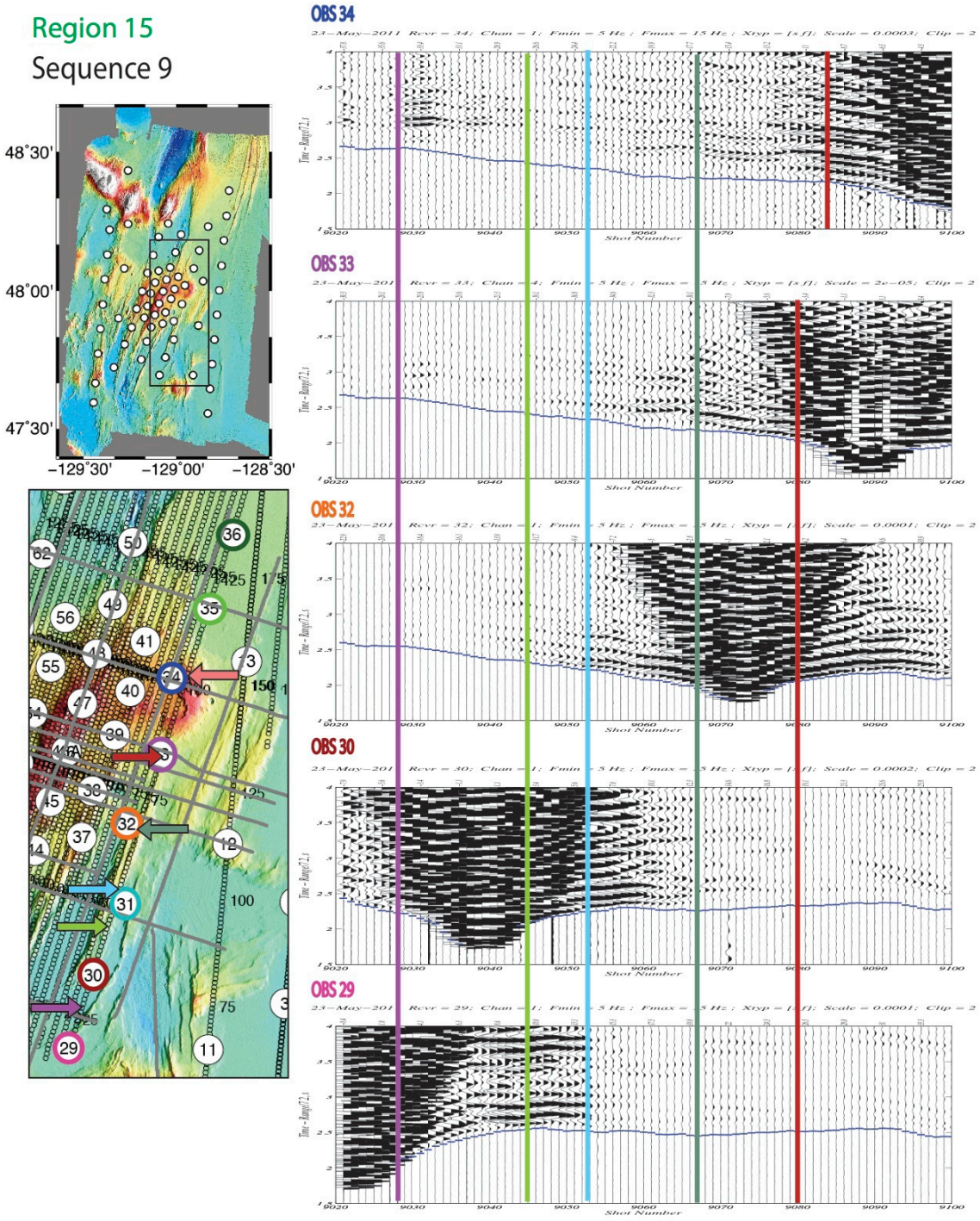

Figure C.14. Region 15 (dark green).

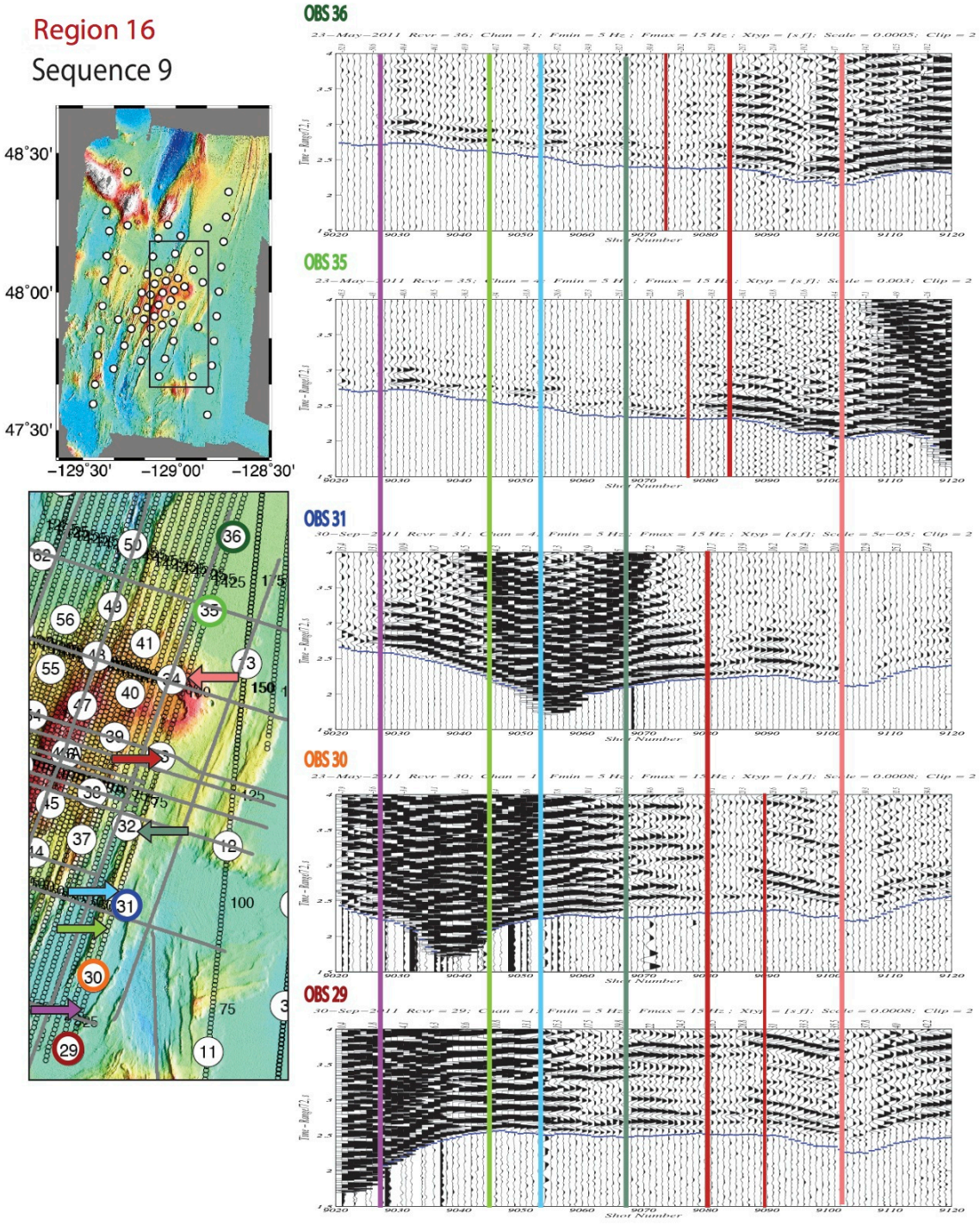

Figure C.15. Region 16 (red).

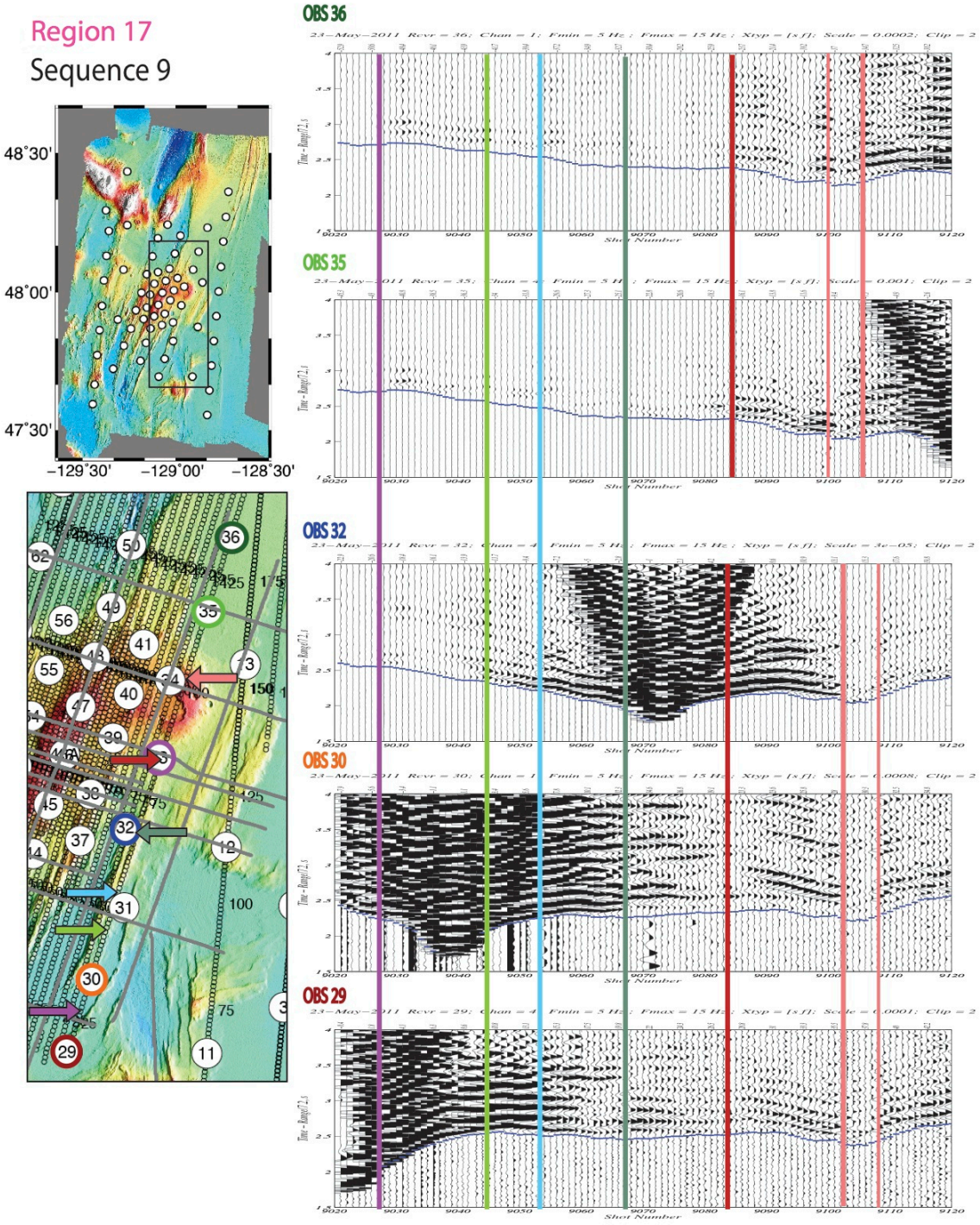

Figure C.16. Region 17 (pink).

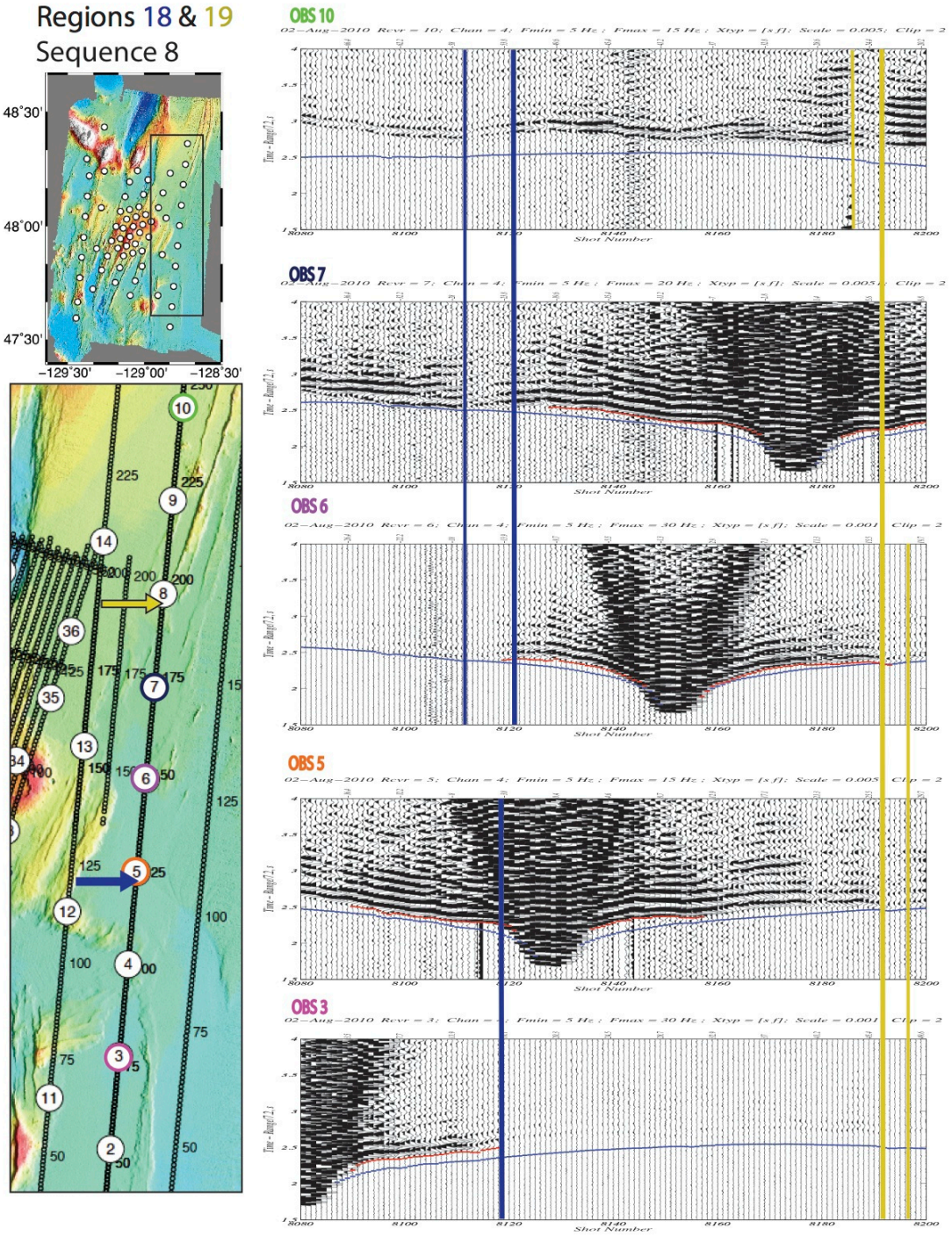

Figure C.17. Regions 18 (blue) and 19 (yellow).

APPENDIX D

P WAVES FOR PROFILES CROSSCUTTING THROUGH THE AMPLITUDE ANOMALIES

I examine the identified amplitude anomalies by observing the *P* waves crossing through the regions from different directions. I look through seismic records are for shot sequences, where the initial *P* waves will cross through the amplitude anomaly on their path to the OBS. The crosscutting *P* waves are examined from multiple directions for the identified amplitude anomalies. The record sections are shown for the vertical or hydrophone channel, dependent upon which channel has the clearest recorded waveforms. The colored bars on the seismic records show the shots with diffracted *P* wave arrivals. The paths of the diffracted waves are shown on the maps by a corresponding colored line. An arrow shows the location of the amplitude anomaly examined. On the bathymetric maps, EW0207 reflection survey lines are shown in gray. The lines on the seismic records show the predicted (blue), picked (red), and disrupted and/or low-amplitude (green) *P* wave arrivals. Comments for each record section are listed in **Appendix B** (**Tables B.3** and **B.4**). The record sections are fix scaled, plotted with a velocity reduction of 7.2 km/s, and are band-pass filtered between 5 and 15 Hz or 5 and 30 Hz, dependent upon waveform clarity.

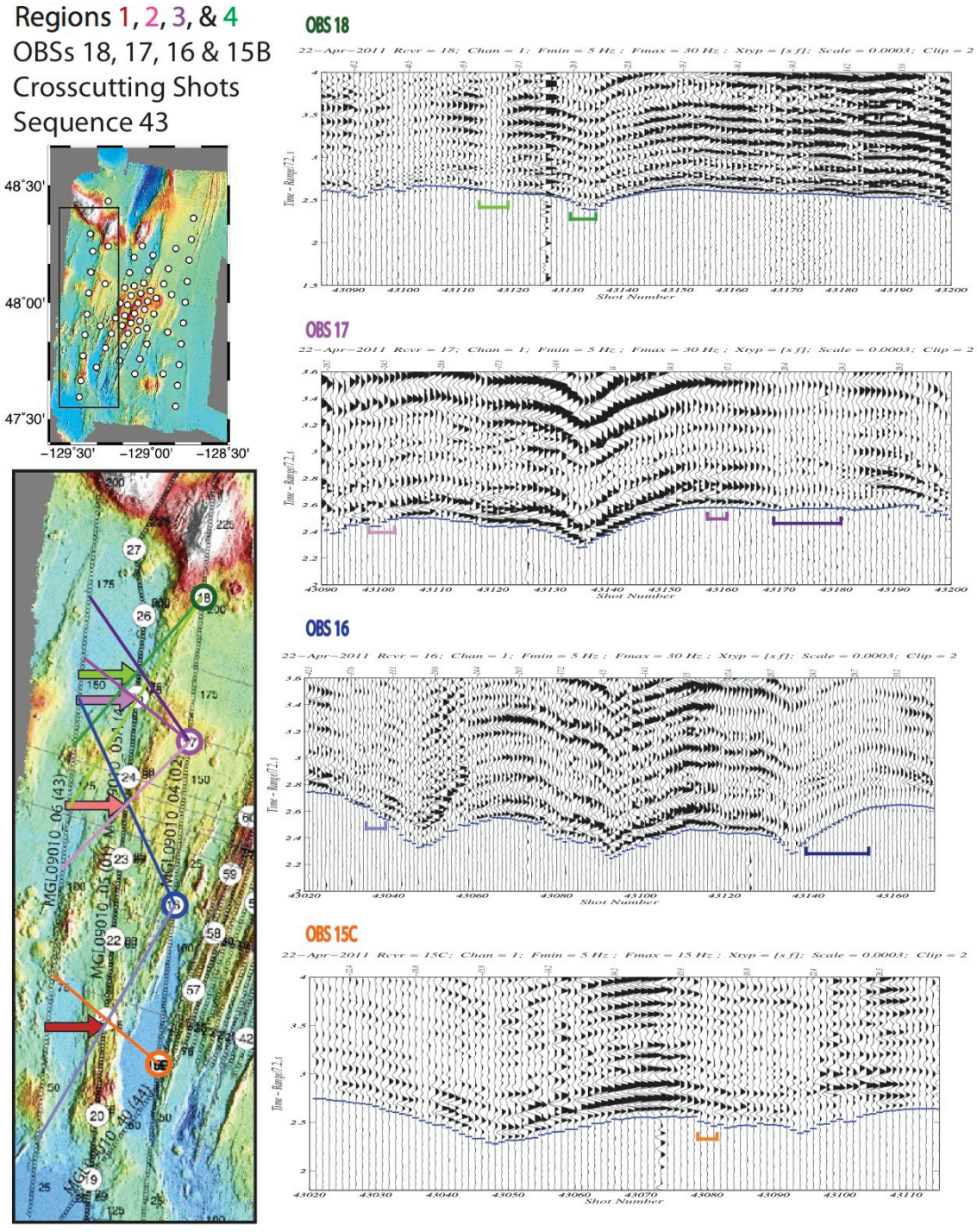

Figure D.1. Regions 1 (red), 2 (pink), 3 (lavender), and 4 (light green).

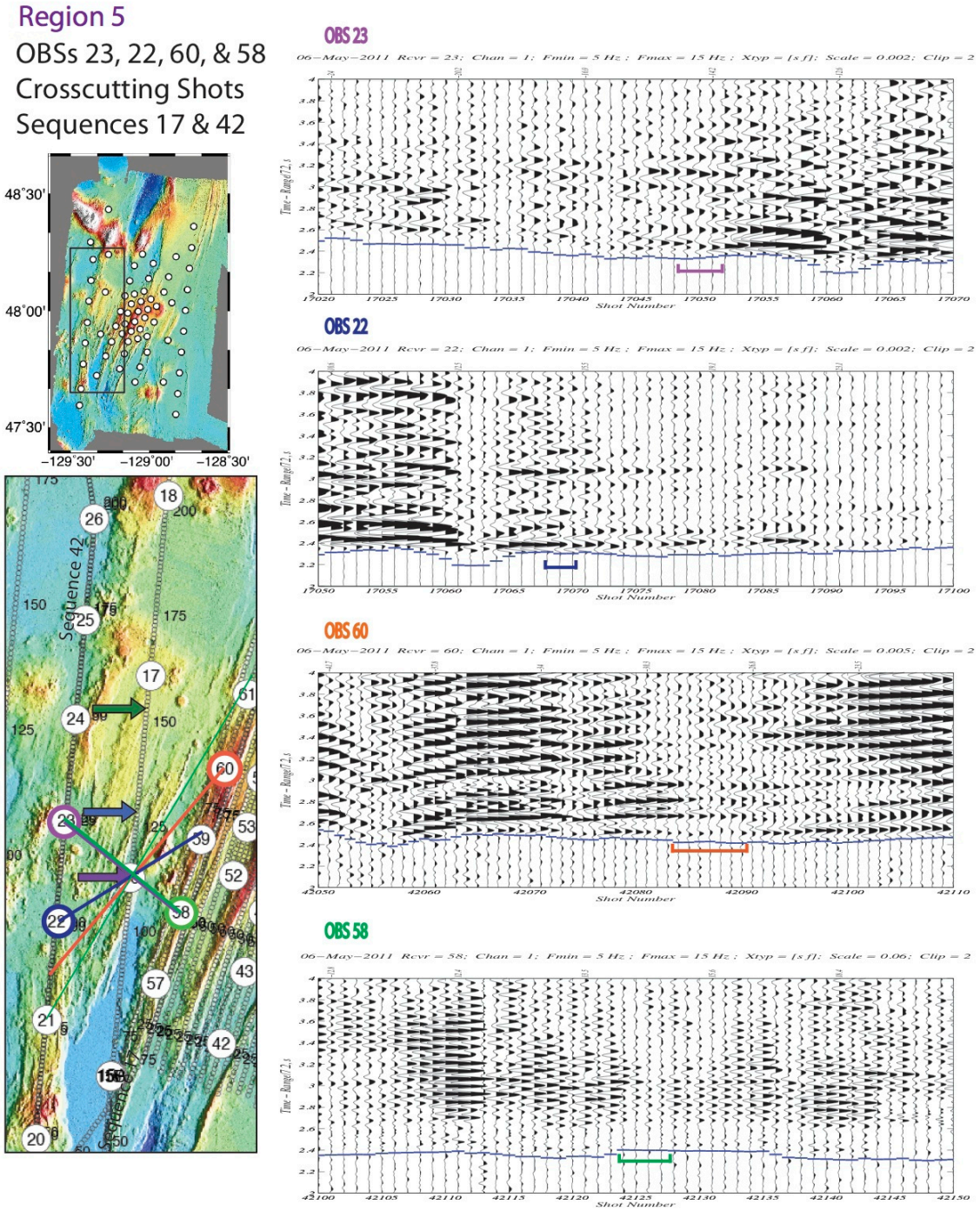

Figure D.2. Region 5 (purple).

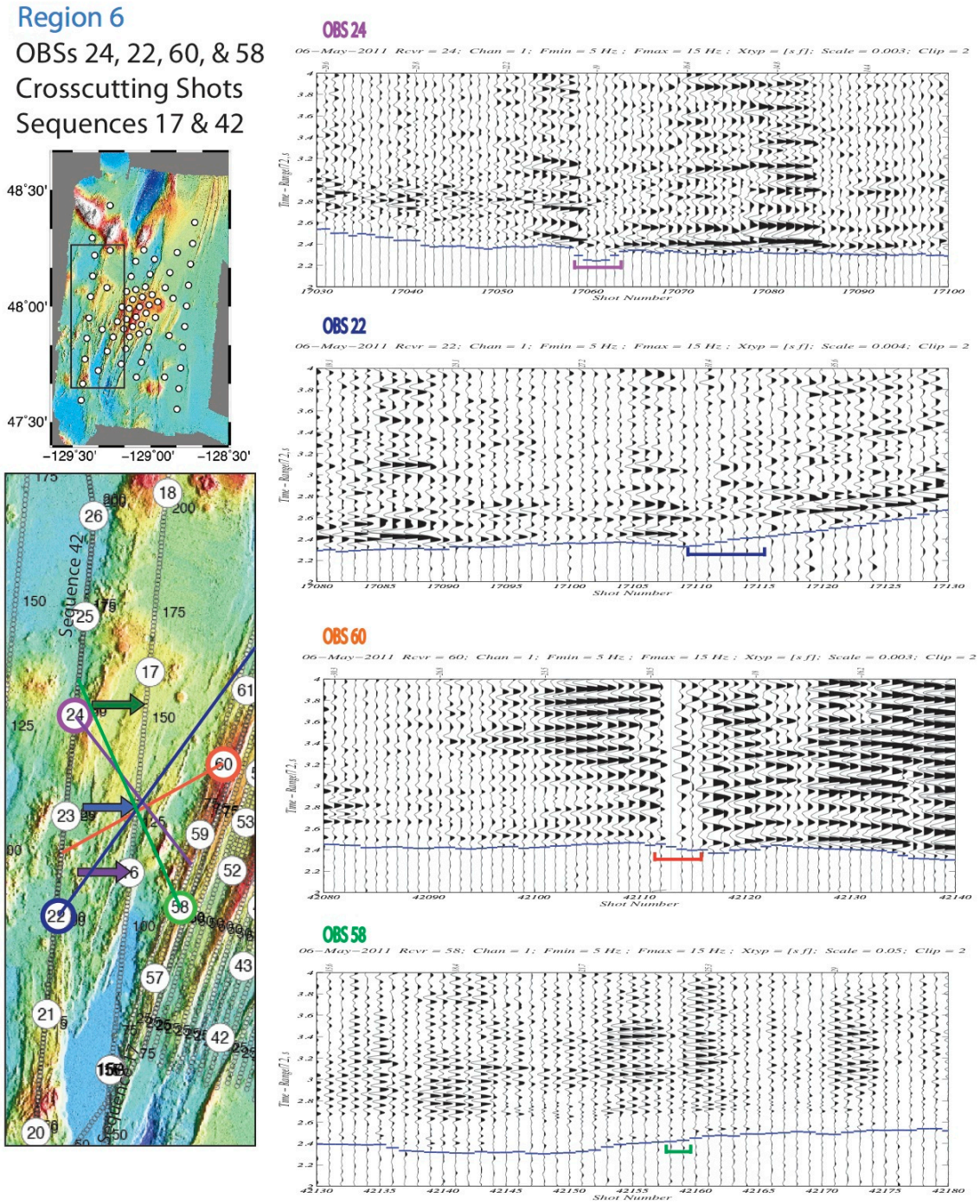

Figure D.3. Region 6 (blue).

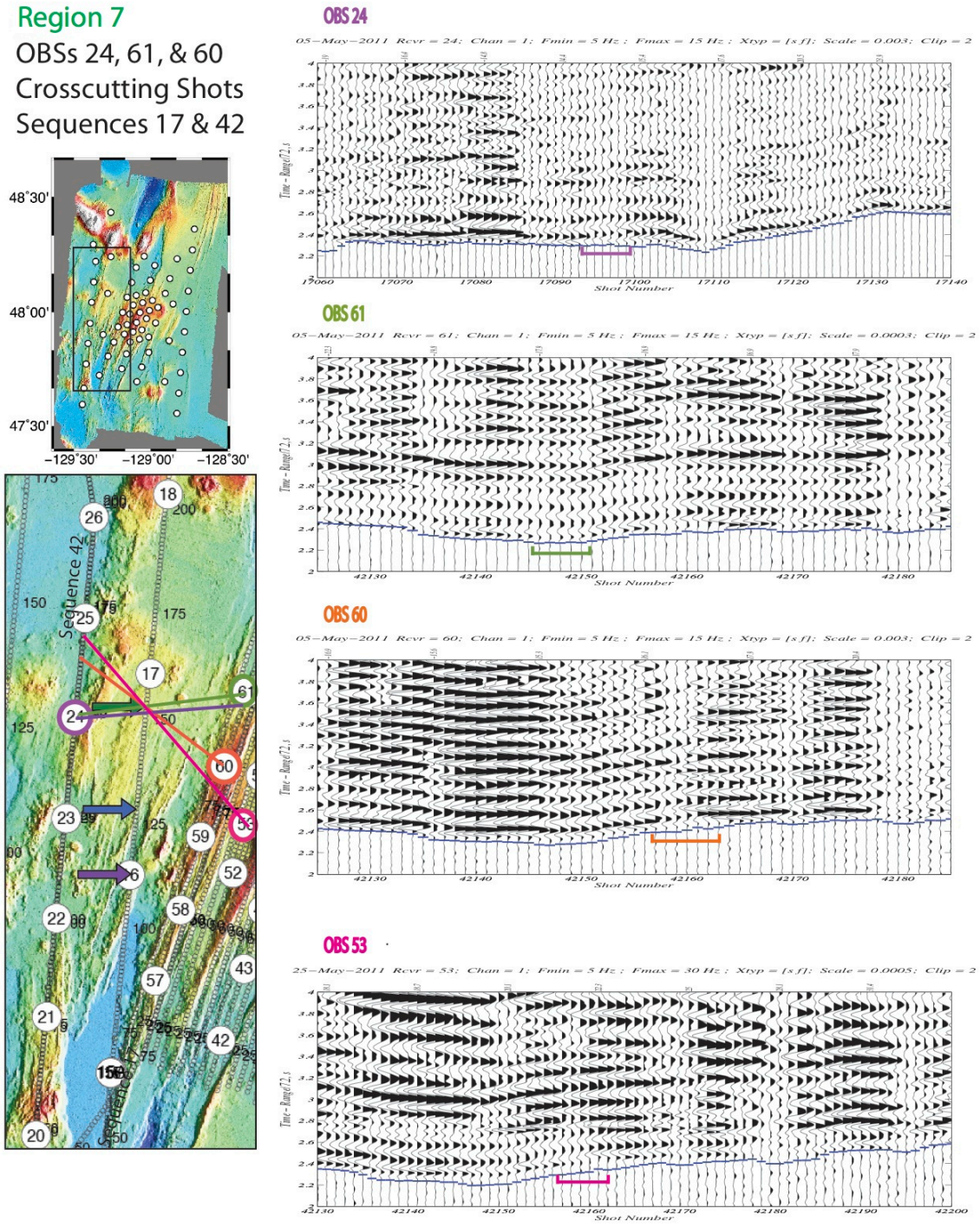

Figure D.4. Region 7 (green).

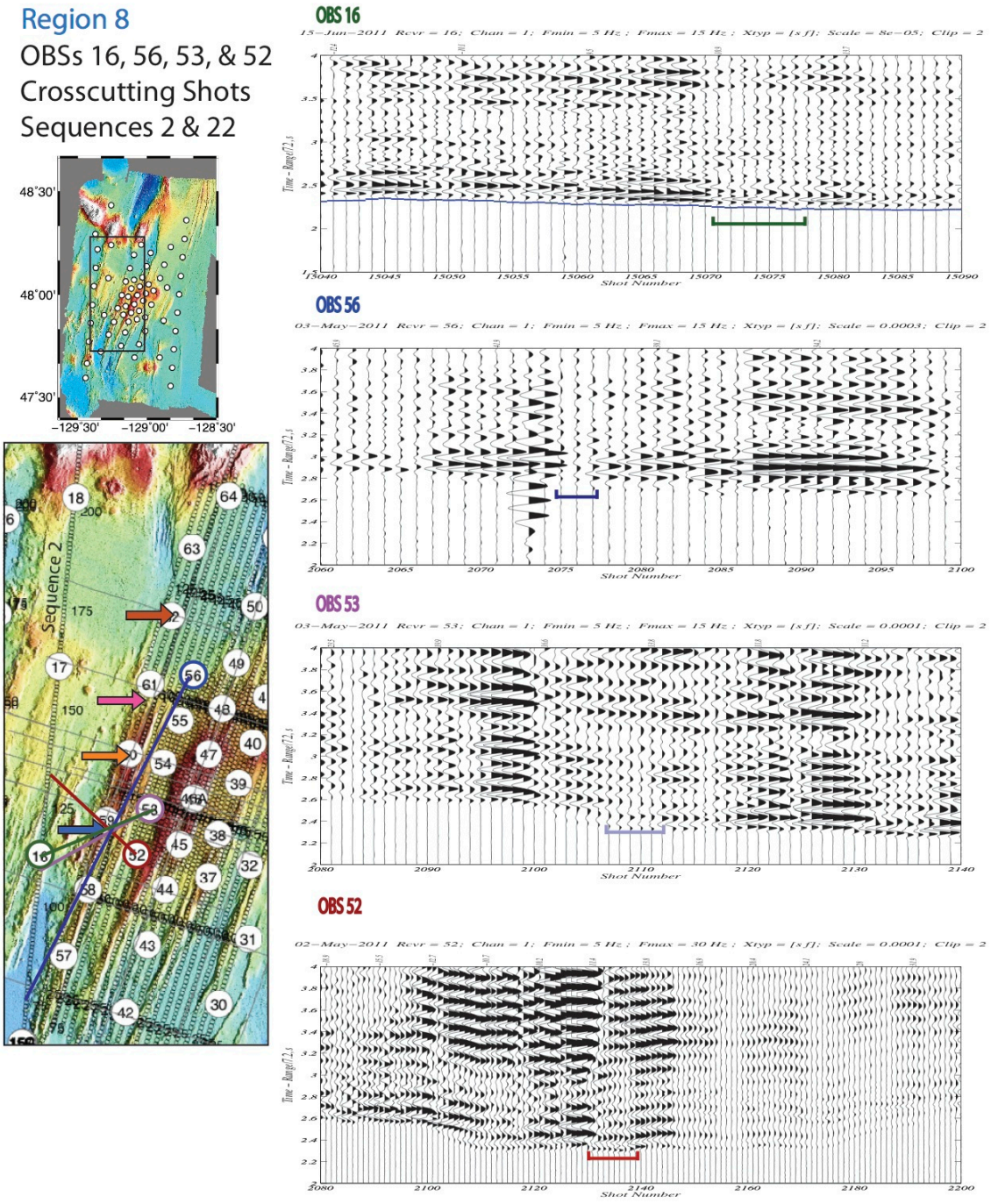

Figure D.5. Region 8 (blue).

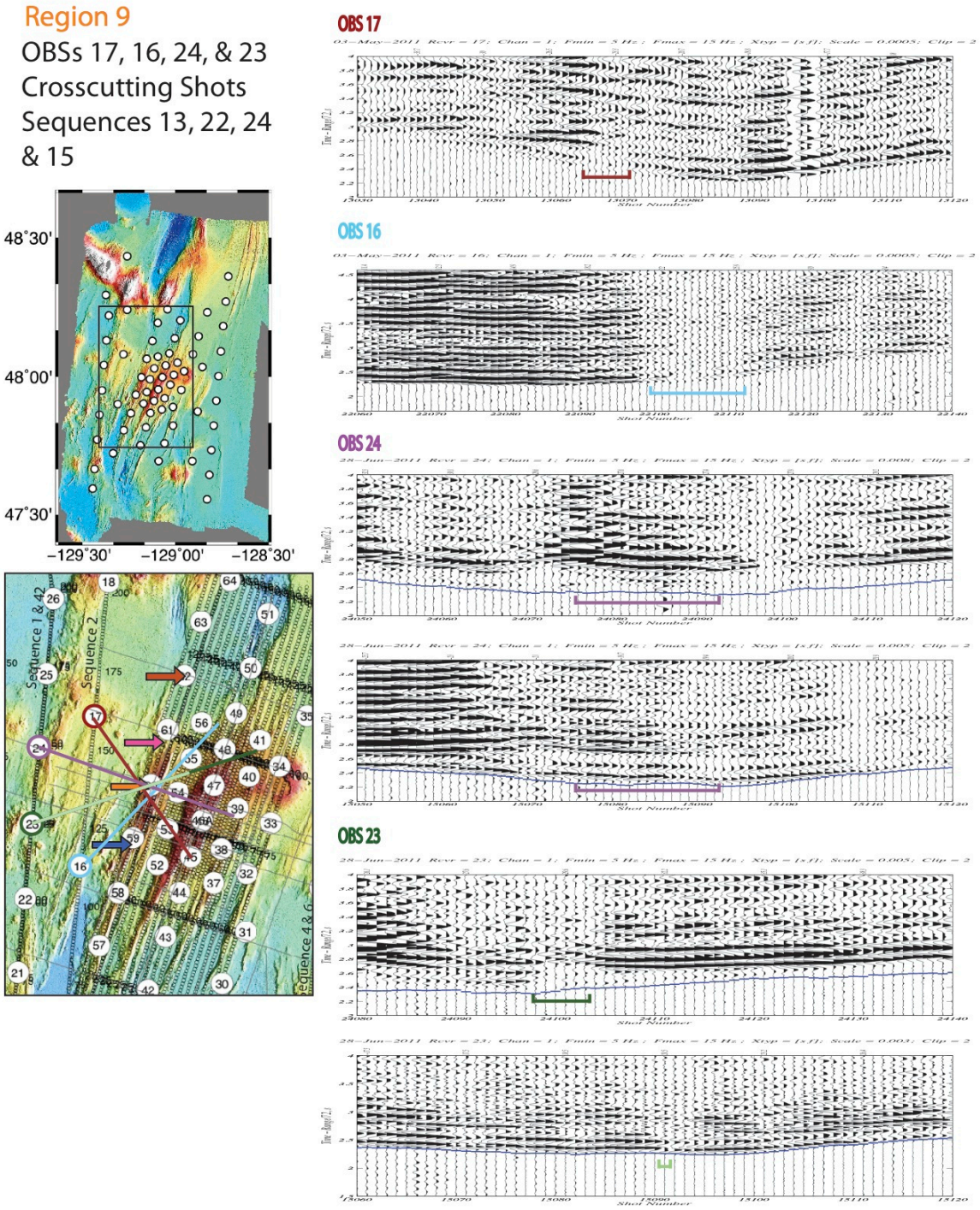

Figure D.6. Region 9 (orange) from eastern direction.

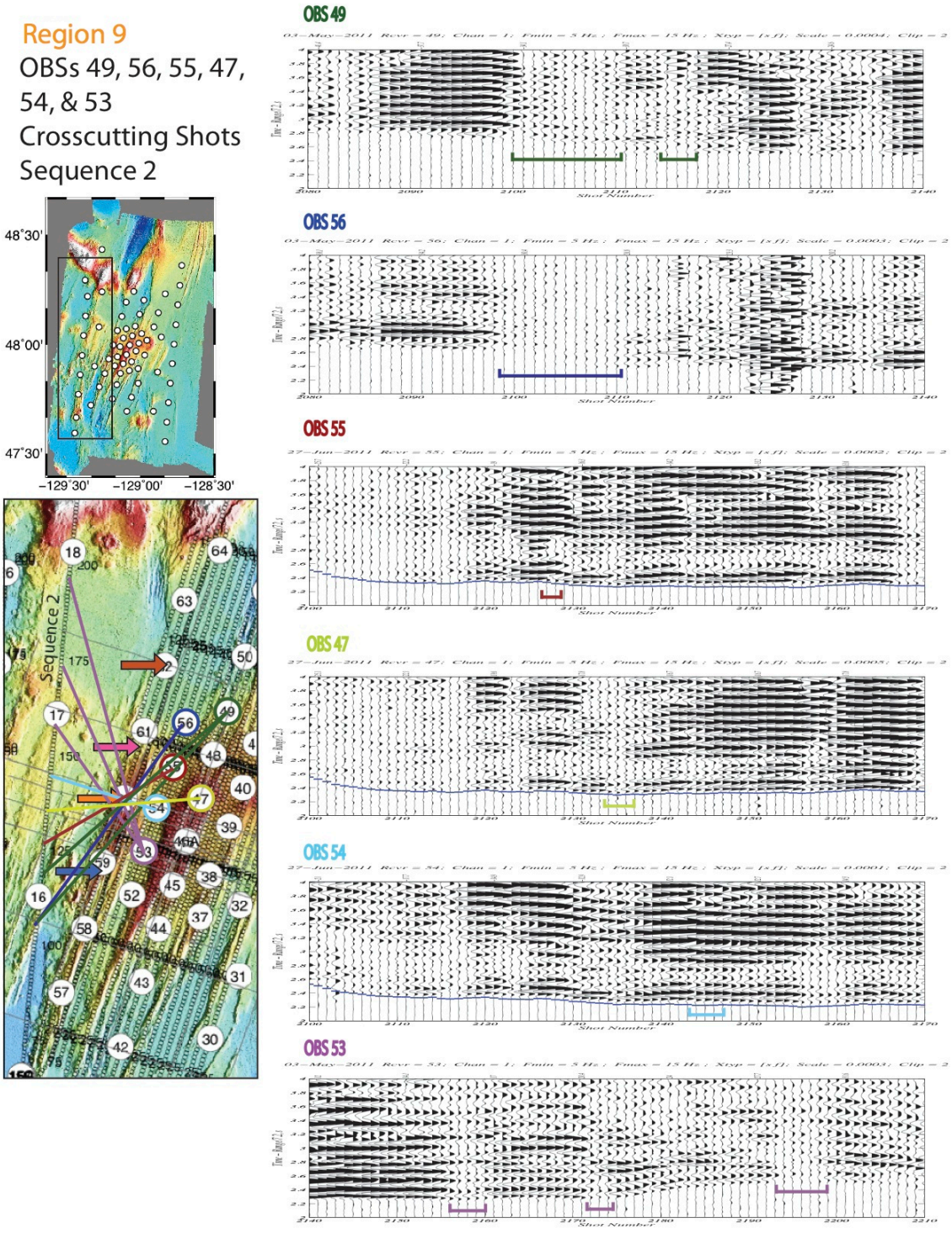

Figure D.7. Region 9 (orange) from western direction.

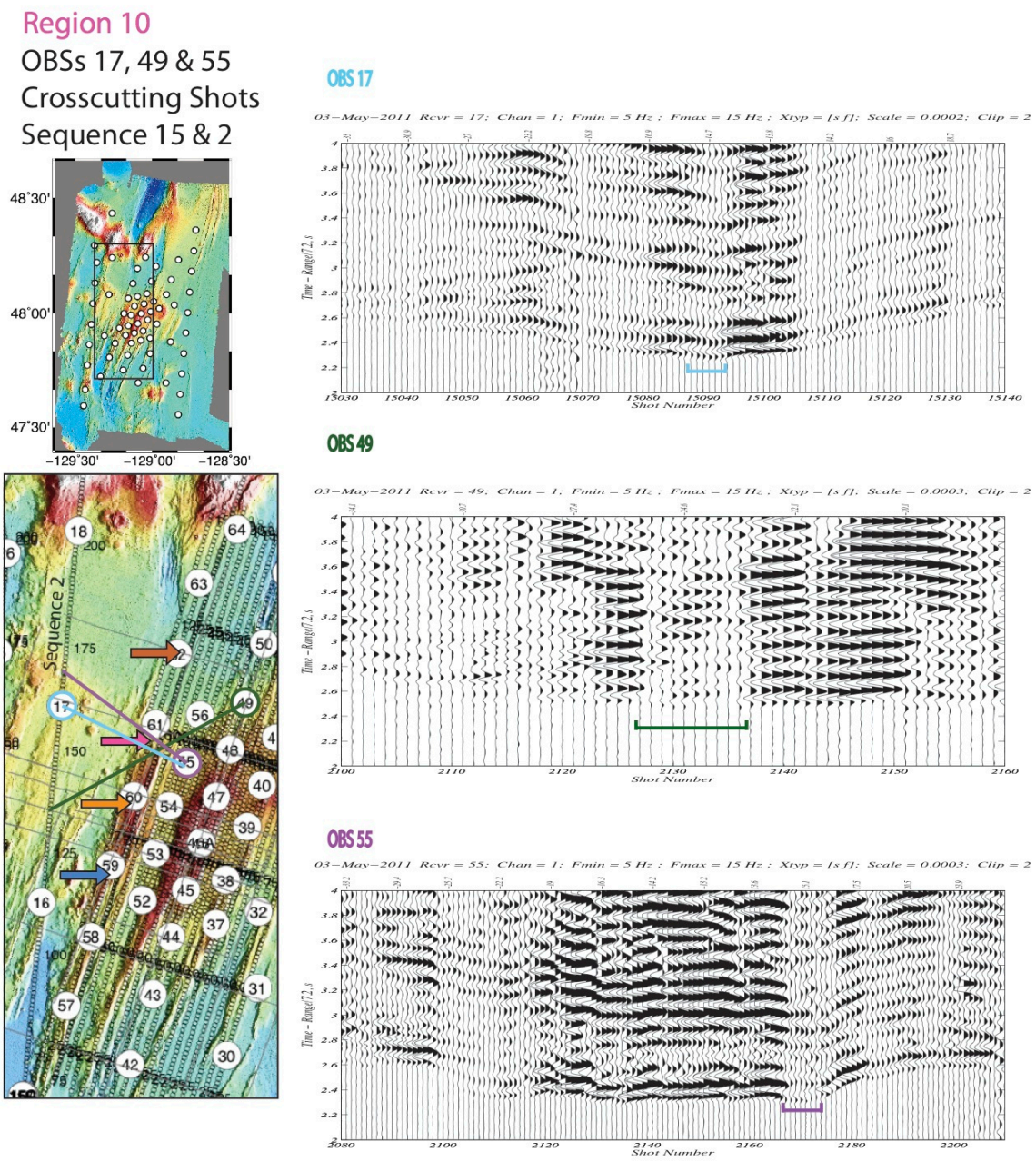

Figure D.8. Region 10 (pink).

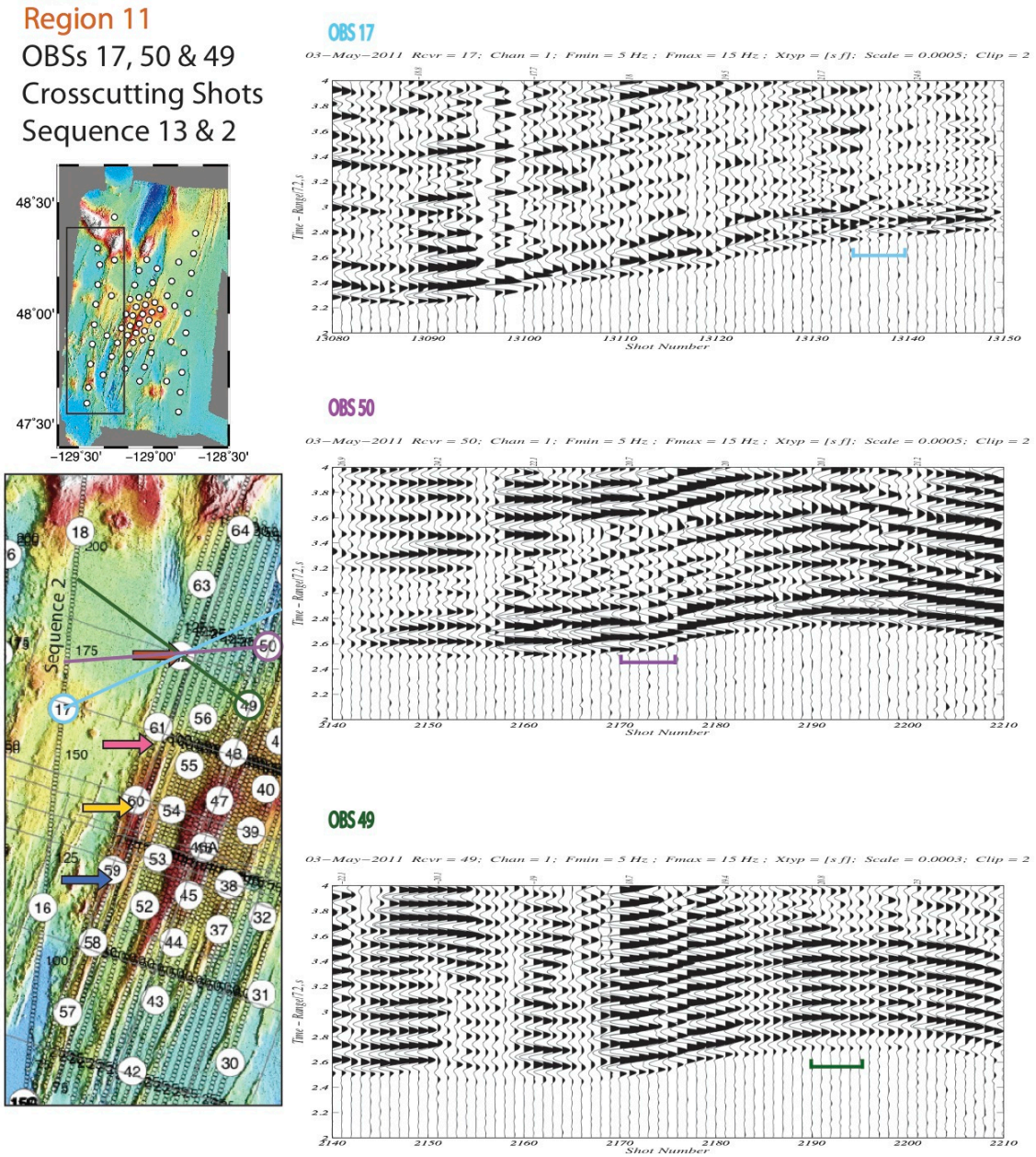

Figure D.9. Region 11 (dark orange).

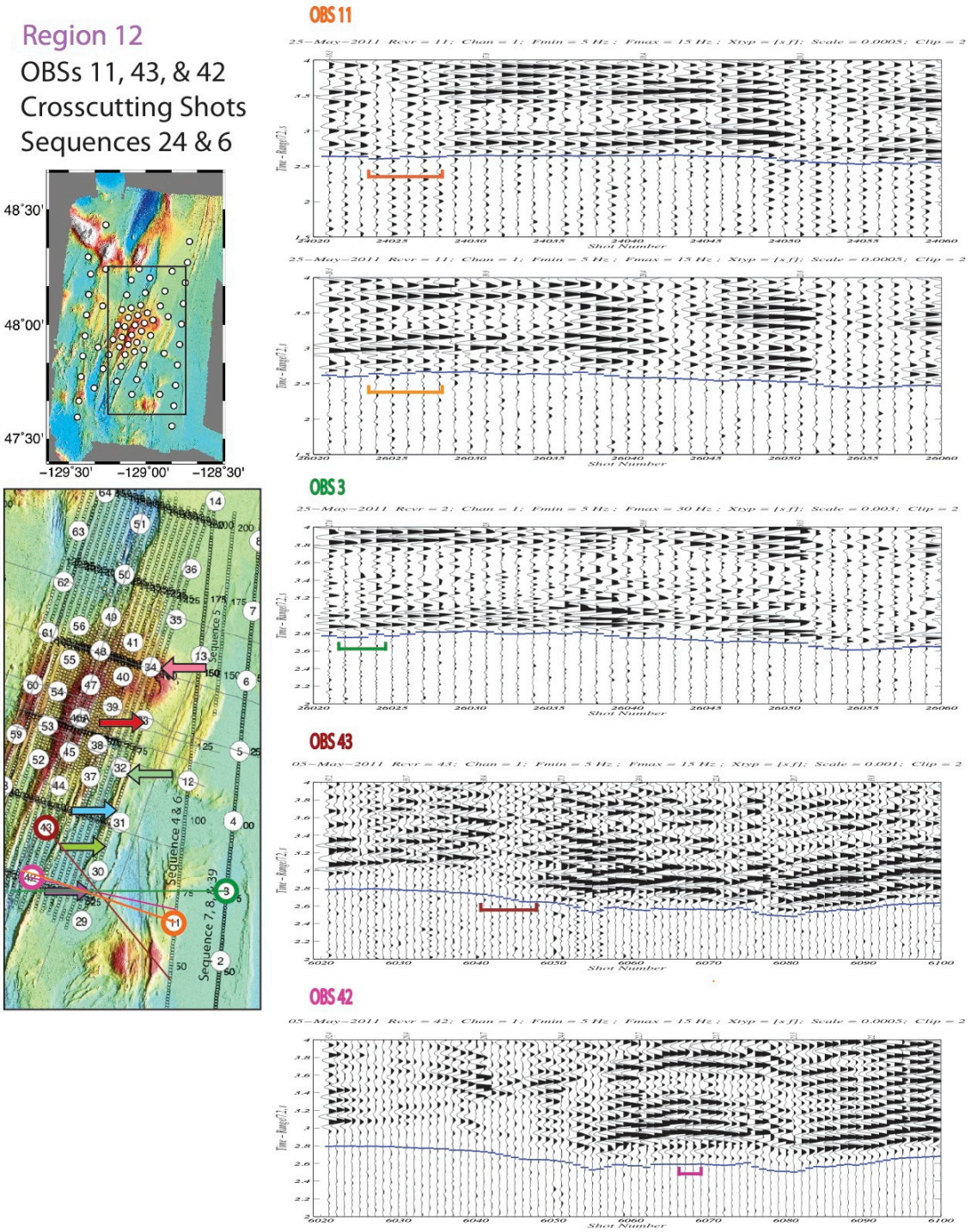

Figure D.10. Region 12 (purple).

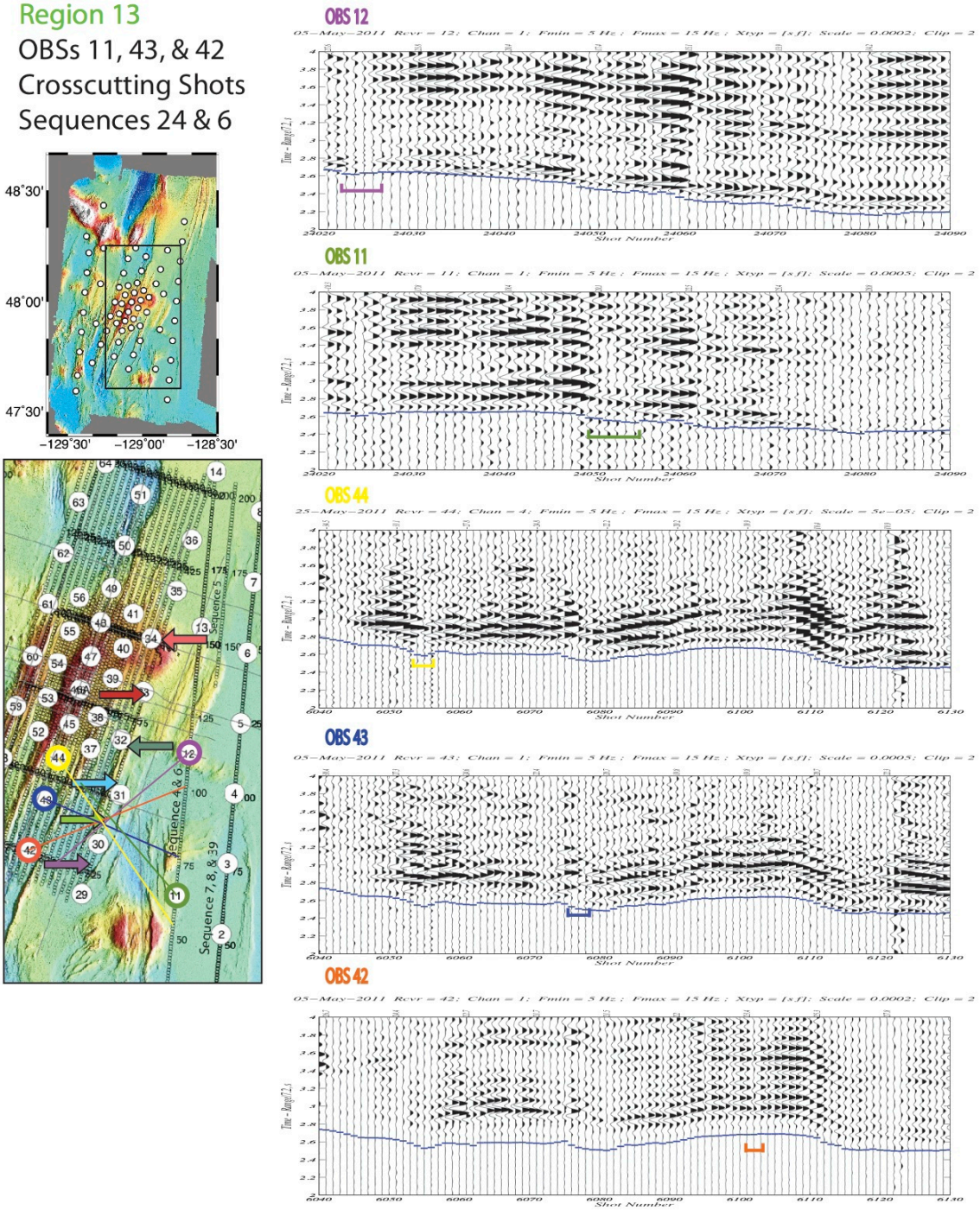

Figure D.11. Region 13 (light green).

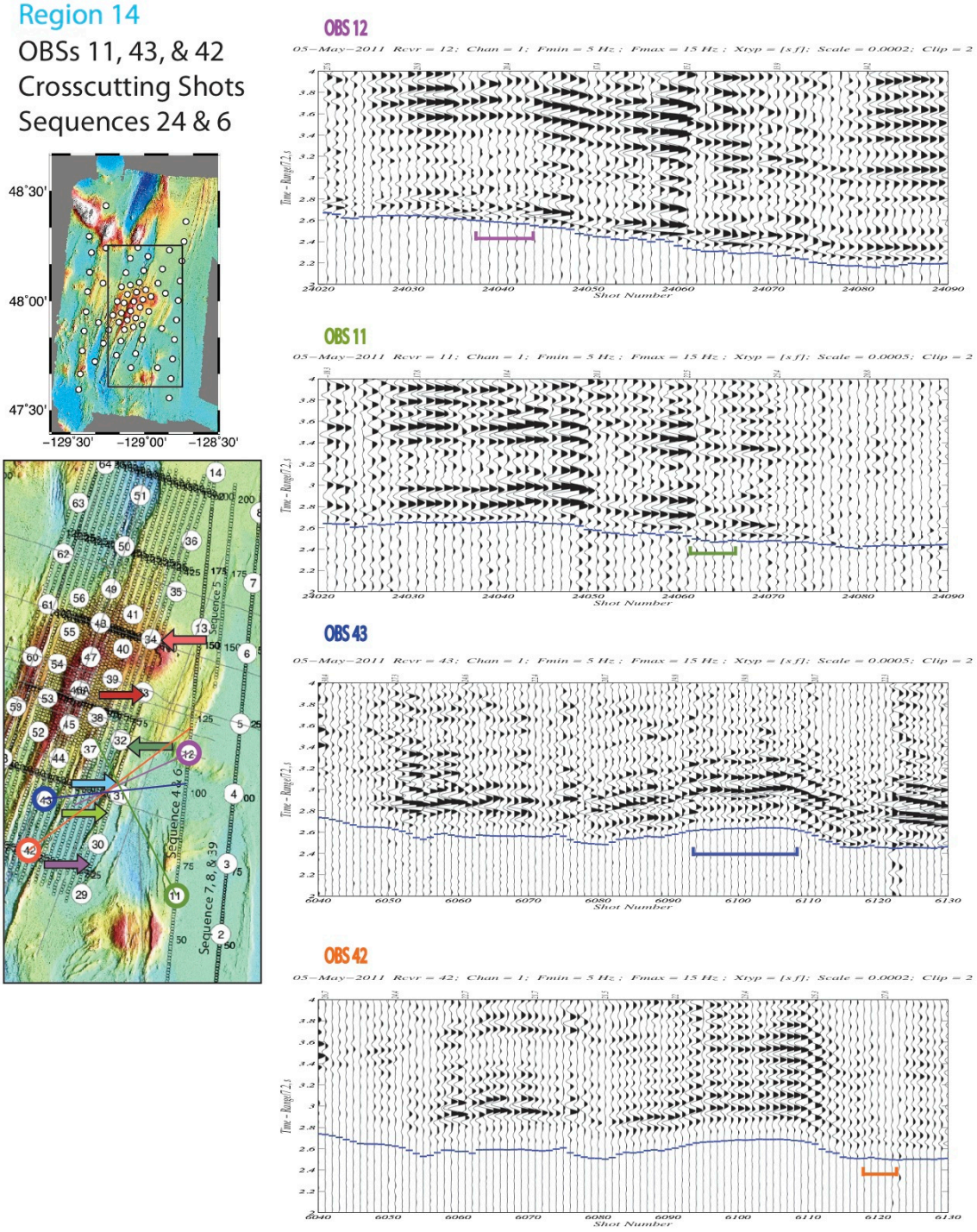

Figure D.12. Region 14 (light blue).

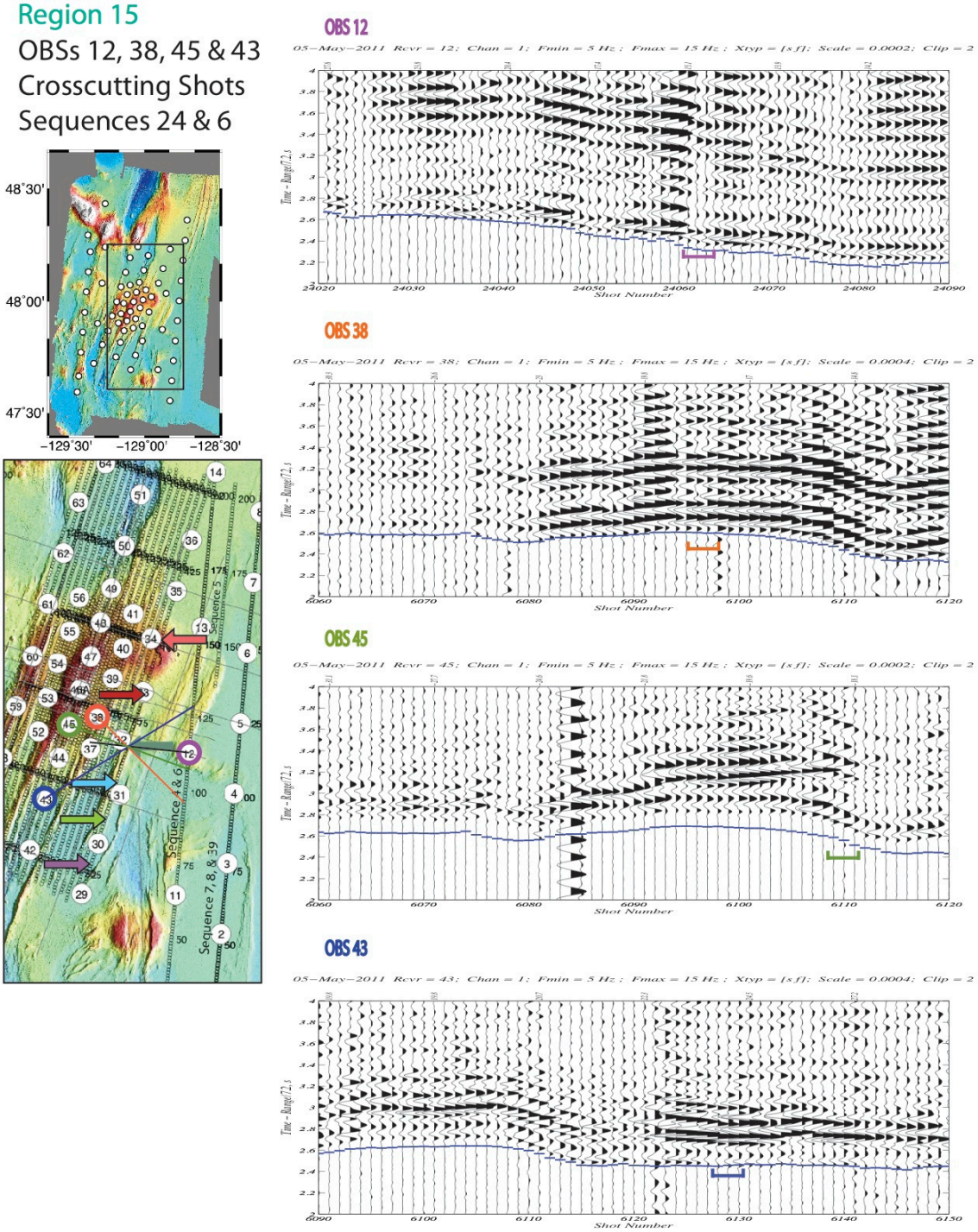

Figure D.13. Region 15 (dark green).

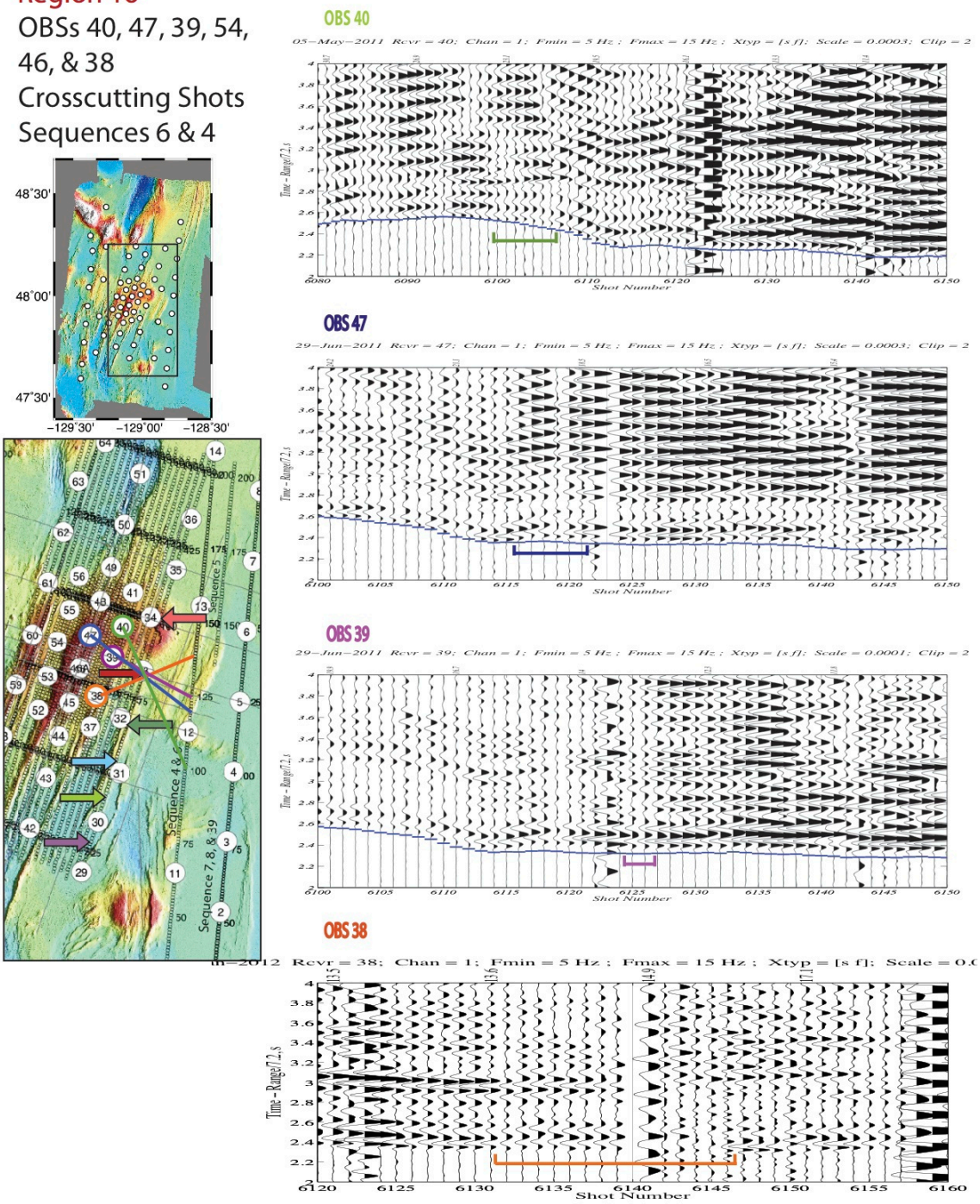

Figure D.14. Region 16 (red) from the eastern direction.

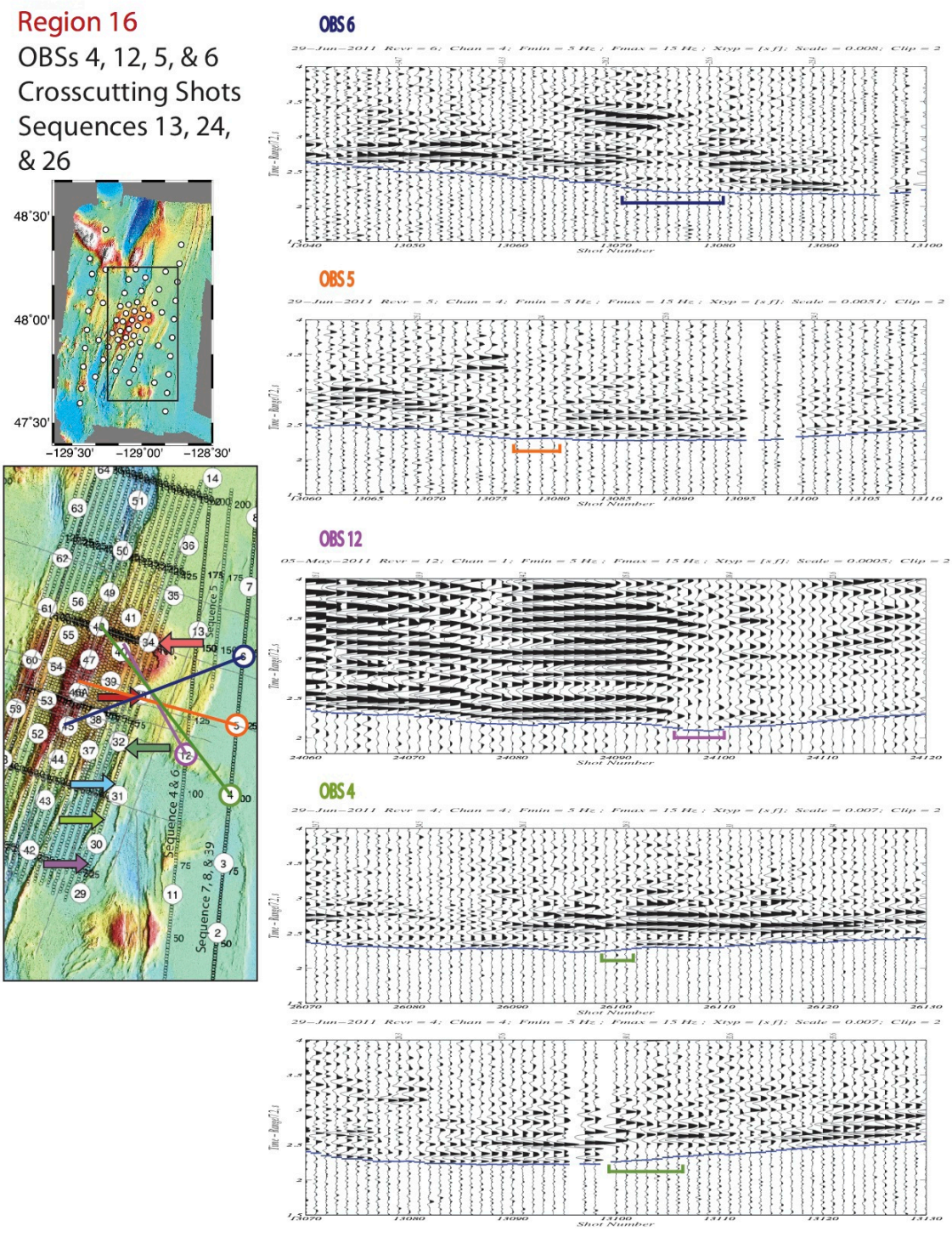

Figure D.15. Region 16 (red) from the western direction.

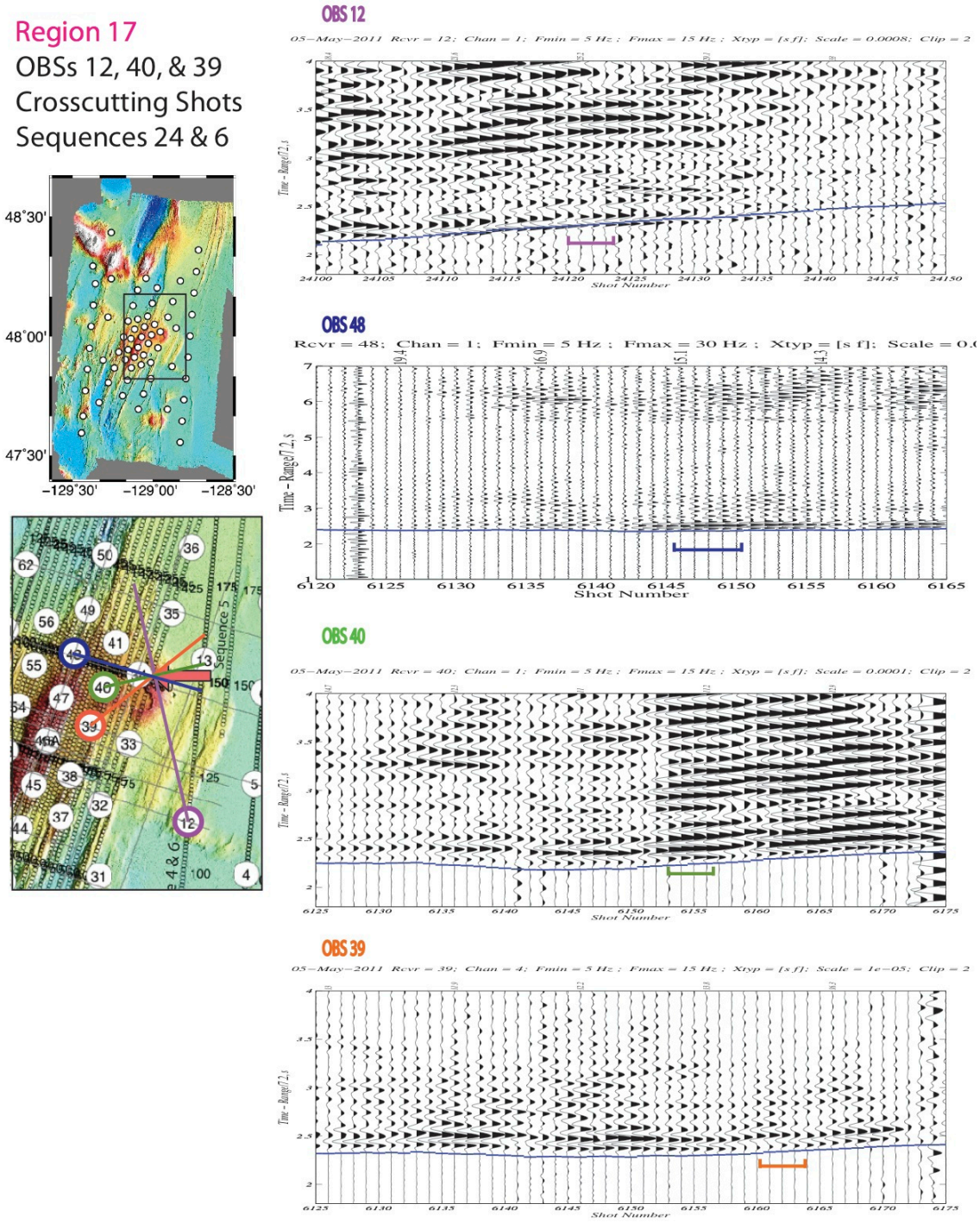

Figure D.16. Region 17 (pink).

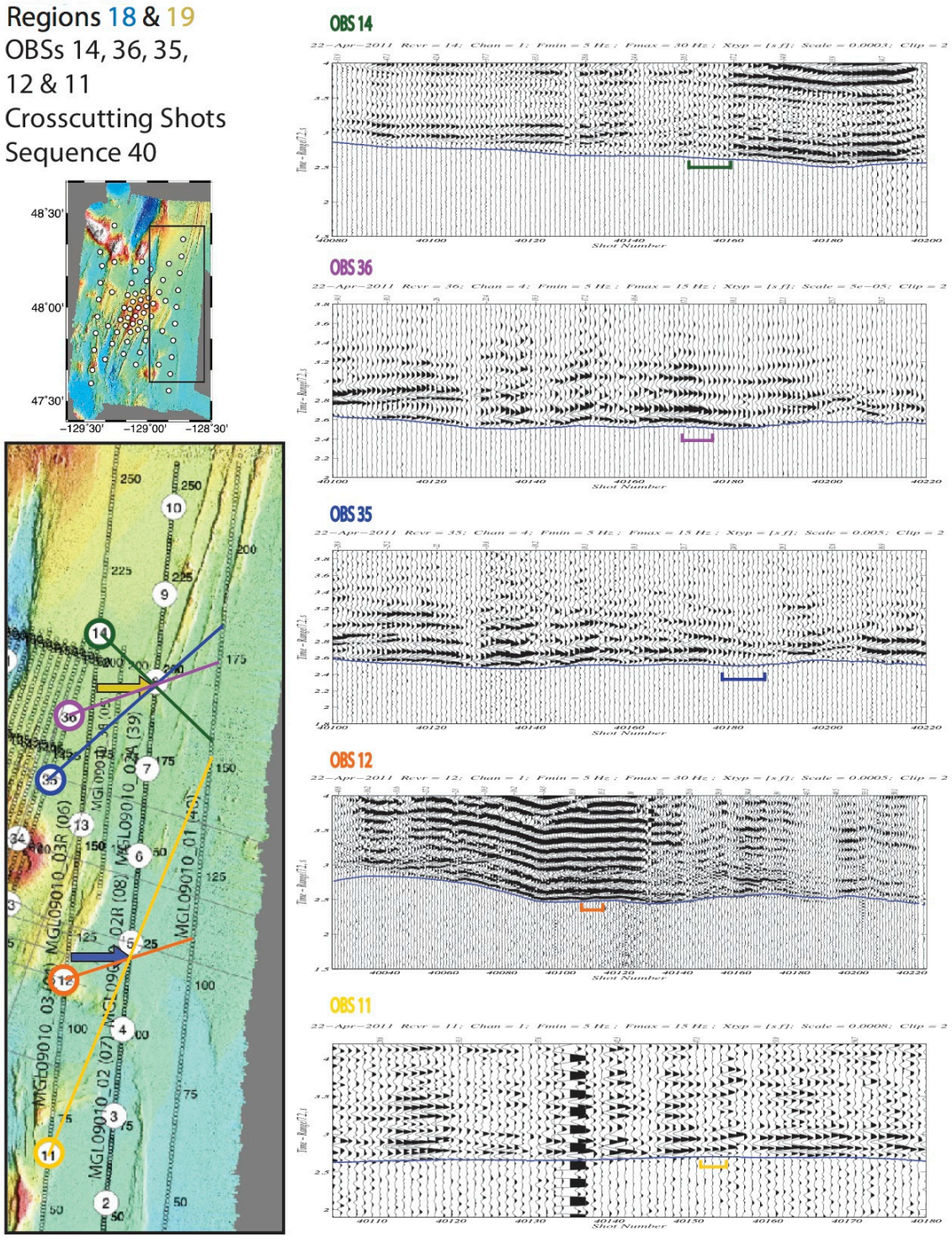

Figure D.17. Regions 18 (blue) and 19 (yellow).

APPENDIX E

THERMAL TIMESCALE CALCULATIONS

The thermal timescale for region 16 is calculated from **Equation 1** (Turcotte and Schubert, 2002),

$$t_s = \frac{b^2}{4\alpha\lambda_2^2} \tag{1}$$

where t_s is the amount of time for a magma body to solidify, b is half the vertical length of the magma body, α is the thermal diffusivity, and λ_2^2 is a dimensionless variable. λ_2 can be calculated from **Equation 2**,

$$\frac{L\sqrt{\pi}}{c(T_m - T_0)} = \frac{e^{-\lambda_2^2}}{\lambda_2(1 + erf\ \lambda_2)} \tag{2}$$

where L is the latent heat, erf is the error function, c is a constant, T_m is the temperature of the molten material, and T_0 is the initial temperature of the country rock (Turcotte and Schubert, 2002).

Using a value of L = 320 kJ/kg, $T_m - T_0$ = 1000 K, and c = 1.2 kJ/(kgK), Turcotte and Schubert (2002) find λ_2 = 0.73. I use this value for λ_2, b = 1 km, and α = 0.5 mm^2/s (Turcotte and Schubert, 2002) to find a solidification time (t_s) of ~29,800 years. Hydrothermal cooling greatly enhances conductive cooling. This is typically modeled as enhanced thermal conductivity, where the effective thermal conductivity, κ_{eff}, can be calculated from **Equation 3.**

$$\kappa_{eff} = Nu\,\kappa_{true} \tag{3}$$

Nu is the Nusselt number, and κ_{true} is the true conductivity. The Nusselt number is found to be 8 at mid-ocean ridges (Phipps Morgan and Chen, 1993).

The thermal diffusivity, α, can be calculated from **Equation 4**,

$$\alpha = \frac{\kappa}{\rho\, c_p} \tag{4}$$

where ρ is the density, c_p is the specific heat capacity, and κ is the thermal conductivity. By combing **Equations 3** and **4**, I multiply the thermal diffusivity (α = 0.5 mm^2/s) by a Nu value of 8 to represent the addition affect of hydrothermal cooling, which yields a solidification of ~3,700 years.

REFERENCES CITED

Baker, E.T, German, C.R., Elderfield, H., 1995. Hydrothermal plumes over spreading-center axes: global distribution and geological inferences. Geophysical Monograph 91, American Geophysical Union; p. 47-71.

Barclay, A.H., Toomey, D.R., Purdy, G.M., and Solomon, S.C., 1998. Seismic structure and magmatic accretionary processes at the Mid-Atlantic Ridge, 35° N. Journal of Geophysical Research; v. 103, no. B8, p. 17,827-17,844.

Barclay, A.H., Wilcock, W.S.D., 2004. Upper crustal seismic velocity structure and microearthquake depths at the Endeavour Segment, Juan de Fuca Ridge. Geochemistry Geophysics Geosystems; v. 5, no. 1.

Canales, J.P., Carton, H., Carbotte, S.M., Mutter, J.C., Nedimovic, M.R., Xu, M., Aghaei, O., Marjanovic, M., Newman, K., 2012. Network of off-axis melt bodies at the East Pacific Rise. Nature Geoscience; doi:10.1038/ngeo1377.

Canales, J.P., Detrick, R.S., Toomey, D.R., Wilcock, W.S.D., 2003. Segment-scale variations in the crustal structure of 150–300 kyr old fast spreading oceanic crust (East Pacific Rise, 8°15′N–10°5′N) from wide-angle seismic refraction profiles. Geophysical Journal International; v. 152, is. 3, p. 766–794.

Canales, J.P., Nedimovic, M., Graham, K., Carbotte, Detrick, B., 2009. Seismic reflection images of a near-axis melt sill within the lower crust at the Juan de Fuca ridge. Nature; v. 460, doi:10.1038/nature08095.

Carbotte, S.M., Detrick, B., Graham, K., Diebold, J., Canales, P., Harding, A., 2002. Cruise Report R/V Maurice Ewing EW0207. http://www.ig.utexas.edu/sdc/cruise.php?cruiseIn=ew0207

Carbotte, S.M., Robert, R.S., Harding, A., Canales, J.P., Babcock, J., Kent, G., Van Ark, E., Nedimovic, M., Diebold, J., 2006. Rift topography linked to magmatism at the intermediate spreading Juan de Fuca Ridge. Geological Society of America; v. 34, no. 3, p. 209-212.

Carbotte, S.M., Nedimovic, M., Canales, J.P., Kent, Harding, A., Marjanovic, M., 2008. Variable crustal structure along the Juan de Fuca Ridge: influence of on-axis hot spots and absolute plate motions. Geochemistry Geophysics Geosystems; v. 9, no. 8.

Christensen, N.I., 1979. Compressional wave velocities in rocks at high temperatures and pressures, critical thermal gradients and crustal low-velocity zones. Journal of Geophysical Research; v. 84, p. 6849-6857.

Christensen, G.L., Shaw, P.R., Garmany, J.D., 1997. Shear and compressional wave structure of the East Pacific Rise, 9°-10° N. Journal of Geophysical Research; v. 102, no. B4, p. 7821-7835.

Christensen, N.I., Shaw, G.H., 1970. Elasticity of mafic rocks from the Mid-Atlantic Ridge. Geophysical Journal International; v. 20, is. 3, p. 271–284.

Creager, K.C., Jordan, T.H., 1986. Slab penetration into the lower mantle beneath the Mariana and other island arcs of the northwest Pacific. Journal of Geophysical Research; v. 91, p. 3573-3589.

Cudrak, C. F., Clowes, R. M., 1993. Crustal structure of Endeavour Ridge Segment, Juan de Fuca Ridge, from a detailed seismic refraction survey. Journal of Geophysical Research; v. 98, no. B4, p. 6329–6349.

Davis, E.E., Karsten, J.L., 1986. On the cause of the asymmetric distribution of seamounts about the Juan de Fuca Ridge: Ridge-crest migration over a heterogeneous asthenosphere. Earth and Planetary Science Letters; v. 79, p. 385-396.

Durant, T.D., Toomey, D.R., 2009. Evidence and implications of crustal magmatism on the flanks of the East Pacific Rise. Earth and Planetary Science Letters; v. 287, p. 130-136.

Fuchs, K., Schulz, K. 1976. Tunneling of Low-Frequency Waves through the Subcrustal Lithosphere. Journal of Geophysical Research; v. 42, p. 175-190.

Govers, R., Meijer, P.T., 2001. On the dynamics of the Juan de Fuca plate: Earth and Planetary Science Letters; v. 189, p. 115–131, doi: 10.1016/ S0012–821X(01)00360–0.

Hammond, S. R., 1997. Offset caldera and crater collapse on Juan de Fuca Ridge-flank volcanoes. Bulletin of Volcanology; v. 58, no. 8, p. 617 – 627.

Haymon, R.M., Macdonald, K.C., Benjamin, S.B., Ehrhardt, C.J., 2005. Manifestations hydrothermal discharge from young abyssal hills on the fast-spreading East Pacific Rise flank. Geology; v. 33, no. 2, p. 152-156.

Hess, P., 1992. Phase equilibria constraints on the origin of ocean floor basalts. Geophysical Monograph 71, American Geophysical Union; p. 67.

Hooft, E.E.E., Patel, H., Wilcock, W., Becker, K., Butterfield, D., Davis, E., Dziak, R., Inderbitzen, K., Lilley, M., McGill, P., Toomey, D., Stakes, D., 2010. A seismic swarm and regional hydrothermal and hydrologic perturbations: The northern Endeavour segment. Geochemistry, Geophysics, Geosystems; v. 11, no. 12, Q12015, doi.org/10.1029/2010GC003264.

Humphreys, E.D., Dueker, K.G., 1994. Physical state of the western U.S. upper mantle. Journal of Geophysical Research; v. 99, p. 9635-3965.

Johnson, H.P., Karsten, J.L., Delaney, J.R., 1983. A detailed study of the Cobb Offset of the Juan de Fuca Ridge: Evolution of a propagating rift. Journal of Geophysical Research; v. 88, no. B3, p. 2297-2315.

Kappel, E.S., Ryan, W.B.F., 1986, Volcanic episodicity and a non-steady state rift valley along the northeast Pacific spreading centers: Evidence from SeaMARC I: Journal of Geophysical Research; v. 91, p. 13,925–13,940.

Karsten, J. L., 1988. Spatial and temporal variations in the petrology, morphology, and tectonics of a migrating spreading center: The Endeavour segment, Juan de Fuca Ridge. University of Washington. Ph.D. thesis; p. 329.

Karsten, J.L., Delaney, J.R., Rhodes, J.M., Liias, A., 1990. Spatial and temporal evolution of magmatic systems beneath the Endeavour Segment, Juan de Fuca Ridge: tectonic and petrologic constraints. Journal of Geophysical Research; v. 95, p. 19235-19256.

Karsten, J.L., Hammond, S.R., Davis, E.E., Currie, R.G., 1986. Detailed geomorphology and neotectonics of the Endeavour segment, Juan de Fuca Ridge: New results from Seabeam swath mapping, Geological Society of America Bulletin; v. 97, no. 2, p. 213–221.

Larsen, S., Harris, D., 1993. Seismic wave propagation through a low-velocity nuclear rubble zone. Lawrence Livermore National Laboratory. Master thesis.

Leybourne, M. I., N. A. Van Wagoner, 1991. Heck and Heckle seamounts, northeast Pacific Ocean: High extrusion rates of primitive and highly depleted mid-ocean ridge basalt on off-ridge seamounts. Journal of Geophysical Research; v. 96, p. 16,275– 16,293, doi:10.1029/91JB00595.

Macdonald, K.C., 1984. Mid-ocean ridges: Fine scale tectonics, volcanic and hydrothermal processes within the plate boundary zone. Annual Review of Earth and Planetary Sciences; v. 10, p. 155-190.

Moser, T.J., 1991. Shortest path calculation of seismic rays. Geophysics; v. 56, no. 1.

Nedimović, M.R., Carbotte, S.M., Diebold, J.B., Harding, A.J., Canales, J.P., Kent, G.M., 2008. Upper crustal evolution across the Juan de Fuca ridge flanks. Geochemistry Geophysical Geosystems; v. 9., n. 9.

Phipps Morgan, J., and Chen, Y. J., 1993. The genesis of oceanic crust: Magma injection, hydrothermal circulation, and crustal flow. Journal of Geophysical Research; v. 98, p. 6283-6297.

Riddihough, R.P., 1984, Recent movements of the Juan de Fuca plate. Journal of Geophysical Research; v. 89, p. 6980-6994.

Rohrs, K.M.M., Milkereit, B., Yorath, C.J., 1988. Asymmetric deep crustal structure across the Juan de Fuca Ridge. Geology; v. 16, p. 533-537.

Shoberg, T., Stein, S., Karsten, J., 1991. Constraints on rift propagation history at the Cobb Offset, Juan de Fuca Ridge, from numerical modeling of tectonic fabric. Tectonophysics; v. 197, p. 295–308, doi:10.1016/0040-1951(91)90047-V.

Toomey, D.R., Jousselin, A., Dunn, R.A., Wilcock W.S.D., Detrick, R.S. 2007. Skew of mantle upwelling beneath the East Pacific Rise Governs Segmentation. Nature; v. 444, p. 409-414, doi:10.1038/nature05679.

Toomey, D.R., Durant, T.D., Hooft, E.E.E, Kohtaro, A., Price, R., Soule, D., Wells, A.E., Wilcock W.S.D. 2009. Cruise Report: Endeavour Seismic Tomography Experiment. http://pages.uoregon.edu/drt/MGL0910_Science_Report/pages/100.html.

Turcotte, D.L., Schubert, G., 2002. Geodynamics. Cambridge University Press; p. 166-168.

Tyson, P., 2010. Birth of an Expedition. PBS Online. Into the Abyss. http://www.pbs.org/wgbh/nova/abyss/mission/birth.html.

Van Ark, E.M., Detrick, R.S., Canales, J. P., Carbotte, S.M., Harding, A.J., Kent, G.M., Nedimovic, M.R., Wilcock, W.S.D., Diebold, J.B., Babcock, J.M., 2007. Seismic structure of the Endeavour Segment, Juan de Fuca Ridge: Correlations with seismicity and hydrothermal activity. Journal of Geophysical Research; v. 112, B02401, doi: 10.1029/2005JB004210.

Van Wagoner, N.A. Leybourne, M.I., 1991. Evidence for magma mixing and a heterogeneous mantle on the West Valley Segment of the Juan de Fuca Ridge. Journal of Geophysical Research; v. 96, B10, 16295-16318.

Weekly, R.T., Wilcock, W.S.D, Toomey, D.R, Hooft, E.E., Wells, A.E, 2011. Upper- to Mid-Crustal Seismic Velocity Structure of the Endeavour Segment: Implications for Crustal Construction. American Geophysical Union; Fall Meeting, ab. V11E-2552.

Wendt, R. E., Cornejo, E.A., Perfit, M.R., Cousens, B.L., Clague, D.A., 2007. Geochemistry of the Vance Seamount chain: Off-axis seamounts along the southern Juan de Fuca Ridge. American Geophysical Union; Fall Meeting, ab. V21B-0609.

Wilcock, W.S.D., Delaney, J.R., 1996. Mid-ocean ridge sulfide deposits: Evidence for heat extraction from magma chambers or cracking fronts? Earth and Planetary Science Letters; v. 145, p. 49-64.

Wilcock, W.S.D., Dougherty, M.E., Solomon, S.C., Purdy, G.M., Toomey, D.R., 1993. Seismic propagation across the East Pacific Rise: finite difference experiments and implications for seismic tomography. Journal of Geophysical Research; v. 98, p. 19913-19932.

Zou, H., Zindler, A., Niu, Y., 2002. Constraints on melt movement beneath the East Pacific Rise from ^{230}Th-^{238}U disequilibrium. Science; v. 295, p. 107-110.